Progress in Energy and Combustion Science 85 (2021) 100902

Contents lists available at ScienceDirect

Progress in Energy and Combustion Science

journal homepage: www.elsevier.com/locate/pecs

Continuum scale modelling and complementary experimentation of solid oxide cells

Steven B. Beale[a,b,*], Martin Andersson[a,c], Carlos Boigues-Muñoz[d], Henrik L. Frandsen[e], Zijing Lin[f], Stephen J. McPhail[d], Meng Ni[a,g], Bengt Sundén[c], André Weber[h], Adam Z. Weber[i]

[a] Forschungszentrum Jülich GmbH, 52425 Jülich, Germany
[b] Queen's University, Kingston, ON K7L 3N6, Canada
[c] Lund University, Lund 22100, Sweden
[d] Italian National Agency for New Technologies, Energy and Sustainable Economic Development, 00123 Rome, Italy
[e] Technical University of Denmark, 4000 Roskilde, Denmark
[f] University of Science and Technology of China, Hefei 230026, China
[g] The Hong Kong Polytechnic University, Hung Hom, Kowloon, Hong Kong China
[h] Karlsruhe Institute of Technology, 76131 Karlsruhe, Germany
[i] Lawrence Berkeley National Laboratory, Berkeley, CA 94720, United States

ARTICLE INFO

Article history:
Received 16 April 2019
Accepted 19 December 2020

Keywords:
Solid oxide fuel cells
Solid oxide electrolysers
Mathematical modelling

ABSTRACT

Solid oxide cells are an exciting technology for energy conversion. Fuel cells, based on solid oxide technology, convert hydrogen or hydrogen-rich fuels into electrical energy, with potential applications in stationary power generation. Conversely, solid oxide electrolysers convert electricity into chemical energy, thereby offering the potential to store energy from transient resources, such as wind turbines and other renewable technologies. For solid oxide cells to displace conventional energy conversion devices in the marketplace, reliability must be improved, product lifecycles extended, and unit costs reduced. Mathematical models can provide qualitative and quantitative insight into physical phenomena and performance, over a range of length and time scales. The purpose of this paper is to provide the reader with a summary of the state-of-the art of solid oxide cell models. These range from: simple methods based on lumped parameters with little or no kinetics to detailed, time-dependent, three-dimensional solutions for electric field potentials, complex chemical kinetics and fully-comprehensive equations of motion based on effective transport properties. Many mathematical models have, in the past, been based on inaccurate property values obtained from the literature, as well as over-simplistic schemes to compute effective values. It is important to be aware of the underlying experimental methods available to parameterise mathematical models, as well as validate results. In this article, state-of-the-art techniques for measuring kinetic, electric and transport properties are also described. Methods such as electrochemical impedance spectroscopy allow for fundamental physicochemical parameters to be obtained. In addition, effective properties may be obtained using micro-scale computer simulations based on digital reconstruction obtained from X-ray tomography/focussed ion beam scanning electron microscopy, as well as percolation theory. The cornerstone of model validation, namely the polarisation or current-voltage diagram, provides necessary, but insufficient information to substantiate the reliability of detailed model calculations. The results of physical experiments which precisely mimic the details of model conditions are scarce, and it is fair to say there is a gap between the two activities. The purpose of this review is to introduce the reader to the current state-of-the art of solid oxide analysis techniques, in a tutorial fashion, not only numerical and but also experimental, and to emphasise the cross-linkages between techniques.

---

* Corresponding author at: Institute of Energy and Climate Research, IEK-14: Electrochemical Process Engineering, Forschungszentrum Jülich GmbH, 52425 Jülich, Germany.
E-mail address: s.beale@fz-juelich.de (S.B. Beale).

https://doi.org/10.1016/j.pecs.2020.100902

Contents

1. Introduction

Numerical modelling is critical for understanding the operation of solid oxide fuel cells (SOFCs) and electrolysers (SOEC) due to the highly coupled physics that occur at multiple time and length scales. The aim of this paper is to cover the state-of-the-art of solid oxide cell (SOC) modelling, so as to provide the reader with an overview of best practices on this topic at the continuum scale. The paper covers relatively focussed aspects of SOC modelling, and so a number of related areas, such as elementary kinetics of electrochemical reactions, materials modelling, and thermodynamic modelling of materials and interfacial stability, spatially-resolved microstructural modelling, system-level modelling are considered outside the scope of the review. Indeed, the challenge facing the modeller is to identify the important phenomena to be analysed in detail, as well as those which are less important. Successfully choosing the trade-off between representativeness and efficiency in the model is the key achievement in preparation for the set of processes to be simulated. This paper aims to provide a comprehensive, critical review and practical guideline to facilitate a synergetic approach towards the numerical simulation and experimental validation of SOCs. While covering the state-of-the art of modelling in this work, we have attempted to describe the assumptions made for each of the different physical phenomena treated. This is done by (i) introducing the overall development of modelling of SOCs; (ii) describing the best practices in continuum scale modelling; (iii) providing details on different approaches to modelling the different phenomena occurring at the microscale; and (iv) relating this to experimental approaches in an attempt to enumerate recommendations as to what researchers should address, combining models and experiments in a scientifically sound manner. The goal is tutorial; so that someone new to the field can rapidly understand the current scope and limitations of SOC modelling.

Physicochemical hydrodynamics [3] deals with the interaction between fluid flow and physical and chemical processes. SOCs are a classic example of such an interaction. As is noted in [4,5]

> “It is of the utmost importance to assign a clear objective to the model in order to correctly address the following trade-off triad: generality, realism and precision.”
>
> Richard Levins

In other words, in the author’s opinion, it is impossible to create a model capable of simultaneously generating realistic and precise results for processes occurring at very different length and time scales. Fig. 1 provides an overview of all processes taking place in an SOC and their time constants/relaxation frequencies. These will be described in further detail in the chapters that follow. In the space/time domain, quantum mechanical phenomena occur at length/time scales of below 1 nm/ns, molecular dynamics modelling at scales of below 1 µm/µs. Continuum scale modelling in the range of µm/µs to m/days is the primary focus of this article. In the frequency domain, nanoscale charge transport processes are on the order of GHz, whereas electrochemical reactions and charge transfer are associated with frequencies of kHz. A range of scales of models (atomistic/elementary kinetics, microstructure based electrode models, cell and stack models, and finally, system models) exist. Each level of model typically requires closures from an order-of-magnitude smaller; so, for example a cell-level model requires the electronic properties of the electrodes and effective mechanical property values to be prescribed. These may be obtained from sub-scale models based on digital reconstruction. Similarly, stack-level models need volume-averaged or ‘homogenised’ data, obtained from the cell level or from a single-repeating unit (SRU). Therefore, such sub-scale phenomena are also considered

Nomenclature

Roman symbols

A	Forward Tafel slope, V
a_i	Activity coefficient
B	Reverse Tafel slope, V
c_p	Specific heat, J/(kg·K)
D_H	Hydraulic diameter, m
D	Diffusivity, m^2/s
E	Nernst potential, V
e	Internal energy, J/kg
E_a	Activation energy, J/(mol·K)
F	Faraday’s constant, C/mol
G	Gibb’s energy, J/mol
g	Mass transfer coefficient, conductance, kg/(m·s)
h	Enthalpy, J/mol
h	Heat transfer coefficient, conductance W/(m^2K)
H	Enthalpy, J/kg
I	Radiant intensity, W/(sr·m), W/m
i''	Current density, A/m^2
i''_0	Exchange current density, A/m^2
j''	Diffusion flux, kg/(m^2·s)
k	Thermal conductivity, W/(m·K)
k_p	Equilibrium constant
M	Molecular weight, kg/mol
M	Geometric factor
m	Mass, kg
$\dot{m}''$	Mass flux, convection flux, kg/(m^2·s)
N	Mole number, mol
P	Product
p	Pressure, partial pressure, Pa
Q	Reaction quotient
$\dot{q}'''$	Volumetric heat source, J/m^3
Q	Charge, C
R	Reactant
R	Universal gas constant, J/(K·mol)
r	Resistance, Ohm·m^2
S	Entropy, J/(mol·K)
s	Entropy, J/(kg·K)
T	Temperature, K
U	Internal energy, J/mol
u	Velocity, m/s
V	Cell voltage, V, volume m^3
y	Mass fraction
n	Charge number in Faraday’s equation

Greek symbols

α	Transfer coefficient
β	Symmetry coefficient, constriction factor
Γ	Exchange coefficient, kg/(m·s)
γ	Reaction order
ε	Porosity
ε_υ	Utilisation
λ	Triple-phase boundary length per unit volume, m/m^3
η	Activation overpotential, V
μ	Dynamic viscosity, kg/(m·s)
μ	Chemical potential, J/mol
$\bar{\mu}$	Electrochemical potential, J/mol
ν	Stoichiometric coefficient
ρ	Density, kg/m^3
σ	Conductivity, S/m
τ	Tortuosity
Φ	Viscous dissipation, m^2/s^2

ϕ	Utilisation

Subscripts

a	Air electrode
b	Bulk value
f	Fuel electrode
g	Gas
min	Minimum
rxn	Reaction
s	Solid
w	Wall value
_	Complex variable

Superscripts

eff	Effective
0	At reference temperature

Non-dimensional numbers

Re	Reynolds number, uD_H/ν
Sc	Schmidt number, ν/D
Sh	Sherwood number $gD_H/\rho D$
St	Stanton number, $h/\rho uc_p$

Subscripts

a	Air/oxidant
an	Anode
ca	Cathode
f	Fuel/feedstock
in	Inlet
out	Outlet
prod	Product
react	Reactant

Abbreviations

CFD	Computational fluid dynamics
DRT	Distribution of relaxation times
ECM	Equivalent circuit modelling
EIS	Electrochemical impedance spectroscopy
FEM	Finite element method
FVM	Finite volume method
KMC	Kinetic Monte Carlo
LSC	Lanthanum strontium cobalt
LSCF	Lanthanum strontium cobalt ferrite
LSM	Lanthanum strontium manganite
MIEC	Mixed ionic electronic conductor
MSR	Methane steam reforming reaction
RUL	Remaining useful life
SEM	Scanning electron microscope
SOEC	Solid oxide electrolyser cell
SOFC	Solid oxide fuel cell
SRU	Single repeating unit
TPB	Triple-phase boundary
WGSR	Water-gas-shift reaction
YSZ	Yttria stabilised Zirconia

in this article. Neither elementary kinetics nor microstructural features are discussed in any great detailed, however.

1.1. Solid oxide cells: Pathway of technology development

The SOFC technology enables the transformation of chemical energy stored in hydrocarbon and carbon-free fuels into electrical energy and heat with high efficiency via an electrochemical reaction. Moreover, if operated in reverse mode (i.e., consuming electrical power), these devices operate as electrolysers (SOECs), convert-

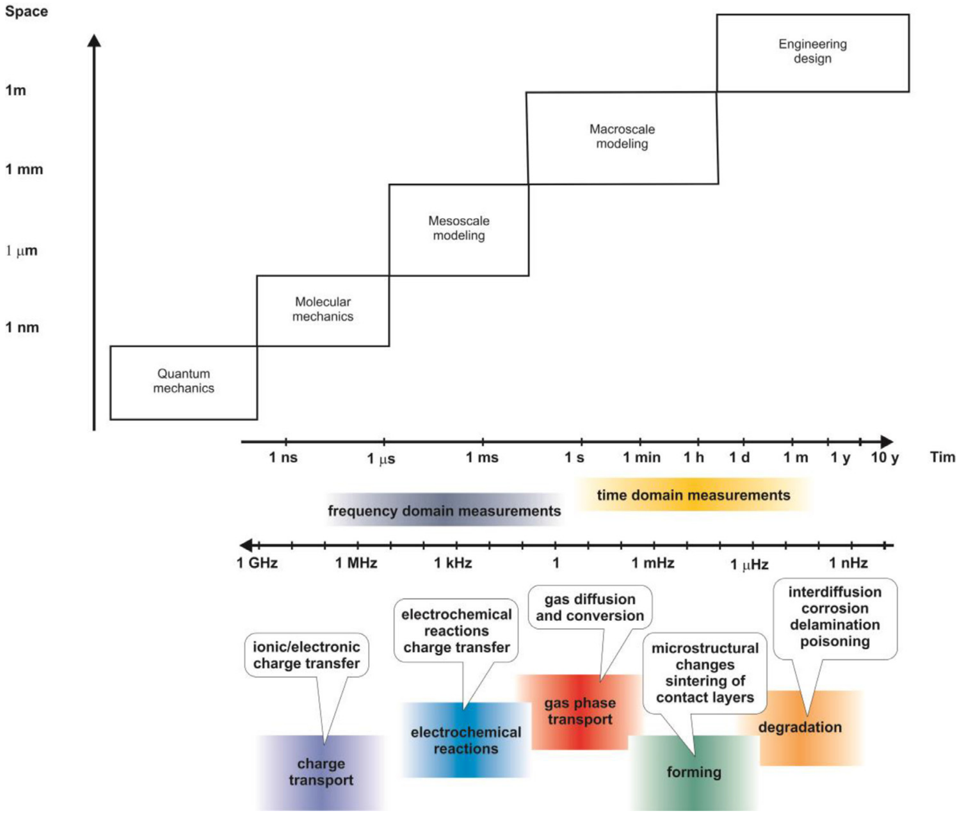

Fig. 1. Time, length, and frequency scales for physicochemical processes in SOCs, adapted from [1,2].

ing substances such as steam into chemical media. State-of-the-art SOCs operate in the temperature range of 600 to 1000°C, enabling the use of a wide range of fuels in fuel cell mode, and high temperature waste heat and high efficiency in electrolysis mode due to the fast electrode kinetics. With oxygen ions as the charge carrier in the electrolyte the technology also facilitates co-electrolysis of H_2O and CO_2, therefore becoming an attractive means for valorising CO_2.

1.1.1. SOC history and state-of-the-art

The origins of SOCs can be traced to the 1890s, when Nernst developed the so-called ‘Nernst mass’ (85% ZrO_2 and 15% Y_2O_3) prototype of the present day anion-conducting electrolyte, pursuing the replacement of gas lighting by electric filaments [6]. However, it was not until 1937 when Swiss scientists Baur and Preis [7] manufactured the first SOFC prototype which, despite chemical instabilities between the electrolyte and electrodes, demonstrated that zirconia-based materials exhibit relatively high ionic conduction at elevated temperatures (600-1000°C) [8,9]. SOEC technology attracted interest in the 1980s thanks to the studies of Donitz and Erdle [10], who reported the first SOEC results within the HotElly project using electrolyte-supported tubular cells [11].

1.1.2. SOC basic principles

The SRU of an SOC is a solid state device consisting of porous positive (air) and negative (fuel/feedstock) electrodes, a solid electrolyte, interconnects, and fuel and air channels. The optimum thickness of the electrodes depends on the balance of transport of ions, electrons, and gases and is of the order of 30-40 µm. The electrolyte should in most cases be as thin as possible on a continuum scale. However, for mechanical strength, one of the layers must be substantially thicker, in order for it to support the cell; either the electrolyte, or one of the electrodes, porous electrically-conducting support layers made of metal or cermet, e.g., Ni-3YSZ [12].

An electrode may be considered to be made of a chemically-active region and one or more porous transport layers, used for gas distribution below the interconnect contact points, conduction and/or mechanical strength. These additional passive layers are sometimes simply referred to as being part of the electrode, and at other times are identified as separate components. The fuel electrode substrate and functional layers are typically fabricated with a porous nickel/yttria-stabilised zirconia (YSZ) cermet. The electrolyte is a thin layer of YSZ, around 2-8 µm in thickness, in the case of electrode-supported cells, or 80 to 200 µm where the electrolyte acts as mechanical support. A gadolinium-doped cerium-oxide layer is applied to the electrolyte prior to depositing state-of-the-art $(La,Sr)(Co,Fe)O_{3-\delta}$ (LSCF) air electrodes to avoid the formation of zirconates ($SrZrO_3$) due to inter-diffusion of air electrode constituents into the zirconia electrolyte layer. Much research and development are still ongoing in identifying new, alternative material combinations for the SOC active components, but these lie outside the scope of this paper as they are focused on material compatibility issues and do not affect the basic electrochemical principles dealt with here. SOC fuel electrodes oxidise H_2 (SOFC) or reduce H_2O (SOEC) at the boundaries where the gas, ion- and electron-conducting phases meet. This region is known as the triple phase boundary (TPB) and is distributed throughout the whole electrode to maximise performance. Fig. 2 is an image obtained by a scanning electron microscope (SEM), wherein the core components described above are visible, also showing the different microstructures of each.

SRUs of planar configurations incorporate high-temperature sealants that minimise fuel and air losses across the periphery. It is of vital importance that the coefficient of thermal expansion of the different components lie as close to each other as possible in order to avoid undesired mechanical stresses that could potentially lead to the cracking of the cell or brittle interfaces, i.e., glass sealants and contact components between cell and interconnects. Furthermore, chemical reactivity between neighbouring elements should be minimal so as to avoid material degradation.

Two principal SOC geometries are to be found: planar and tubular. The main advantage of tubular SOCs over planar is that they intrinsically confine gases in a highly efficient manner due to the strongly reduced edge-to-active area ratio, hence there is less need to employ high temperature seals. This allows for more rapid transient operations, as well as greater structural robustness during long-term operation. Micro-tubular SOCs, brought to light in the late 1990s [13], have generated higher power densities than their larger counterparts, besides being highly resistant to thermal cycling. However, an efficient current collection and interconnection between tubular-shaped cells to form a stack remains critical issues [14].

Fig. 3 illustrates an example of a planar SOC geometry, produced as thin, flat plates enabling a compact series connection of these to form a stack. The advantages of planar geometry are lower manufacturing costs and higher power densities than for tubular cells. Nonetheless, planar SOCs feature drawbacks that must be addressed to guarantee a high-quality product in the long term: they require strong gas-tight seals to separate fuel and air streams and to bond the stack components together. Furthermore, the flow distribution and thermal gradients across the planar stacks can cause mechanical stresses, which may result in failure when ceramic materials are employed.

Different planar stack designs are commercially available[1]. The earlier SOFC stack designs were cross-flow designs, and the manifolds could easily be externally located. The challenge with cross-flow is the very uneven temperature distribution with one cold corner at the intersect of the two inlets, and a hot corner at the junction of the two outlets [15]. The uneven temperature distribution will result in high thermo-mechanical stresses and uneven operating conditions across the stack, especially when operated in fuel cell mode of operation. Some commercial cross-flow stacks are still available today e.g., the all-ceramic monolithic stack from Saint-Gobain, and the large stacks from FuelCell Energy (Versa Power).

Stacks with unidirectional flow may include counter and co-flow; the former tends to have a slightly warmer centre and higher thermal stresses than the latter [16], which is why the latter is typically chosen in modern commercial designs. Due to the need to cool the stacks, the rate of air flow in a SOFC is much larger than that required stoichiometrically, typically by a factor of 5-10, depending on the current density. To distribute the flow evenly across all cells in the stack, the inlet and outlet pressure for each cell should be nominally equal [17], calling for large vertical manifold channels. This can be achieved by having channels internal to the stack, as in the case of the Mark F design (Fig. 3). Most manufacturers prefer an external manifold on the air side, as in SOLIDpower, Sunfire and Haldor Topsoe stack designs, rather than building large channels into the stack. Some manufacturers have the fuel manifolds in the line of the air flow field within the stack (Sunfire, Haldor Topsoe), whereas others place the fuel manifolds on the side of the stack, so that they do not obstruct the air flow (SOLIDpower, Elcogen). The latter strategy makes a very even flow-field distribution possible, for both fuel and air; as high as 95 % fuel utilisation have been demonstrated yielding a high efficiency of 75% (based on lower heating values) in SOFC operation [18,19]. The cells are typically mounted in a cassette. The cassettes are sub-

---

[1] Reference to any commercial product or corporation name is for information purposes only, and does not constitute recommendation or endorsement by the authors.

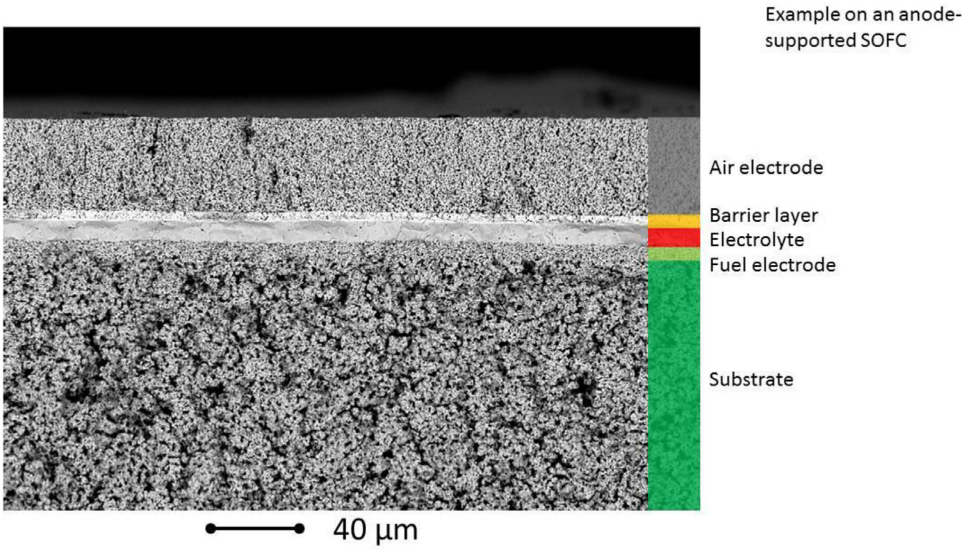

Fig. 2. Scanning electron microscope image of electrode materials for anode supported SOC. Courtesy of IEK-1, Forschungszentrum Jülich GmbH.

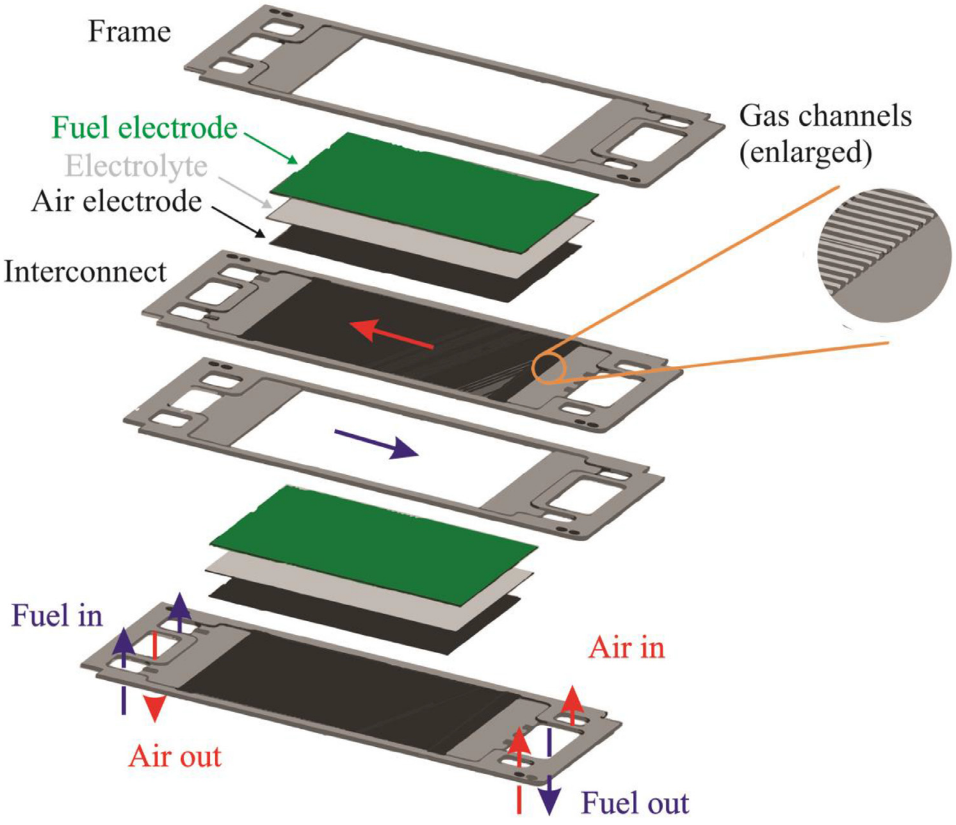

Fig. 3. Schematic of planar anode-support solid oxide fuel cell, based upon the Jülich Mark-F geometry. Courtesy of IEK-14, Forschungszentrum Jülich GmbH.

sequently assembled into a stack with posterior heat treatment to melt the sealing glass, while adding pressure to join all the components.

SOCs use electrochemical reactions for the inter-conversion of electrical and chemical energy. This involves reduction and oxidation of the reagents on either side of the electrochemical cell. The anode is defined as the electrode where the oxidation reaction takes place, generating surplus electrons, whereas the cathode is defined as the electrode where the reduction reaction takes place, consuming electrons. In fuel cell mode, fuel is oxidised at the fuel electrode (i.e., converting hydrogen into water) and is thus called the anode. This oxidation reaction generates electrons that negatively charge the electrode. In electrolysis mode, however, the negative charge is given by the external voltage source, which 'pushes out' the electrons from the reagents, effectively reducing their state (i.e., splitting water to hydrogen and oxygen ions) and thus the 'fuel' electrode, still negatively charged, is by definition the cathode. It is to be noted that for SOCs, the material combinations of the active components (electrodes and electrolyte) generally do not need to change despite the inversion of polarity. The electrolyte remains a conductor of oxygen ions that interact with the electrons at the oxygen (positive) electrode, and the hydrogen (negative) electrode catalyses the steam reduction process in electrolysis mode as it does hydrogen oxidation in fuel cell mode. That is why many processes discussed in this work are fundamentally equivalent for the two modes. The long-term effects of cell degradation are different however, since this often entails a demixing of electrode constituents, the 'direction' of which is influenced by the polarity of operation. Also, the more strongly oxidizing atmosphere at the fuel electrode in electrolysis operation can cause accelerated nickel agglomeration and volatilization compared to fuel cell mode.

To avoid the ambiguity of the terms anode and cathode in SOCs, which can operate as either fuel cells or electrolysers, it is necessary to refer to 'fuel/feedstock' or 'negative' electrodes on the one hand, and to 'air' or 'positive' electrodes, on the other. In this paper, the negative electrode is generally referred to as 'fuel' and the positive electrode as 'air', fully recognising that for electrolysers the fuel is, in fact, feedstock, and that the composition of the oxidant may differ to that of atmospheric air. Fig. 3 is an 'exploded view' of a planar SOC, based on the Jülich Mark-F geometry. Stacks of this type have operated for over 90 000 hours without failure. Fuel and air are introduced to individual cells from the manifolds via gas passages. Air flows through micro-channels machined between the 'ribs' of the air electrode-side of the steel interconnector (see Fig. 3, inset). The ribs provide electrical contact between the electrodes and the porous air electrode. On the fuel side there are no ribs; rather, the fuel flows within the open frame. (Because Fig. 3 is an 'exploded diagram', the electrolyte, which is located within the frame, appears to have been extruded or offset outside of the region.) Metallic contact between the interconnect and anode is achieved by a Ni-mesh (not shown), which is spot-welded to the interconnect plate. This provides a low resistance electrical connection with the anode substrate and also serves to distribute the fuel gas over the region, by inducing mixing. This particular design is a counter-flow configuration. Numerous modelling studies and experimental measurements have shown that, in general, the counter-flow configuration exhibits the best performance in terms of maximum electric potential, power density and cell efficiency, further discussed below. Co-flow generally has the lowest performance, but exhibits a more uniform temperature and current density distributions, and is therefore often preferred. The cross-flow configuration with intermediate performance can have significant undesirable gradients in terms of temperature and current density.

1.1.3. Modelling and physical experiments

The experimental optimisation of SOC stacks is costly, as ideally multiple nominally identical stacks must be tested under the same conditions, at high temperatures, to ensure that small production variations or inconsistent in testing conditions are not the reason for observed failures or discrepancies in performance. Furthermore, post-mortem analyses of failed stacks can be challenging, as detrimental conditions often cause accelerating effects, such as heating due to the direct combustion of a cracked cell or sealant, and the initial cause of failure is not directly observable. Despite these difficulties, experimental characterisation and validation are the best ways to concretely prove the potential of SOC cell/stack assemblies. Different cross-correlating methods to monitor both cells and stacks are valuable in the development of the technology. These include local probing, current-voltage characteristics, and impedance spectroscopy. The cost of experiments must be considered in the development of the technology. Numerical simulation is a tool for predicting the physical phenomena occurring in the microstructure of the cells, in the cells themselves, and when operating an SOC stack. However, modelling requires a large number of physical parameters to be known for the set of governing equations to be solved, and these are rarely well-defined in a complex, compound system such as an SOC. Often, ideal values are used for fundamental parameters, such as a reaction order or pre-exponential factor, for example (see section 2), or values are taken from the literature without questioning their applicability. Being able to assess the real values of these parameters for a given SOC architecture or material combination would allow the models to be more accurate in their representativeness, and increase confidence in their predictions of phenomena that cannot be measured. It is therefore crucial that efforts to test, characterise and validate cells and stacks be accurately synchronised with mathematical modelling of the phenomena and processes that make up the physical objects. Only in this way is it possible to properly understand and ultimately control and design the behaviour and performance of the SOC, and thus more coherently and confidently sustain the market deployment of this high-potential technology for energy conversion.

1.2. Common analysis tools and techniques

Below, the basic experimental characterisation tools, which yield the most common data used for technology assessment and model validation, are briefly described. In-depth description and detailed guidelines for all SOC testing procedures can be found in the literature [20,21]. Furthermore, in section 3 of this review, specific techniques are discussed in greater depth.

1.2.1. Global performance characterisation: Polarisation curves

The polarisation curve is the ubiquitous expression for fuel cell and electrolyser performance at the cell and stack levels. Cell voltage, V, is plotted as a function of current density[2], i''. The open circuit or Nernst potential, E, occurs at equilibrium $i''=0$. Fig. 4(a) shows a polarisation curve for a single SOC operating in both fuel cell, $i'' \geq 0$, and electrolyser, $i'' \leq 0$, modes. It can be seen that the voltage decreases as the current density increases in a relatively linear manner. Generally speaking, for fuel cell mode, the low, intermediate and high current-density regions are frequently referred to as activation, ohmic and concentration areas where losses are primarily due to charge-transfer kinetics, electrical resistance and mass transport, respectively. SOCs are high-temperature devices and, for this reason, activation losses are relatively small: the decrease in voltage as i'' increases from zero is due to thermodynamic, not kinetic factors: When the fuel employed is dry hydrogen, as is further discussed below, the production of water by the reaction leads to a reduction in the thermodynamically-maximum potential, E. When testing and rating fuel cells, an important parameter is the utilisation, ε_u, defined for both air and fuel as the ratio of the fuel/oxidant consumed to the maximum possible value (usually the respective bulk inlet flow). This may be defined, as the mass of air/fuel consumed by the reaction to the inlet supply:

$$\varepsilon_u = \frac{\dot{m}_{\text{rxn}}}{\dot{m}_{\text{in}}} \tag{1}$$

where

$$\dot{m}_{\text{rxn}} = \frac{\mathrm{M}_j i}{z_j \mathrm{F}} \tag{2}$$

Here M_j is the molar mass of fuel (fuel cell) or feedstock water (electrolyser) and air/oxidant (fuel cell) for species j[3], z_j is the

---

[2] It is common in electrochemical texts to denote the current density with the symbol J (to distinguish from current i) and potential by the symbol U. However, in this text the convention of Jacob is employed, whereby a 'dash' denotes a spatial derivative and a 'dot' a temporal derivative. Thus, i''denotes current density (A/m^2) and i'''A/m^3. The symbol E denotes ideal or Nernst potential and the symbol, V, the cell voltage.

[3] Use of the subscript index 'i' is avoided in all expressions which include terms in current, i or current density i″.

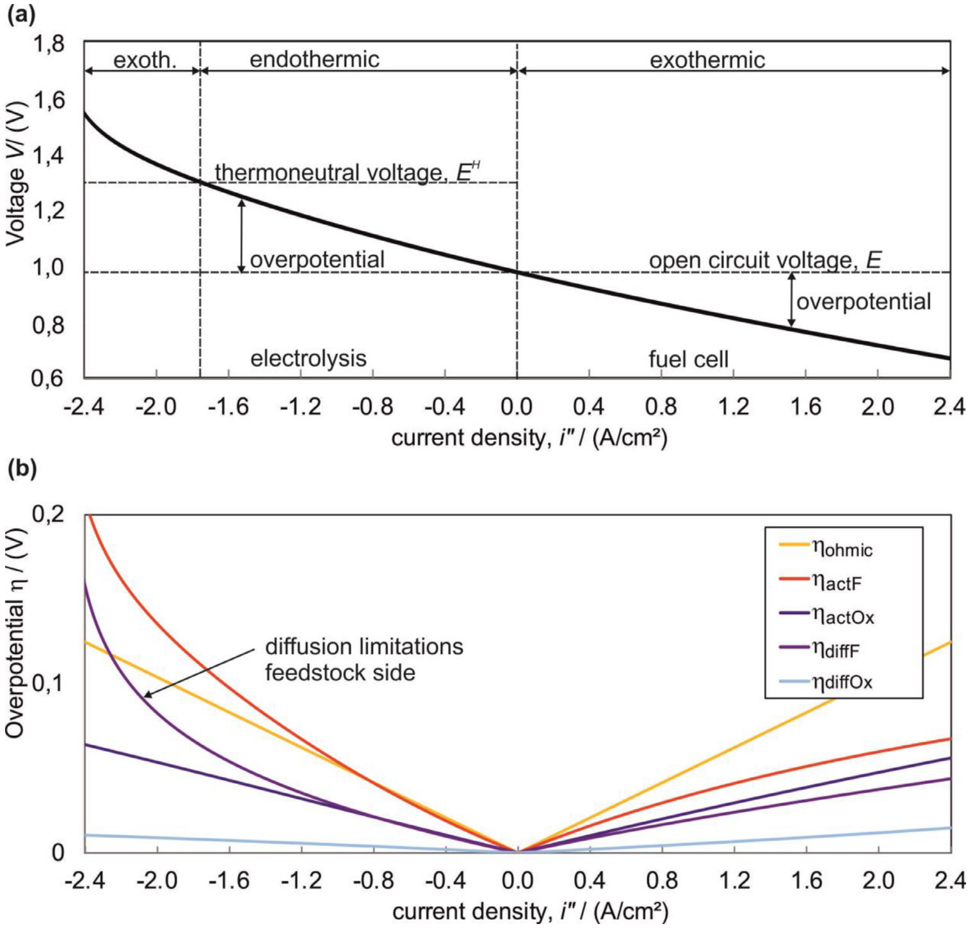

Fig. 4. (a) Polarisation curve for a 1 cm^2 solid oxide cell, based upon Jülich technology [22] with ambient air and 70% H_2/30% H_2O at 800°C. (b) Activation, ohmic and concentration overpotentials for the same cell.

number of charged particles associated with the reaction, F is Faraday's constant, and i is the total current. Eq. (2), is referred-to as Faraday's second law of electrolysis. When performing a polarisation test, both the fuel/air (fuel cell) and water (electrolyser) utilisations can be maintained constant down to some minimum reaction rate (current). This is typically achieved by adjusting the flow rates. However, in air-cooled SOFCs, the air flow is generally adjusted to ensure adequate cooling of the cell (see section 2.7.9) and the fuel flow is also commonly fixed, rather than varied. Therefore, for fuel cell mode, the utilisation increases as the current density increases, and a limiting current may be approached whereby mass transfer is limited by oxygen starvation (not readily apparent on the right side of Fig. 4). Similarly for electrolysers, feedstock starvation is clearly seen on the left side of Fig. 4.

Utilisation may also be defined in terms of outlet values:

$$\varepsilon_u = 1 - \frac{\dot{m}_{out}}{\dot{m}_{in}} \tag{3}$$

If a computational model is employed, the mass flux is obtained by integration at the inlet/outlet as:

$$\dot{m} = \sum_i \dot{m}_i = \sum_i \int_A \rho y_i |\mathbf{u} \cdot \mathbf{dA}| \tag{4}$$

where ρ is mixture density, and y_i is mass fraction for species i (section 2.3), and $\boldsymbol{u}$ and $\boldsymbol{A}$ are inlet/exit velocity and area vectors. Eqs. (1) and (3) will only lead to identical values, when the flow Reynolds numbers, $\mathrm{Re} = uD_H/\nu$, where D_h is a hydraulic diameter and ν kinematic viscosity, or, more correctly, the Péclet numbers, $\mathrm{Pe} = uD_H/D$ where D is diffusivity, are sufficiently high. Otherwise the individual species velocity does not equate with the overall value, $|\boldsymbol{u_i}| \neq |\boldsymbol{u}|$ and Eq. (4) is incorrect. Calculations for the 1996 International Energy Agency (IEA) SOFC benchmark [23], with hydrogen as a fuel, suggest that for the fuel side, Re $<$ 1, so Eqs. (1) and (3) computed this way do not give consistent values [24,25]. Under the circumstances, for both numerical and physical experiments, $\dot{m}$ must be obtained sufficiently far away from the SOC, so that diffusion is negligible. The same situation is also true for heat metering at low flow rates.

1.2.2. In-depth process characterisation: Electrochemical impedance spectroscopy

The polarisation curves of SOCs can only provide the total overpotential at a given operating point. Information about the different underlying loss mechanisms in the cathode, electrolyte, anode and their interfaces do not emerge. These are, however, essential for understanding the cell performance for a targeted optimisation of the cell. Electrochemical impedance spectroscopy (EIS) is a common approach to gain such information, utilising the dynamics of the underlying physicochemical processes in the cell.

Electronic and ionic conduction, charge transfer at interfaces, catalytic reactions, and gas diffusion in porous electrodes are time-dependent processes, resulting in capacitive behaviour in addition to a contribution to the internal resistance of the cell. These are related to the permittivities, space charge layers or chemical capacities, which by their nature yield characteristic responses to sinusoidal excitation. In EIS, a frequency sweep of excitation current or voltage is applied to the SOC (from around 100 kHz to around 0.1 Hz, at logarithmically-spaced intervals) and the response (in volt-

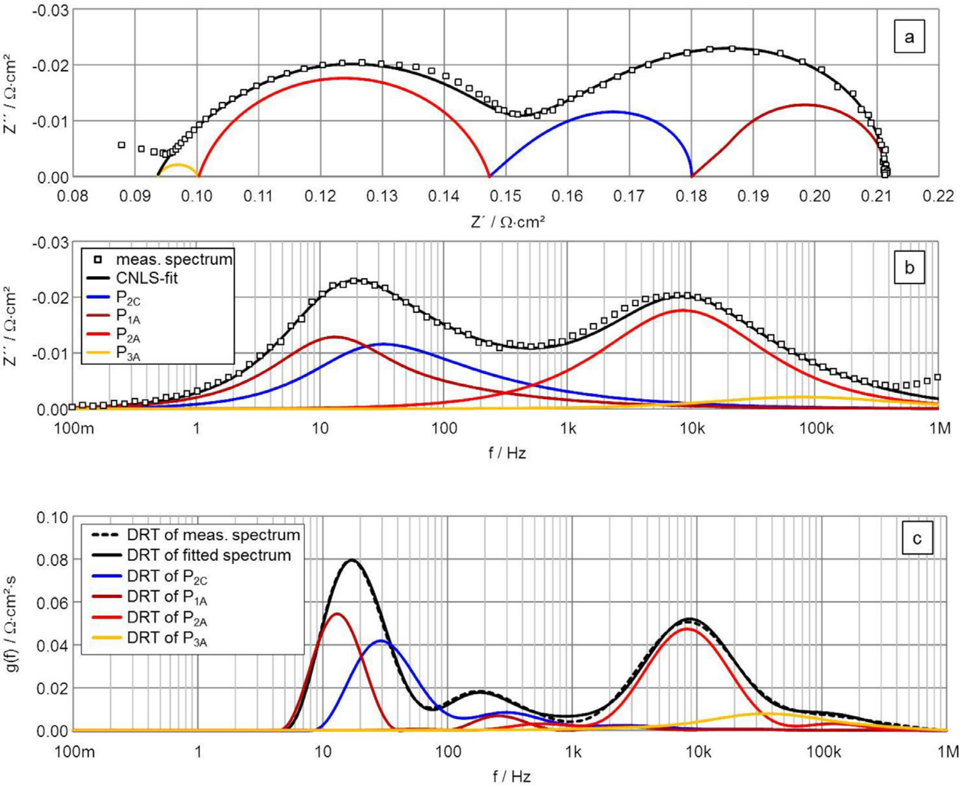

Fig. 5. Impedance spectrum of an anode-supported SOFC, as shown in Figure 2: The Nyquist plot (a), the imaginary part vs. the frequency plot (b) and the distribution of relaxation times (DRT) plot (c) show the measured and fitted spectra. Furthermore, the different contributions of the cathode (P_{2C}) and anode (P_{1A}, P_{2A}, P_{3A}) are displayed (Courtesy IAM-ET, Karlsruher Institute of Technology).

age or current, respectively) is recorded. In the case of fairly slow, forming and degradation processes, see Fig. 1, the temporal change of the impedance spectra yields information about the critical processes for the SOC in long term operation.

The electrical impedance of a linear process is defined as the quotient of a sinusoidal voltage and the related current both sharing the same frequency. This is usually expressed as a complex value, $\underline{Z}$,

$$\underline{Z} = \frac{\underline{V}(t)}{\underline{i}(t)} = \frac{\underline{V}\cdot e^{j\cdot\omega\cdot t}}{\underline{i}\cdot e^{j\cdot\omega\cdot t}} = \frac{\underline{V}}{\underline{i}} = \frac{|\underline{V}|}{|\underline{i}|}\cdot e^{j\cdot\varphi} = |\underline{Z}|\cdot e^{j\cdot\varphi} = R + jX \qquad (5)$$

and displayed in the complex plane as a Nyquist plot, Fig. 5(a).

In the simplest case, the electrical behaviour of process k can be described by an equivalent circuit consisting of its resistance R_k and a parallel capacity C_k, where the dynamics of the process are represented by the time constant, $\tau_k = R_k \cdot C_k$ or the relaxation frequency, $f_k = (2\pi\cdot\tau_k)^{-1}$. To model the dynamics of physicochemical processes in SOCs, more complex equivalent circuits are usually applied and EIS is used as a tool to identify and quantify the associated parameters. The theory is discussed in impedance spectroscopy handbooks, such as those by Macdonald [26], Barsoukov and Macdonald [27], Orazem and Tribollet [28] and Lasia [29], together with practical hints.

Fig. 1 provides an overview of the time constants/relaxation frequencies. A single EIS measurement will generate aggregate information about the electrochemical charge transfer processes, mass transfer, and chemical reactions.

It is essential that the EIS measurement settings, the test bench and cell, satisfy the conditions of linearity, causality, and time-invariance. SOCs couple very diverse mechanisms, making them nonlinear systems; nevertheless, if the excitation signal is small enough (usually V_{AC}< 20 mV), the response can be presumed to be linear. Causality and time-invariance are more critical requirements that can be impacted by the test bench (harmonics of the AC power line, drift or oscillation of the gas flows, or fuel humidification) and the stability of the cell. Practical guidelines for the EIS-measurements of SOCs can be found in Klotz *et al.* [30] and in the IEC 62282-8-1 Standard on test procedures for SOCs (to be issued in 2020). A method to evaluate the measured spectra is described in Schönleber *et al.* [31] and the related software is available online [32].

The interpretation of electrochemical impedance spectra is often hampered by the complexities of the phenomena and their overlap in the frequency domain. Neither Nyquist nor Bode plots, see Fig. 5, are capable of displaying distinctly the different loss mechanisms in an SOC.

Recently developed mathematical approaches [33,34] have succeeded in obtaining a distribution of relaxation times (DRT) from the EIS spectrum, enabling the deconvolution of the different, compound processes. On the basis of this information, physico-chemically-meaningful equivalent circuit models can be set up wherein each circuital element represents an identified process, as shown in Fig. 6.

Once a generally valid model is obtained, dedicated fitting algorithms can then approximate the resistance and capacitance values of each element in the equivalent circuit [35,37]. Through rearrangement of the governing equations, quantification can take place for the fundamental physical and chemical parameters that must be used in the mechanistic models (see section 3.3). This is a crucial step in the transfer of experimental measurements to process and component modelling, avoiding excessive reliance on sources of literature that are unclear or unquestioned in terms of reliability or applicability. This enables closer collaboration between experimental and simulation experts, whereby the latter

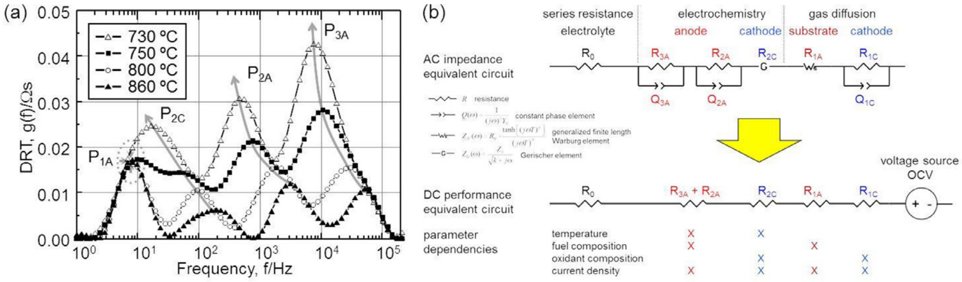

Fig. 6. (a) Example of DRT analysis of EIS spectra at different operating conditions, identifying constituent processes on the basis of which an equivalent electrical circuit can be formulated and quantified. (b) Equivalent circuits used for the 0-D cell model, AC impedance equivalent circuit (top) to obtain model parameters by means of impedance spectroscopy and complex nonlinear least square-fitting and DC performance equivalent circuit (bottom) to simulate current-voltage characteristics [35,36].

require accurate data on which to build their models, while the former require physically-sound verification of their measurements.

Nevertheless, many unsatisfactory EIS models are still employed. It is quite common to set up equivalent circuits based on a larger number of elements, which can easily be fitted to any measured spectrum. An excellent agreement of a small series of measurements with the model does not guarantee the correctness of the model (as any additional equivalent circuit element added to the model will further decrease the model error) and the interpretation of the various fitted values is debatable. A more rigorous approach using physico-chemically-meaningful models is recommended where all, or at least most, of the model parameters can be determined independently without fitting, as successfully applied in the work of Dierickx *et al.* [38].

A different approach to understand electrochemical processes in the cell using impedance spectroscopy, is based on elementary kinetic modelling. Impedance spectra can be simulated by means of elementary kinetic models, i.e., the spectra (as well as DC polarisation curves) can be calculated using appropriate sets of transport and reaction equations as described in Bessler *et al.* [39-41]. Despite their complexity, such models can reproduce experimental data and correlate features of the spectra to physicochemical processes in the cell.

1.2.3. Characterisation of state: Gas composition, pressure and temperature measurements

Besides the characterisation of the electrical performance of the SOC cell/stack assembly, in experimental programmes of research, it is important to accurately monitor and record the temperatures of the test specimens, as these can greatly influence response. Conditions in an experimental set-up will necessarily be different to those in an autonomous, field-tested or commercially operating system. Short stacks and single cells are tested in furnaces that impact the operating temperature inside the cell/stack housing and provide different boundary conditions to those in large insulated stacks that generate sufficient heat to be thermally self-sustaining. However, in contrast to a closed ‘end-use’ system, experimental rigs offer the possibility of introducing a number of thermocouples in key places where real measurement can be of vital importance to gaining proper insight into the occurring *operando* processes. The electrolyte temperature can also be inferred, based on the temperature dependence of its high frequency impedance [42].

It is very important that in experimental setups there be adequate pre-heating of the reactants to the nominal operating temperature of the stack or cell. The gas temperature should be measured at the inlet and outlet of the cell/stack by using thermocouples placed in the gas stream near the electrode gas supply/exit port of the cell/stack assembly unit. Thermocouples should be placed, where accessible on the cell/stack: this means at least in connection with the end plates that enclose the tested unit, but more invasive measurement can give better ideas as to the temperature distribution across the cell surface area from inlet-to-outlet. Temperature inhomogeneity is one of the most important reasons for SOC degradation. As regards the localised measurement of temperature, innovative approaches have been demonstrated lately at cell level, such as the one employed by Silva-Mosqueda *et al.* [43] in which thermocouples were distributed in the X and Y axes of the fuel electrode of a single cell and temperature gradients were obtained in 2-dimensions. This solution is analogous to the one proposed by Guk *et al.* [44] for measuring the temperature in the air electrode. At the stack level, Tallgren *et al.* [45] proposed an indirect method to monitor temperature distributions of cell clusters by using EIS measurements. However this method cannot be used to measure temperature gradients at the electrode level. Some information about temperature measurement may be found in [46-49]. In principle the thermocouples can be also inserted directly into the air channels. The risk of short circuit and leakage through the sealant (in the case of a closed manifold) is high, but the measurement is possible. This is easier for stacks with open air manifolds. Yan *et al.* [50] consider the use of optical fiber sensors to gather temperature information

As concerns the water content in the cell/stack when tested in a laboratory furnace, cold-spots may become an issue when employing prototype housings or test rigs enabling localised spot-samplings of gas composition in real-sized specimens, especially when the measuring equipment is placed outside the furnace at ambient temperature. A sound management of temperature is important to control steam content, and avoid condensation which in turn may lead to undesirable local pressure gradients [51].

Gas composition measurement is important when compound gases are utilised, such as reformate (in SOFCs) or in co-electrolysis (in SOECs). The electrode gas composition should be sampled near the electrode gas supply and/or exit port and analysed, for example, using infrared spectroscopy, mass spectroscopy and/or gas chromatography. At the air electrode, oxidant concentration can be measured using an amperometric lambda sensor. The gas sample should be transported from origin to point-of-analysis in a manner that minimises changes in composition (i.e., short heated sampling lines). Water content can be difficult to manage, as many analysis instruments do not tolerate condensed water.

Finally, reactant pressure fluctuations can also give rise to significant alterations of the recorded cell voltage. It is good practice to measure the differential pressures between the inlet and outlet of each electrode and water condensation at the outlet should again be carefully managed to avoid backpressure effects. A pressure sensor, manometer, Bourdon tube, or similar instrument may be employed. The measuring instrument should be located in such a manner that the uncertainty is minimised with respect to any pressure loss within the piping.

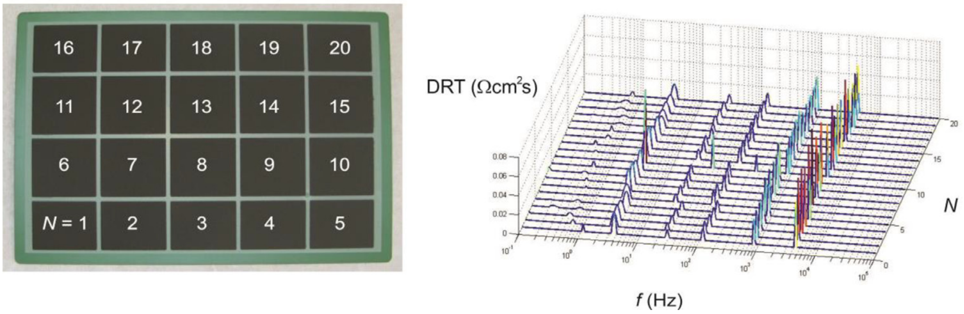

Fig. 7. Example of a segmented cell for local electrochemical measurements such as EIS, and the resulting DRT map. Courtesy of École polytechnique federal de Lausanne [52,53].

1.2.4. In-situ characterisation: Segmented cells and local probing

Many characterisation techniques are applied to the entire cell (or stack) and do not take into account the spatial differences of local conditions in an operating cell. There will always be a profile of conditions (through the electrochemical reactions and associated cell response) from the inlet to the outlet of the reagents fed to the cell. It is exactly this differential of state over the thin plane of the cell that can lead to locally-critical conditions (hot spots, fuel starvation, nickel reoxidation, mechanical stress, etc.) that cannot be detected in a "black box" set-up such as an average test facility. To overcome this, so-called segmented cells and stacks have been developed for individual assessment of the different zones across an operating SOC. Here, the air electrode layer is printed as mutually-electrically insulated segments over the entire cell area, allowing the ability to individually measure distinct areas of the cell and the electrical response of each in the overall flow field. Being able to carry out EIS and subsequent deconvolution via DRT analysis on all segments allows for monitoring of the degradation rates associated with each electrochemical process as distributed over the active area of the cell, see Fig. 7.

Other laboratories have developed test set-ups where local gas and temperature measurements can be taken, *in-operando*, to map the evolution of chemical reactions across the active cell area in steady-state and transient conditions [54,55]. These techniques add considerable information to the local conditions determining the electrochemical performance of, and degradation in SOCs, and can be used to generate statistical multivariate models correlating localised conditions with global settings, as well as to validate CFD models.

1.2.5. Optical in-situ characterisation

Another approach to obtaining spatially resolved measurements from within an operating SOC is to employ optical methods, obtaining non-intrusive in-situ experimental data of the occurring phenomena. Pioneering work in this respect was carried out by Lu *et al.* [56]. The simple mapping of temperature distribution and variation of the optically exposed electrode, for derivation of the reactions occurring and identification of hot spots can be carried out by infra-red imaging [57,58], but chemical analysis of formed species; either on the surface, or in the reacting gas phase requires the utilisation of Raman spectroscopy [59]. To facilitate optical access, the test section is closed off with quartz material, and then placed in a furnace with appropriate openings for both the laser light source and the optical sensor. In addition to the accurate alignment of the laser beam, care must be taken not to damage the transparent section, as well as not to generate reflection noise. Adequate sealing can be a major challenge, due to the fragility of the glass surface and the high temperatures acting on different materials in the set-up. For these reasons, most work to-date has been on button cells, though more recent studies have also considered for channels, thus monitoring the evolution of the reactant composition [60,61]. Though a highly artificial environment, by nature, due to the complexity of the experimental set-up for optical in-situ measurement, the resulting data can be particularly useful for validating detailed models of reforming and SOC oxidation/reduction processes.

1.3. History of continuum scale SOC modelling

The operation of an SOC-stack is driven by a number of complex, interconnected phenomena occurring at multiple length scales and in different parts of the cell, as shown in Fig. 8. It is impossible to experimentally examine microscale phenomena taking place in a porous electrode structure inside the stack. Even operando methods such as impedance spectroscopy average over the cell area and cannot describe local phenomena. In this sense, numerical modelling, including coupled electrical and electrochemical, thermal, fluid dynamics and mechanical sub-models, is becoming an ever more crucial tool for the prediction of global and local physical phenomena within the different parts of the cell [62]. For instance, the current-density distribution in a cell, the temperature gradient in a stack, or gas concentration in an electrode are difficult to obtain experimentally, but can readily be predicted in a model study.

In this respect, the primary focus of the present paper encompasses the state-of-the-art and best practices related to the modelling of SOCs at the continuum scale level, which reduces to single cells, SRUs and stacks, with some attention to micro-scale work. While significant development in modeling detailed electrochemistry done over the past 20 years are recognized, beginning with the pioneering work of the Gauckler group on model electrodes and their mechanisms, see Bieberle and Gaukler [63], continuing with an international group of scientists developing elementary kinetic models (in alphabetical order: Adler, Bessler, Deutschmann, Goodwin, Jackson, Kee, and others) see DeCaluwe *et al.* [64] and references therein, culminating in the ongoing development of the open-source chemistry software, Cantera [65,66]. In single cell to stack modelling detailed reaction kinetics [67] and elementary kinetic electrode models [64] have to be simplified to reduce computing time. As we are focusing on continuum scale models in this review, modelling on an elementary kinetic electrode or even model-electrode level will not be considered. It is important to note that these simpler types of models have already been confirmed to be suitable for engineering design optimisation purposes while limiting the amount of testing required for verification. For instance, Peksen *et al.* [68,69] used a 3-D model of an SOFC stack to improve the design of the pre-heaters, while Rashid *et al.* [70] modelled several manifold designs of a flat-tubular SOFC stack converging towards an optimal geometry capable of increasing the nominal stack power by 8%. Bi *et al.* [71] identified a key geometric

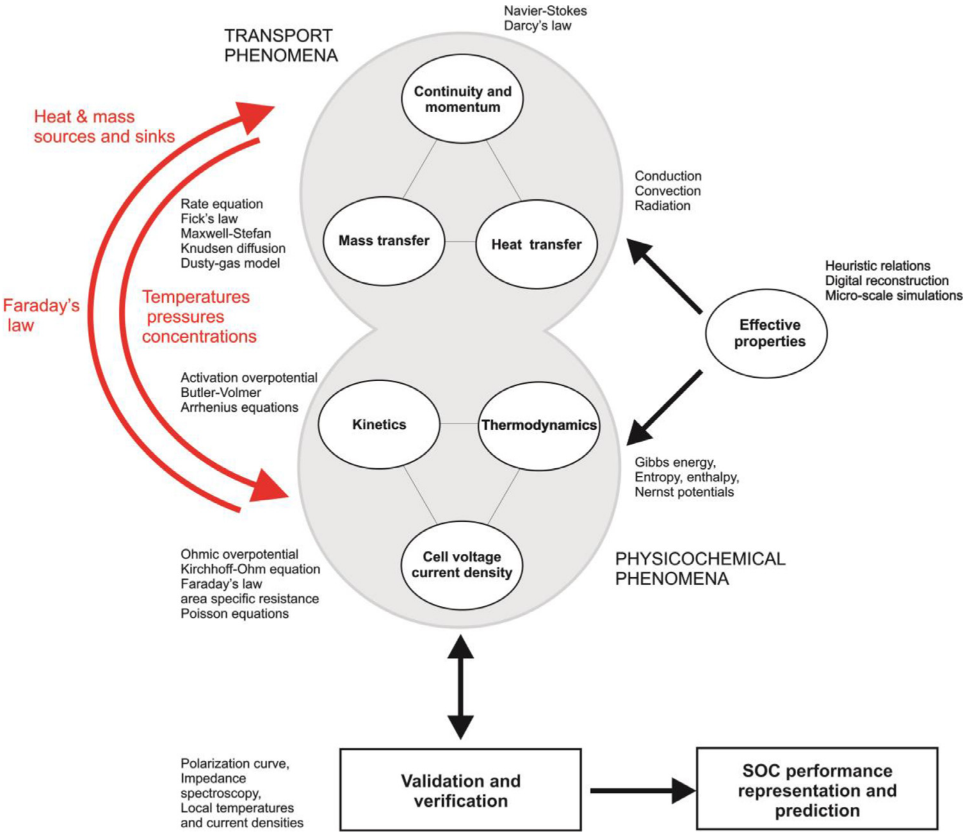

Fig. 8. Modelling scenario for SOCs.

design parameter to improve the flow uniformity of the planar SOC stack by CFD simulations of the flow fields in the SOC stacks. Liu *et al.* [72] used a model to analyse the trade-off between ohmic and concentration overpotentials and proposed an interconnected rib design to improve output. Chen *et al.* [73] were able to diminish concentration losses of an SOFC SRU by analysing different interconnect designs using a CFD model, together with the Taguchi method.

The 1990s witnessed the advent of the first CFD-based fuel cell models incorporating fluid flow phenomena coupled with electrochemistry. These were relatively simple and 1-D, and it was not until 1994 that a transient 3-D model of an SOFC was developed by Achenbach *et al.* [74]. Ferguson *et al.* [24] studied the effects of heat and mass transfer in a planar SOFC by means of temperature-dependent empirical mathematical expressions, while Bessette *et al.* [75] verified that extrapolating results obtained from the numerical model of an SOFC SRU to predict the outputs for a stack is imprecise, as was subsequently confirmed by Beale and Zhubrin [76]. Chan *et al.* [77] developed a model with the Butler-Volmer equation, Eq. (64), below. In 2003, Recknagle *et al.* [78] developed an SOFC stack model with an empirical electrochemistry model and used it to study the effects of flow configuration on the temperature distribution and power output of a 1-cell planar SOFC stack. Khaleel *et al.* [79] illustrated a finite element method (FEM)-based SOFC model for analysing a methane-fuelled 30-cell stack, with simplified fluid-electrochemical-chemical modelling.

Khaleel *et al.* [80] outlined a multiscale electrochemistry modelling scheme by considering the effect of electrode microstructure on electrochemical performance at the continuum level. Janardhanan and Deutschmann [81,82] introduced a heterogeneous multistep mechanism for steam reforming of methane, hydrogen and carbon monoxide in the Ni/YSZ electrode of an SOC. This approach has been used by other groups, Zhu *et al.* [83]. Kim *et al.* [84] proposed a multiscale materials modelling method by considering the effects of microstructure evolution on effective material properties and SOFC performance at the continuum scale. Shi *et al.* [85] developed a 2-D model, capable of considering the effects of heterogeneous electrode properties.

The development of 3-D multi-cell stack models with realistic geometric details is another major effort for enhancing SOFC continuum modelling capability. Beale and Zhubrin [76] presented a stack model based on volume-averaging which the authors referred to as a distributed resistance analogy. Sudaprasert *et al.* [86] developed a multi-physics-coupled stack model to simulate the operations of a 5-cell SOFC stack, but the cell size was relatively small. More recently multi-physics models for production-scale SOFC stacks have been successfully developed [87-89]. Li *et al.* [90] performed multi-physics simulations of the operations of a 30-cell stack with an electrochemically-active area of 144 cm^2 in a single cell. Nishida *et al.* [89] presented a multi-physics stack model with extensive experimental validation on an 18-cell stack with an effective electrode area of 361 cm^2.

With the growing number of papers on modelling of SOCs, review papers started to appear. Kakaç *et al.* [91] published a comprehensive review on the activities of SOFC macro-modelling in 2007. In 2008, Colpan *et al.* [92] presented another literature survey and pointed out the need to increase model accuracy. Updates on the progress of SOFC modelling continued to appear [93-97]. Andersson *et al.* [93] made a review on the development of multiscale chemical reactions coupled with transport phenomena in SOFCs. Grew and Chiu [97] presented a review on numerical techniques and their applicability across the length and time-scales for SOFC modelling. In 2015 Peksen [98] considered thermomechanical modelling in SOFCs.

Recent reviews on SOFC modelling includes the work by Bao *et al.* [99] on the model-based control of SOFC-gas turbine hybrid systems, as well as the work by Zabihian and Fung [100] that explains the fundamental bases behind different modelling approaches. In the field of mesoscale modelling, recent development focuses on methodologies for porous media, electrochemistry etc., for example, the work by Torabi *et al.* [101] that describes recent development of the second law investigations and analyses in thermal and chemical porous media systems. The work by Ryan and Mukherjee [102] describes the challenges, state-of-the-art and path forward in mesoscale electrochemical energy systems modelling, see Fig. 1, and their application to various design and operational issues in SOFCs, PEFCs, lithium ion batteries as well as metal-air batteries. Tjaden *et al.* [103] review a diverse range of methods that have been developed to extract the tortuosity of electrochemical devices.

Recent modelling activities on SOFCs are still carried out on various length scales, on the cell scale, a new design (double-sided cathodes) was modelled by Jiang *et al.* [104]. Kim and Lee [105], Wang *et al.* [106], and Zeng *et al.* [107] focused on the thermal stresses using commercial software. Muramatsu *et al.* [108] developed a simulation method to calculate non-stationary distributions of the chemical potential of oxygen in a SOFC under operation. Studies are also still performed on using new fuels for SOFCs such as ethanol [109]. On a system scale, research is carried out on a combined heat, hydrogen and power system [110] with various chillers [111], on integrating SOFCs with various battery technologies [112] on SOFC integration in unmanned aerial vehicles [113] and on SOFC-gas turbine systems [114].

With regard to SOECs, models ranging from 1-D to 3-D have been developed. In addition, models focusing on H_2O electrolysis, CO_2 electrolysis and H_2O/CO_2 co-electrolysis are also to be found. Ni *et al.* [115,116] developed a 1-D, steady-state model of a reversible SOC with an oxygen ion-conducting electrolyte and proton-conducting electrolyte. It was found that, in terms of electro-chemical performance, the cathode-supported configuration is the optimal design for SOCs in both SOFC and SOEC modes. As mentioned previously, in an SOFC the cathode is the air electrode, whereas in a SOEC it is the fuel electrode. Udagawa *et al.* developed a 1-D model of an SOEC stack comprised of cathode-supported solid oxide cells operating in steady state [117] and dynamic conditions [118]. The 1-D models are useful for predicting the electrochemical behaviours of button cells, but for practical operation, composition and temperature variations along and across the gas channels are 2-D or 3-D models required. A series of 2-D thermo-electrochemical models were developed by Ni *et al.*, considering the fluid dynamics, heat transfer, chemical reactions and electrochemical reactions in SOECs used for H_2O electrolysis [119], CO_2 electrolysis [120] and H_2O/CO_2 co-electrolysis [121]. 3-D SOEC models were developed by Hawkes *et al.* [122]. Choi *et al.* [123], meanwhile, adapted an existing 3-D SOFC model [124] to obtain results for an SOEC.

In terms of SOEC reviews, Ni *et al.* [125] published a review on high temperature SOECs, including both materials development and modelling efforts. In 2012, Laguna-Bercero published a review of the recent advances in high temperature SOECs [11]. The present review is focused more on the linkages between experiment and modelling, as well as the detailed origin of the modelling equations by phenomena and the various approaches used for both fuel cells and electrolysers alike.

Even if there are large numbers of scientific papers concerning the modelling of fuel cells, and to a lesser extent electrolysers, only a limited number of them directly tackle the problem of obtaining the physical parameters and coefficients by concomitant experimental results rather than from the literature or by hypothesis. A methodology for bridging experimental and modelling fields has been given by Leonide *et al.*, where EIS and equivalent circuit modelling (ECM) are used to deconvolute the electrochemical processes at the anode and cathode [126] and subsequently to parameterise an incremental cell model [35], which has been applied in gas channel and repeat unit models [127]. Gong *et al.* [128] used an adaptive differential evolution algorithm to identify the parameters of a simple 1-D SOFC model, while Tade *et al.* [129] proposed a technique for estimating the electrode charge transfer coefficients from polarisation curves. With regard to the characteristics of composite electrodes, Reiss *et al.* [130], Ni *et al.* [131] and Bertei *et al.* [132] proposed innovative methodologies to analyse the microstructural properties of the electrodes and apply them to continuum models in order to understand variations in the cell performance.

1.4. Model dimensionality and scale

Modelling work represents numerous levels of simplifications, with the aim of striking a balance between available computational power and the details of the phenomena to be investigated. Although available computational power has increased dramatically, there is still a need to strike a balance; the microstructural details of a cell might be important in certain macroscopic studies, while such details might be less important in the understanding of the response of an entire stack. In terms of dimensionality and scale, some comments will now be made that are relevant for the discussions throughout the whole article.

The book by Kulikovsky [133] contains analytical solutions to non-dimensional equations for a variety of fuel cell types. These solutions may be used for model verification and to ‘get a feel’ for the problem, but it is doubtful that they could be used to design a real SOC geometry. For that, more detailed 3-D models, often based on the finite volume method (FVM) or FEM, are typically employed. As early as 2002 and before, private sector SOC manufacturers were modifying commercial CFD codes to perform detailed 3-D calculations on single cells and stacks of up to 50 cells with computational meshes of 10^6, in parallel (up to 40 cores), for design purposes [15]. However, only recently the idea of using cell-scale codes to perform calculations on stacks has come within the realm of possibility. For stacks, volume-averaging techniques are employed, together with some of the closures described below, to reduce the required memory and run time; see section 2.11. The focus in this review is primarily on cell-scale models and their characterisation and validation. Continuum models of transport phenomena and electrochemistry in SOCs can range from simple to complex in terms of detail, and from microns to meters, in scale. Simple 0-D and 1-D models are useful as sub-scale models in larger system-level codes, and as education tools. As computer speed and memory size improve, the granularity and fidelity of numerical modelling are proportionally increasing. Fig. 8 illustrates the various processes to be considered in the construction of a mathematical model of an SOC, in particular the interaction between transport phenomena; fluid flow, heat and mass transfer, electric and chemical-kinetic phenomena. At each scale, it is usually necessary to prescribe closure terms and effective material properties that are often themselves obtained from detailed sub-scale models, empirical correlations or analytical/semi-analytical methods. Beale *et al.* [134] distinguish between ‘presumed flow models’, where only species continuity and energy are solved, and ‘detailed numerical models’, where momentum conservation and detailed transport equations are employed with fine meshes. The model of Achenbach [74] fell into the former category: Perfect mixing of the gases was assumed, so there were no cross-wise concentration gradients.

Many early SOC models contained little or no electro-kinetics at all: At elevated temperatures, it was considered that the reaction rates were sufficiently fast that kinetic (activation) losses could be lumped-in with the ohmic losses as an 'area specific resistance' (ASR), for which there is a semi-theoretical basis at low current densities (see section 2.5.1). This approach yielded reasonable results in comparison with experiments that display approximately linear polarisation curves. The paradox with the ASR approach is that without a reaction there would, of course, be no current, however the approach is valid provided the reaction rate is linearly proportional to the voltage reduction. Many authors treat the electrodes as being infinitely thin, although there is evidence that the finite thickness of the electrodes affects the kinetics. Simpler models treat the current density in the electrodes and the electrolyte of planar SOCs as being 'locally 1-D'. Under these circumstances, it is not necessary to solve for the electronic and ionic potential fields, section 2.4, but rather by combining Ohm's law with Kirchhoff's second law for the circuit, referred hereinafter as the Kirchhoff-Ohm equation, which relates the cell voltage, V, to the current density, i'':

$$V = E - i''R - \sum \eta \tag{6}$$

Eq. (6) states that the cell voltage, V, is the ideal or Nernst potential, E, minus losses, namely overpotentials $\eta = \eta_{\text{act},a}$ and $\eta = \eta_{\text{act},f}$, which are air electrode and fuel (feedstock) electrode activation overpotentials, discussed in section 2.9.1, while R is resistance and is to be considered a function of temperature $R = R(T)$ (see section 2.9.3). The issues of how to measure the values of R, E, etc. are further discussed below, in section 3. The reader will note that while V is a single value, the terms on the right-side of Eq. (6) are a function of its position in the cell plane (a 2-D model) and computational volumes (3-D) are only used for the flow and heat distribution, not for the electro-chemical reactions. If the ASR approach is adopted, R is an effective value, including activation losses, contact resistance(s), etc. implicitly, and under the circumstances $\eta_{\text{act},a} = \eta_{\text{act},f} = 0$. Otherwise, R is purely ohmic resistance and $\eta_{\text{act},a} \neq 0$, $\eta_{\text{act},f} \neq 0$. Many authors refer to an ohmic overpotential, $\eta_{\text{ohm}} = i''R$ (section 2.9.3). Eq. (6) is to be considered a basic equation that may be expressed in numerous different forms. Additional electrode overpotentials may be expressed explicitly, e.g., due to mass transfer (section 2.9.2) and electric resistance. Although in electrochemistry it is customary to refer to all electric potential losses as overpotentials, as is shown in Fig. 4(a); in modern 3-D computational models, mass transfer and electric resistance terms do not need to treated as such and may, for example, be obtained from the solution of partial differential equations. Conversely, for both single electrodes and electrode pairs, activation losses are usually expressed as local overpotentials.

The alternative to Eq. (6) is to solve for one or both of the electronic and ionic electric field potentials as state-variables in the volumetric domains of the electrodes, electrolyte and interconnectors (section 2.4). These will be referred to as single- and two-potential models. The electric field potentials drive the flux of e^- electrons through the load. A two-potential model accounts for the fact that fuel/oxidant gases are being consumed/produced by the electrochemical reactions in the through-thickness direction of the electrodes. The two potentials will co-exist together with the pore gas, within the electrodes, for a continuum scale model. As the reactions occur through the electrodes and with varying gas composition, the activation overpotential varies. These local quantities may also be needed to pinpoint incipient degradation phenomena [135,136]. However, this substantially increases the complexity.

Having decided on the model dimensionality (and different model components may be of different dimensionalities), at the heart of the issue is thermodynamics; a proper understanding of which is prerequisite. The level of model parameterisation, which equations are to be solved, how the system of equations is closed and what parameters must be measured in order to ensure the number of independent variables equals the number of model equations, must be taken into consideration. The end user faces a bewildering set of choices. Chemical and electrochemical kinetics (electrodics) must be taken into consideration, as SOCs operate at finite rates under non-equilibrium conditions. As a result, sources and sinks of electrical charge, chemical compounds, and heat arise; Faraday's second law of electrolysis, Eq. (2), converts charge production into mass sources/sinks, and heat sources/sinks are obtained from thermodynamic laws. These are required in the balance of mass, momentum and energy, whereas the arising values of temperatures, pressures and concentrations are required for the prediction of the thermodynamic, kinetic and electric quantities. SOC components contain a number of composite materials and porous layers. Effective property values must therefore be computed based on the best information at hand. All mathematical models should be thoroughly validated/verified using theory, other numerical methods, and physical experiments. These must be devised in such a manner as to be independent from the parameterisation of the model. When this cycle of interacting fields of science and engineering is complete, the fuel cell scientist has at his/her hands a tool capable of predicting the performance of SOCs. There is no 'one-way' but rather a myriad of possibilities that are improving over time.

2. Current continuum scale cell models

This section contains an overview of SOC models. The material is broken down according to subject matter in the sub-sections below; thermodynamics, transport, charge transfer, electrochemistry, chemistry and so forth. In each section the present state-of-the-art is presented together with discussions/recommendations as to best practices on a case-by-case basis.

2.1. Basic thermodynamics

Many of the items presented briefly in this section will be further expanded in detail later in the paper. In an SOFC, the oxygen reduction reaction (ORR) takes place at the oxygen electrode, while in an SOEC oxygen evolution takes place at the oxygen electrode, and the ORR takes place at the fuel electrode.

$$\frac{1}{2}O_2 + 2e^- \underset{SOEC}{\overset{SOFC}{\longleftrightarrow}} O^{2-} \tag{7}$$

At the (negative) fuel/feedstock electrode, if the fuel is H_2, the oxygen anions combine with a hydrogen molecule to form water:

$$H_2 + O^{2-} \underset{SOEC}{\overset{SOFC}{\longleftrightarrow}} H_2O + 2e^- \tag{8}$$

The overall reaction is thus:

$$H_2 + \frac{1}{2}O_2 \underset{SOEC}{\overset{SOFC}{\longleftrightarrow}} H_2O \tag{9}$$

Whereas hydrogen is a common SOFC fuel in the laboratory, almost all SOFC systems are nowadays operated with hydrocarbon-based fuels. The stack is commonly fed with preconditioned fuels, for instance partially reformed natural gas or reformates of higher hydrocarbons. Fuels such as syngas or even ammonia are possible as well. Carbon-based fuel components, such as carbon monoxide or methane, may react electrochemically at the fuel electrode, see Eq. (10). However, operation with such fuels may entail carbon deposition, leading to deactivation of the fuel electrode.

$$CO + O^{2-} \underset{SOEC}{\overset{SOFC}{\longleftrightarrow}} CO_2 + 2e^- \tag{10}$$

A more general expression may be written as follows:

$$\sum_j \nu_j R_j \rightarrow \sum_k \nu_k P_k \tag{11}$$

where R_j denotes reactant j, (H_2, O_2, etc.) and P_k denotes product k (H_2O, etc.). Variables ν (1, ½, 1 in Eq. (11)) are the so-called stoichiometric coefficients. Other homogeneous and heterogeneous reactions may be occurring simultaneously, for instance methane-steam reforming, water-CO shift reaction, and so on; these are further discussed below, in sections 2.6.1 and 2.6.2. In terms of thermodynamics, the cell potential is related to the electrochemical potential difference of the electrons in the two electrodes: $E^0 = (\bar{\mu}_{e^-}|_a - \bar{\mu}_{e^-}|_f)/z\mathrm{F}$. The electrochemical potentials can be related to the change in Gibbs free energy:

$$\Delta G = \sum_j (\nu_k \mu_k)_{\mathrm{prod}} - \sum_k (\nu_j \mu_j)_{\mathrm{react}} \tag{12}$$

which leads to an expression for the cell potential under standard conditions[4]:

$$E^0 = \frac{\Delta G^0}{z_i \mathrm{F}} \tag{13}$$

where z_i is the number of electrons transferred (equal to 2 for H_2). SOCs do not operate under standard conditions, therefore the Gibbs free energy may be corrected using:

$$\Delta G = \Delta H - T\Delta S \tag{14}$$

where T, S, and H are temperature, entropy, and enthalpy, respectively, $\Delta H = \sum_j (\nu_k H_k)_{\mathrm{prod}} - \sum_k (\nu_j H_j)_{\mathrm{react}}$, and $\Delta S = \sum_j (\nu_k S_k)_{\mathrm{prod}} - \sum_k (\nu_j S_j)_{\mathrm{react}}$. Individual species enthalpy and entropy are obtained as,

$$H_k = H_k^0 + \int_{T_0}^{T} c_p dT \tag{15}$$

$$S_k = S_k^0 + \int_{T_0}^{T} c_p \frac{dT}{T} - \int_{p_0}^{p} R \frac{dp}{p} \tag{16}$$

The species specific heat, c_p, are given as polynomials in T for SOC gases in Todd and Young [137], see also Hernando-Pacheco and Mann [138] The enthalpy of formation of the chemical reaction defined by Eq. (14) is ΔH= -247.3 kJ/mol at 1000°C, whereas the Gibbs energy of the formation is ΔG= -177.4 kJ/mol, the negative sign indicating that heat will be released at a rate of 69.9 kJ/mol. Thus, the potential goes from 1.229 V at 25°C to 0.94 V at 1000°C. The former value is for liquid water, while the value at 1000°C is for gaseous water. This means that there is less electrochemical energy as the temperature increases (or less additional potential is required for electrolyser mode). However, this decrease in potential is offset by the increase in the enthalpy of the gases. The entropic part is often referred to as reversible energy and represents the heat necessary for the reaction to proceed and can be calculated as the difference between the cell potential and thermoneutral potential, $E^H = \Delta H/2\mathrm{F}$, i.e., using Eq. (13) with the enthalpy not Gibbs free energy.

The cell potential is also impacted by concentration changes. The reversible (or Nernst) cell potential E may be written for an arbitrary electrochemical reaction as:

$$E = E^0 - \frac{RT}{zF} \ln Q \tag{17}$$

where Q is the reaction quotient

$$Q = \left(\prod_j c_j^{\nu_j} \right)_{\mathrm{prod}} / \left(\prod_k c_k^{\nu_k} \right)_{\mathrm{react}} \tag{18}$$

where c_j represent the concentrations of the products and c_k those of the reactants. As the air and fuel in an SOC are high-temperature gases, they can be treated as an ideal mixture:

$$pV = NRT \tag{19}$$

where R is the ideal gas constant, N is the number of moles and V is the volume. For an ideal-gas mixture, the chemical potentials are given by, $\mu_j = \mu_j^0 + RT \ln p_j$, where p_i are the partial pressures of species j, respectively. The chemical potential is the driving force in chemical reactions and mass transfer. The electro-chemical potential accounts for both chemical and electrical forces. It is defined by:

$$\bar{\mu}_j = \mu_j + z_j \mathrm{F} \boldsymbol{\phi} \tag{20}$$

where is the so-called Galvani potential. Using partial pressures and reaction stoichiometry, the Nernst equation, Eq. (17), is derived for the hydrogen/oxygen reaction with:

$$\mathrm{Q} = \ln \left(\frac{p_{H_2O}}{p_{H_2} p_{O_2}^{0.5}} \right) = \ln \left(\frac{x_{H_2O}}{x_{H_2} x_{O_2}^{0.5}} \right) - \frac{1}{2} \ln (p_a) \tag{21}$$

where x_i are the mole fractions at the electrode reaction sites (TPBs), section 2.9.2, and p_a is the air/oxidant electrode pressure. For practical reasons, E^0 in Eq. (17), is typically re-defined to include the last term on the right side of Eq. (21) at $p_0 = 1.01325$ bar. Under the circumstances, the latter term is replaced by a term of the form, $\frac{1}{2}\ln(1 + p_{\mathrm{gauge}}/p_0)$, where $p_{\mathrm{gauge}} = p_a - p_0$. This is equivalent to normalising the pressures with the air pressure, typically at a standard value of $p_0 = 1.01325$ bar. The latter form is useful when considering detailed transport models where the values of pressure and temperature vary. Generally speaking, changes in p_{gauge}/p_0 are usually small, and so changes in E are largely due to variations in mole fraction and temperature.

It is to be noted, assuming the fuel/feedstock side contains H_2O and H_2, a small amount of oxygen, O_2 (10^{-20} bar) is present on the fuel-side for equilibrium and the Nernst potential may be equivalently written as follows:

$$E = \frac{RT}{4F} \ln \left(\frac{p_{O_2,a}}{p_{O_2,f}} \right) \tag{22}$$

While Eq. (22) may be considered the more 'fundamental' form, it is Eq. (21) that is generally employed, since $x_{O_2,a}$ (air electrode) and $x_{H_2,f}$and $x_{H_2O,f}$ (fuel electrode) are readily available. When a current flows, reactants will be consumed and products produced, thereby changing the partial pressures of the components at the reaction sites from the equilibrium values.

It can be argued that by replacing $\ln(p_{O_2,a}/p_{O_2,f})$, Eq. (22), with $\ln(p_{O_2,a}) - \ln(p_{O_2,f})$, the latter should then be renormalised $\ln(p_{O_2,a}/p_{ref}) - \ln(p_{O_2,f}/p_{ref})$. Clearly the reference terms will cancel out, and may conveniently be chosen as unity, obviating unnecessary complications: Provided one starts with a non-dimensional expression, regardless of rearranging quotients as differences, the result will be always be the same, i.e., independent of the choice of units of p. The same logic may be applied to Eqs. (17), (18), (21), (23), (24). The Nernst potential for the CO oxidation in a fuel may be similarly derived as:

$$\mathrm{Q} = \frac{RT}{2F} \ln \frac{p_{CO_2}}{p_{CO} p_{O_2}^{1/2}} \tag{23}$$

where $E_{CO}^0 = \Delta G_{CO}^0(T)/2\mathrm{F}$ is the free-energy change of the reaction $CO + \frac{1}{2}O_2 \leftrightarrow CO_2$. For reduction/electrolysis, the quotient is simply reversed, $Q = p_{CO} p_{O_2}^{1/2} / p_{CO_2}$.

In Eq. (21), a single ideal or Nernst potential is formulated for the anode-cathode assembly. The Nernst potential can be considered the sum of two half-potentials at the anode and cathode, $E = E_a$ - E_f. However, the individual potentials cannot be measured

---

[4] The term 'standard conditions' is not without ambiguity. Here it is meant at constant reference pressure of 1 bar, but not at a standard temperature of 25 °C as is used for the terminology, elsewhere.

independently [139] and so the above potential is defined with respect to an arbitrary reference electrode. For two-potential models (see section 2.4), the Nernst potential for each of the electrode reactions are needed to determine the driving force at each electrode. These can be derived in a similar manner [135]:

$$E_a = E_a^0 + \frac{RT}{4F}\ln p_{O_2} - \frac{\mu_{O^{2-}}}{2F} \tag{24}$$

$$E_f = E_f^0 + \frac{RT}{2F}\ln\left(\frac{p_{H_2O}}{p_{H_2}}\right) - \frac{\mu_{O^{2-}}}{2F} \tag{25}$$

where $E^0$is the electrochemical potential of the electrode at a reference state, $E_a^0 = G_{O_2}^0/4\text{F}$,$E_f^0 = G_{H_2O}^0/2\text{F} - G_{H_2}^0/2\text{F}$, and $\mu_{O^{2-}}$ is the chemical potential of the oxide ions.

Carbon monoxide can be oxidised in the electrochemical reaction and also react with water, i.e., the so-called water-gas shift reaction (WGSR). In SOFC modeling, it is assumed in many models that that carbon monoxide is only reformed in the WGSR, i.e., one neglects the electrochemical reaction with carbon monoxide as reactant. Note that expressions for the Nernst potential for hydrogen and for carbon monoxide are developed for simplified mixtures with only one electrochemical reactant. Discussions on possible approaches to deal with electrochemical reactions when both hydrogen and carbon monoxide is present are found in in Andersson *et al.* [140] and Bao *et al.* [99].

Heat transfer is discussed in detail in section 2.7. For now, it is sufficient to note that heat is due to reversible and irreversible terms:

$$\dot{q} = \dot{q}_{\text{rev}} + \dot{q}_{\text{irrev}} = i(E^H - E) + i(E - V) \tag{26}$$

where i is the cell current, V is the operating potential and $E^H = \Delta H(T)/2\text{F}$is the thermo-neutral potential, Fig. 4. For an SOEC, if the cell voltage is between the enthalpy and equilibrium potentials, the reaction is endothermic, and is exothermic otherwise. For most SOECs, the reaction is endothermic at low-to-medium current densities. SOFCs are exothermic over the entire range of their operation.

In addition to defining the heat loss, one can also define a voltage efficiency for an SOFC, $\varepsilon = V/E$, as the operating potential, V, is the Nernst potential E minus the losses (and the efficiency is thus less than 1). The reason is that E is proportional to the free energy ΔG, and thus represents the energy input, whereas the operating potential V represents the (potential) work done by the cell (electrical power output).

For an SOEC, the efficiency is defined in terms of the energy output, i.e., chemical energy of the product, over energy input, i.e., electrical power. The water and CO_2 splitting reactions are both endothermic and thus both require electricity, ΔG, and heat, $T\Delta S$. The reaction heat can be supplied by the heat from the internal losses, or by preheating the gases. At the point where the internal resistances exactly balance the reaction heat requirement, the cell is operating thermoneutrally. Below the thermoneutral potential all the electrical power is converted to chemical energy, ΔH, and the efficiency is thus 100 %, assuming that all heat to be supplied electrically. In most cases heat from down-stream processes (e.g., from methanol or ammonia synthesis) is available, and by supplying this heat to the SOEC in terms of water vapour, the efficiency can go beyond 100 % (as the definition only accounts for the electrical energy input). If the potential is increased beyond the thermoneutral potential, E^H, then the cell is operating exothermally overall (adding the two heat contributions), and the efficiency is thus $\varepsilon = E^H/V$. The chemical energy of the product (e.g., hydrogen) is classically defined in terms of either the lower heating value or the higher heating value, where the latter also includes the heat of evaporation, although both defined at 25°C higher heating value is thus also rather close to the enthalpy ΔH only with the difference that ΔH is defined at the reaction temperature.

Eqs. (6) and (17) do not yet constitute a closed system of equations, as there are four unknown scalar fields, E, i'', $\eta_{\text{act},a}$, $\eta_{\text{act}.f}$, it being assumed that the cell voltage, V, or equivalently the total current, are prescribed. Therefore, additional equations are required for the activation overpotentials. These are described in section 2.5.1. In addition, the equations for mass transport (section 2.3), energy (section 2.7), momentum (section 2.2) and additional chemical reactions (section 2.6) must be solved.

2.2. Continuity and momentum

The overall continuity equation may be written equivalently in either mass or molar units [141], as:

$$\frac{\mathrm{D}\rho}{\mathrm{D}t} + \rho\,\text{div}\mathbf{u} = \frac{\partial\rho}{\partial t} + \text{div}(\rho\mathbf{u}) = \dot{r}''' \tag{27}$$

$$\frac{\partial c}{\partial t} + \text{div}(c\mathbf{u}*) = \dot{R}''' \tag{28}$$

where D denotes the so-called 'total' derivative, $\boldsymbol{u}$ and $\boldsymbol{u}^*$ are the mass-averaged and molar-averaged velocity and $\dot{r}'''$ is a volumetric mass source, for example due to chemical/electrochemical reactions in a porous media (but typically zero in the gas channels, where mass is conserved). For a mixture of components $\rho = \Sigma\rho_i$ is mixture density, defined in Eq. (32). In Eq. (28), $c = \Sigma c_i$ is total concentration and $\dot{R}''' = \mathrm{M}\dot{r}'''$is a molar source, typically non-zero, as moles are not conserved and M is a mixture molar mass. Generally speaking, the mass-form is preferred when detailed 3-D computational fluid dynamics (CFD) calculations are performed, as the velocity then corresponds to that in the Navier-Stokes and energy equations. However, both forms proliferate in the SOC community**.** Therefore, interconversion is frequently required. When electrodes are treated as being of finite thickness, the mass source/sink terms in Eq. (27) are obtained by summing the individual species source/sink terms, as outlined in section 2.3.

The mass balance, Eq. (27), and momentum transport equations are needed to close the system of equations to be solved. Although it is possible that the flow may be turbulent, for example in the manifolds of an SOC stack, generally speaking in the gas channels, the laminar Navier-Stokes equations are considered to apply:

$$\frac{\partial}{\partial t}(\rho\mathbf{u}) + \text{div}(\rho\mathbf{u}\mathbf{u}) = -\text{grad}p + \text{div}\mu\text{def}\mathbf{u} - \tfrac{2}{3}(\text{grad}\mu\text{div}\mathbf{u}) + \rho\mathbf{b} \tag{29}$$

where $\text{def}\mathbf{u} = u_{i,j}\hat{\mathbf{e}}_j$. If the flow (as opposed to the gas mixture) is treated as incompressible, then def**u** is replaced by grad**u** and $\text{div}\mathbf{u} = 0$ in Eq. (29): Not only are the Mach numbers trivially small, but also the rate of change of chemical species (mixture density, ρ) are also small. Body forces, $\boldsymbol{b}$, can also be neglected.

In the porous layers, either the superficial (filter) velocity, **U**, or the interstitial (pore) velocity, **u**, may be selected as a dependent variable. A momentum balance, for local void fraction, ε, would be

$$\frac{1}{\varepsilon}\frac{\partial\rho\mathbf{U}}{\partial t} + \frac{1}{\varepsilon}\text{div}\left(\rho\frac{\mathbf{U}\mathbf{U}}{\varepsilon}\right) = -\text{grad}p - F\mathbf{U} + \text{div}(\lambda\text{grad}\mathbf{U}) \tag{30}$$

where

$$F = \frac{\mu}{k_D} - \rho b|\mathbf{U}| \tag{31}$$

Some authors exclude the ε-terms; The implication is that the equation is valid for high mobility, μ/k_D (Darcy's law), and low mobility (Navier-Stokes) but is technically incorrect in the intermediate zones, Beale [142]. k_D is the absolute permeability, b is a Forschheimer (inertial) constant and $\lambda = \mu_{eff}/\varepsilon$ is a Brinkman number. The density can be calculated using.

$$\rho = \frac{p}{RT}\sum x_i \mathrm{M}_i = \frac{p}{RT}\Big/\sum \frac{y_i}{\mathrm{M}_i} \tag{32}$$

where M_i is the molar mass of species i. The dynamic viscosity of the mixture is calculated by employing the formula by Todd and Young [137], specifically for SOFCs, or the earlier work of Wilke [143].

In some cases the laminar flow in the flow channels can be described by Darcy's law through a volume averaged analogy. This is highly recommendable, as it significantly reduces the need for computational resources, allowing for swifter generation of results. The reader is referred to section 2.11.

2.3. Mass transport

The primitive forms of the individual species continuity equations are:

$$\frac{D\dot{n}''_i}{Dt} + \dot{n}''_i \mathrm{div}\mathbf{u_i} = \frac{\partial \rho_i}{\partial t} + \mathrm{div}(\rho \mathbf{u}_i y_i) = \dot{r}_i''' \tag{33}$$

$$\frac{D\dot{N}''_i}{Dt} + \dot{N}''_i \mathrm{div}\mathbf{u_i} = \frac{\partial c_i}{\partial t} + \mathrm{div}(c \mathbf{u}_i x_i) = \dot{R}_i''' \tag{34}$$

where $\dot{n}''_i$ is the absolute mass flux, $\dot{N}''_i$ is the absolute molar flux, ρ_i is the partial density of species i, c_i is the molar concentration and $\mathbf{u_i}$ is i-species velocity. $\dot{r}_i'''$ is a volumetric mass source of species i, for example due to chemical/electrochemical reactions in a porous media (typically zero in the gas channels) and $\dot{R}_i'''$ is a molar source of species i. There could be more than one reaction rate for a given species, for instance if CO is involved in the water-gas shift reaction (WGSR) and methane-steam reforming (MSR) reactions. It is not convenient to work with individual species velocities. Defining mass fraction, $y_i = \rho_i/\rho$, and mole fraction, $x_i = c_i/c$, the following identities are obtained:

$$\frac{\partial(\rho y_i)}{\partial t} + \mathrm{div}(\rho \mathbf{u} y_i) = -\mathrm{div}\mathbf{j}_i + \dot{r}_i''' \tag{35}$$

$$\frac{\partial(c x_i)}{\partial t} + \mathrm{div}(c\mathbf{u} * x_i) = -\mathrm{div}\mathbf{J}_i + R_i''' \tag{36}$$

where the mass-based diffusion flux is $\mathbf{j}_i = \rho_i(\mathbf{u}_i - \mathbf{u})$ and the molar-based flux is $\mathbf{J_i} = c_i(\mathbf{u}_i - \mathbf{u}^*)$

$$\sum_{i=1}^{n}\mathbf{j}_i = \sum_{i=1}^{n}\mathbf{J_i} = 0 \tag{37}$$

When electrodes of finite thickness are employed in a model, the mass sources/sinks are obtained from the exchange current density according to Faraday's second law of electrolysis, Eq. (2), expressed per unit volume $\dot{r}_j''' = \mathrm{sgn}(j) i''' M_j/z_j\mathrm{F}$, and $\mathrm{sgn}(j)$ is +1 for products and -1 for reactants. If the electrodes are treated as infinitely thin surfaces, the mass sources/sinks are generally treated as boundary conditions, with, $\dot{m}_i'' = \mathrm{sgn}(j) i'' M_i/z_i\mathrm{F}$. The total mass flux is obtained by summing the terms for the active species. The total flux, N_i, is composed of a diffusive term, $\boldsymbol{J_i}$, and a convective term, $c_i\boldsymbol{u}^*$. Eqs. (35)-(36) represent alternative forms for a system of unclosed equations. It is necessary to make a constitutive assumption. Both Fick's law and Maxwell-Stefan have been employed in the gas channels. The former is used in binary systems, while the latter is more suitable for multicomponent systems with significant differences in the molar masses of the species [95]. Fick's law can be written as:

$$\mathbf{j}_i = -\rho D \mathrm{grad} y_i \tag{38}$$

$$\mathbf{J}_i = -cD \mathrm{grad} x_i \tag{39}$$

The system of equations in Eqs. (38) and (39) are solved together with Eqs. (35) or (36), the Darcy-modified Navier-Stokes equations, Eq. (30), the energy equation (section 2.7), as well as additional equations describing chemical (section 2.6) and electrochemical (section 2.5) processes.

The simplest mass transfer analysis is to presume that at any boundary, a rate equation applies:

$$j_w| = -\rho D \left.\frac{\partial y}{\partial n}\right|_w = g(y_w - y_b) \tag{40}$$

$$J|_w = -cD \left.\frac{\partial x}{\partial n}\right|_w = g^*(x_w - x_b) \tag{41}$$

where g is a mass transfer coefficient and x_b, y_b and x_w, y_w are bulk and wall values (for readability, the subscript 'i' has been excluded. Imperfect mixing can then be accounted-for in even the simplest SOC models [144]. Both Eqs. (40) and (41) are valid for binary and dilute mixtures, as well as for concentrated multi-species mixtures where the binary diffusivities are similar in magnitude. For any given geometry, such as a channel or porous geometry, the mass transfer coefficient may be obtained from the correlations for the Sherwood number, Sh, or Stanton number, St, based on an analytical solution, numerical integration scheme [145], or as the result of a physical experiment. The Stanton number is typically correlated as a function of the Schmidt number, $\mathrm{Sc} = \mu/\rho D$ and Reynolds number, $\mathrm{Re} = uL/\nu$, where u is velocity and L is a length-scale. For example,

$$St = \frac{g}{\rho U} = \frac{\mathrm{Sh}}{\mathrm{Re}\cdot\mathrm{Sc}} = a\mathrm{Sc}^m\mathrm{Re}^n \tag{42}$$

The value of the exponent, m, determines how much the diffusivity, D, affects the rate of mass transfer. To illustrate: with m=-2/3, if D were increased 10-fold, this would result in g only increasing to 4.6 times the initial value. Thus, although the magnitude of the diffusivity, D, is important, the overall impact on mass transfer should not be overstated. While concentration gradients exist at all current densities, mass transport issues are most important at high mass fluxes/current densities; generally SOCs are seldom operated there, due to degradation issues. Fig. 4b shows the voltage reduction associated with concentration gradients, for a small 1cm^2 cell.

For ternary, quaternary and higher order mixtures of species, the binary species diffusion coefficients, D_{ij}, cannot generally be employed [146]. A number of methods for computing the diffusivity of a given species in a mixture, D_i, from the binary diffusivities, D_{ij}, e.g., Wilke [147]:

$$D_i = (1 - x_i)\left(\sum_{j\neq i}\frac{x_j}{D_{ij}}\right)^{-1} \tag{43}$$

which is, in principle, restricted to a situation in which a single species i diffuses in a stagnant multi-component. The binary diffusivities, $\text{Đ}_{ij} = \text{Đ}_{ij}(T, p)$, may be computed from mathematical correlations, for example Fuller *et al.* [148] and Poling *et al.* [149]. Only n-1 terms are required in Eq. (43), the n^{th} term being obtained from overall continuity, Eq. (27). A more detailed constitutive relationship is the so-called generalised Fick's law:

$$\mathbf{j}_i = -\rho \sum_{i\neq j} D_{ij} \mathrm{grad} y_i \tag{44}$$

$$\mathbf{J}_i = -c \sum_{i\neq j} D^*_{ij} \mathrm{grad} x_i \tag{45}$$

Unlike the binary diffusion coefficients, D_{ij}, the multi-component coefficients, D_{ij}, D^*_{ij}, are a strong function of local mass/mole fractions. These may be obtained from the mathematical inversion of the Maxwell-Stefan equations, Taylor and Krishna

[146], whereby the gradients are expressed as a function of the fluxes.

In addition to gas channels, SOCs contain porous electrodes/transport layers, details of which are not typically resolved in cell-level models, which necessitate the computation of 'effective' diffusivities and other properties, as described in section 2.8, below. Traditionally, concepts such as 'tortuosity' and 'tortuosity factor' [150,151] were employed to derive simplistic expressions for effective properties. A more recent approach is to independently perform detailed micro-scale simulations and employ volume-averaging on porous ensembles to generate property values [152]. This relies on advanced imaging methods being available to digitise typical geometries (see section 2.8).

The following equation describes the Maxwell-Stefan equations [153,154]:

$$\frac{1}{RT}\mathrm{grad}\,p_i = \sum_{\substack{j=1 \\ j\neq i}}^{n} \frac{p_j \mathbf{J}_i - p_i \mathbf{J}_j}{p D_{ij}} \tag{46}$$

where p_i is the partial pressure of species i, p the total pressure in the control volume and D_{ij} the binary diffusion coefficient between species i and j. To ensure flux consistency, Eq. (37) must be satisfied [155,156]. Eq. (46) may be conveniently written in terms of mole fractions:

$$\frac{\mathrm{grad}\,p_i}{p} = \sum_{j=1, j\neq i}^{n} \frac{x_i x_j \left(\mathbf{u}_j - \mathbf{u}_i\right)}{D_{ij}} \tag{47}$$

In the event that grad p is small (if it is not, this is added as an additional pressure-diffusion term), this may be conveniently rewritten in terms of the mole fractions as:

$$\mathrm{grad}x_i = \sum_{j=1, j\neq i}^{j=n} \frac{x_i x_j}{D_{ij}}\left(\mathbf{J}_j - \mathbf{J}_i\right) = \sum_{j=1, j\neq i}^{j=n} \frac{\left(x_i\mathbf{J}_j - x_j\mathbf{J}_i\right)}{cD_{ij}} \tag{48}$$

Following Taylor and Krishna [146], this may be considered a matrix equation, noting that only n-1 terms are independent owing to flux conservation, Eq. (37). Discarding the redundant nth equation for the chosen 'carrier' species,

$$c\,\mathrm{grad}x_i = -B_{ii}J_i^* - \sum_{\substack{j=1 \\ j\neq i}}^{j=n-1} B_{ij}J_j \tag{49}$$

where,

$$B_{ii} = \frac{x_i}{D_{in}} + \sum_{\substack{k=1 \\ i\neq j}}^{n} \frac{x_k}{D_{ik}} \tag{50}$$

$$B_{ij} = -x_i\left(\frac{1}{D_{ij}} - \frac{1}{D_{in}}\right) \qquad \forall j \neq 1 \tag{51}$$

The mass-based formulation[5] is:

$$\mathrm{grad}\left(y_i\mathrm{M}\right) = \frac{\mathrm{M}^2}{\rho}\sum_{\substack{j=1 \\ j\neq i}}^{n} \frac{y_i y_j\left(\mathbf{j}_j - \mathbf{j}_i\right)}{\mathrm{M}_j D_{ij}} \tag{52}$$

which may also be considered a matrix equation in n-1 equations, as above:

$$\rho\,\mathrm{grad}y_i = -A_{ii}\mathbf{j_i} - \sum_{\substack{j=1 \\ j\neq i}}^{j=n-1} A_{ij}\mathbf{j_j} \tag{53}$$

which can be inverted to obtain the generalised Fick's law in mass units $\mathbf{j}_i = \mathbf{A}_{ij}^{-1}\mathrm{grad}y_j$. In principle, it is possible to start with the evaluation of the n-1 binary Maxwell-Stefan diffusion coefficients and mathematically invert the n-1 equations to obtain the generalised Fick's law, Eq. (44):

$$\mathbf{j_i} = -\rho\left[\mathbf{A_{ij}}\right]^{-\mathbf{1}}\mathrm{grad}y_k \tag{54}$$

which is employed in popular CFD codes in use today. However, the matrix inversion is computationally expensive and numerical instabilities have been reported when numerous species are considered. Another approach, due to Kleijn *et al.* [157], involves implicitly inverting the diagonal flux terms to obtain a gradient, but explicitly leaving the off-diagonal terms as fluxes, n rather than n-1 equations are solved. Regardless of the methodology followed, substantial additional computational effort is added, as compared to a simple formulation of Fick's law.

An order of magnitude analysis is suitable to ascertain whether the Wilke form of Fick's law approximates the Maxwell-Stefan formulation in SOCs. Following the approach of Krishna and Standart [158], it is possible to 'force' the Maxwell-Stefan formulation, Eq. (48), into a flux-gradient form, with $\mathbf{J_i} = -cD_i\mathrm{grad}x_i$, with:

$$D_i = \left(\dot{N}_i'' - x_i\sum_{k=1}^{n}\dot{N}''_k\right)\left(\sum_{j\neq i}\frac{x_j\dot{N}_i'' - x_i\dot{N}_j''}{D_{ij}}\right)^{-1} \tag{55}$$

The stoichiometric coefficients in Eq. (55) may be substituted for the molar fluxes at the electrodes, $\dot{N}_i'' = \nu_i$, where it is understood that the coefficients on the left-side of Eq. (11) are negative and those on the right-side are positive. This approach differs from the later approach of Krishna [159,160], where it is assumed that $\dot{\mathbf{N}}_i'' = -cD_i\mathrm{grad}x_i$, which is only appropriate for no net molar flux.

Table 1 shows a comparison of the diffusivities of the transferred substances based on the approaches of Wilke [147], Eq. (43) and Krishna and Standart [158], Eq. (55) for: (a) SOFC air composed of a ternary mixture of N_2, O_2, and H_2O; (b) SOFC fuel composed of a ternary mixture of N_2, H_2, and H_2O; and (c) SOFC fuel composed of a quinary mixture of H_2, CH_4, CO, H_2O and CO_2. The latter corresponds to the inlet fuel conditions employed for benchmark test 2 in the International Energy Agency task on the Modelling and Evaluation of Advanced Solid Oxide Fuel Cells, Achenbach [23]. It is assumed that H_2 and CO are consumed equally. Binary coefficients were evaluated using [148,149] at 1173 K and 1.01325 bar.

It can be seen that for (a), the ternary air mixture with a single transferred substance, oxygen, Eq. (55) identically reduces to Wilke's equation, Eq. (43), for the transferred substance diffusivity, D_{O_2}, lending confidence to using this calculation procedure at the air electrode. For the considered (non-transferred) phases, the mixture diffusivities computed by Eq. (43) are only the binary diffusivities. (b) For the ternary fuel mixture, Eq. (55) returns $D_{N_2} = 0$, which is clearly incorrect and due to the shortcomings of 'forcing' the formulation when there is zero flux and zero gradient. Attention is therefore restricted to transferred substances. The errors in the transferred substance diffusivities when comparing Wilke and Krishna and Standart are -9% and -6%, respectively. (c) For the quinternary mixture, however, for H_2O, there is a substantial under prediction of -37% for the mixture diffusivity, by the Wilke method.

At elevated temperatures, the ratio of the mean free path of the pore gas and the size of the pores is often such that Knudsen diffusion may be significant, and the molecules collide more frequently with the pore walls than with other molecules [77].

$$D_{ij}^{\mathrm{eff}} = M\left(\frac{1}{D_{ij}} + \frac{1}{D_{i,\mathrm{Kn}}}\right)^{-1} \tag{56}$$

where M is a geometric factor, further discussed in section 2.8. In the gas channels, $M = 1$, $D_{\mathrm{i,Kn}} = 0$, but in the porous electrodes

---

[5] Interestingly, although the Maxwell-Stefan equations are generally presented in terms of molar-based quantities in modern texts, the original formulations by both Maxwell and Stefan were mass-based.

Table 1
Comparison of mixture diffusivities.

	Species	ν_i	x_i	Eq. (43) D_i (cm²/s)	Eq. (55) D_i (cm²/s)	% Error
(a)	N_2	0	0.7	4.51	N/A	N/A
	O_2	1	0.2	6.49	6.49	0.0
	H_2O	0	0.1	3.28	N/A	N/A
(b)	N_2	0	0.2	4.88	N/A	N/A
	H_2	1	0.5	9.35	9.65	-3.1
	H_2O	-1	0.3	5.80	6.63	-12.5
(c)	H_2	0.5	0.2626	6.47	6.33	2.2
	CH_4	0	0.171	3.30	N/A	N/A
	CO	0.5	0.0294	3.16	3.06	3.3
	H_2O	-0.5	0.4934	4.02	6.40	-37.2
	CO_2	-0.5	0.0436	2.63	2.65	-0.8

$M < 1$, and $D_{i,\mathrm{Kn}} > 0$. Eq. (56) states that (i) the Knudsen and binary diffusion coefficients may simply be added harmonically, generally referred to as Bosanquet's relation [161-163] and (ii) that effective values of both Knudsen and binary diffusion scale by the same factor, M. The equation for the Knudsen diffusion coefficient takes the following form:

$$D_{i,\mathrm{Kn}} = \frac{2}{3}\bar{r}_p\sqrt{\frac{8RT}{\pi \mathrm{M}_i}} \tag{57}$$

where $\bar{r}_p$is the average pore radius in the porous matrix, the value of which is extremely important.

The dusty gas model, proposed by Mason and Malinauskas [163], explicitly takes into consideration the three different types of mass transfer mechanisms in a porous matrix: multicomponent bulk diffusion, Knudsen diffusion, and Darcy's law, and has been praised [164-165] as a mechanistic approach to model gas transport through porous media [166]. The general form, neglecting the effects of thermal diffusion, is expressed by means of the following equation:

$$\sum_{\substack{j=1\\ j\neq i}}^{n} \frac{p_i\dot{\mathbf{N}}''_j - p_j\dot{\mathbf{N}}''_i}{pD^{\mathrm{eff}}_{ij}} + \frac{\dot{\mathbf{N}}''_i}{D_{\mathrm{Kn}\,i}} = -\frac{1}{RT}\left(\mathrm{grad}\,p_i + \frac{k_0 p_i}{\mu D^{\mathrm{eff}}_{Kn\,i}}\mathrm{grad}\,p\right) \tag{58}$$

where D^{eff}_{ij} is the effective binary diffusivity between species i and j, $D^{\mathrm{eff}}_{\mathrm{Kn}\,i}$ the effective Knudsen diffusivity of species i, and k_0 is a molar permeability.

Attending to the relatively small volume of state-of-the-art SOC electrodes and to the complexity of the dusty gas model, most authors assume the viscous flux to be negligible, $\mathrm{grad}\,p \approx 0$. Then, a so-called modified Maxwell-Stefan model is obtained. The premise of $\mathrm{grad}(p) = 0$ is inconsistent with the DGM as this model inherently includes a variation of pressure throughout the porous electrode in its formulation, as shown by Bertei *et al.* [167]. Model validation for this was completed by Webb *et al.* [165] for binary mixtures with experimental data gathered by Evans *et al.* [168].

More recently, an approximation of the dusty gas model was derived by Kong *et al.* [169] in the form of a modified Fick's law. Several researchers have reviewed the use of simpler models to investigate their range applicability and validity. Fick's law based on Wilke's approximation can be extended to account for Knudsen diffusion. It has a tendency to overestimate the resistance for the mass transfer compared to the dusty gas model [170].

Research into a modified Fick's model (including the geometric M-factor, and Knudsen-modified binary diffusion coefficients [171] found no noteworthy difference from the dusty gas model for a wide range of the investigated geometries and operating parameters. Without Knudsen diffusion, the Maxwell-Stefan formulation is insensitive to the pore diameter and tends to underestimate the mass transfer resistance [170].

In the work by Bao *et al.* [172], the extended Maxwell-Stefan approach was found to overestimate the mass transfer resistance compared to the dusty gas model. Recommendations on when to apply different models were also provided by Suwanwarangkul *et al.* [170] Mention is to be made of the notable papers on the binary friction model [173] and the cylindrical pore interpolation model [174].

The newcomer to the field faces a disturbing array of choices from simple to complex, as described above. The choice will depend on the composition of the reactants/products and current density, Mass transfer is the rate-limiting factor at high current densities. At low to intermediate values, its importance is diminished. A Fick's law approach would appear sufficient at the oxygen electrode, whilst at the fuel electrode, depending on the components, an order of magnitude analysis can determine the appropriate method. Fortunately, modern general-purpose CFD codes (both commercial and open-source) typically allow for a choice of diffusion models to be implemented at run-time. The simpler models can then be benchmarked against the more detailed closures, easing the choice of diffusion model in each component of the electrochemical cell.

2.4. Charge transport

While one can assume that the cell potential can be equated with the Nernst potential less losses, as in the Kirchhoff-Ohm relationship, Eq. (6), this does not consider changes within actual electrode structures. Thus, further details on the overpotential variation and local concentrations through the electrodes can be obtained by modelling both the ionic and electronic potentials referred to in this paper as two-potential models [135,136]. It is tacitly assumed here that only O^{2-} ions and not e^- or H_2 gas are transported across the electrolyte (no leakage), which is generally not a serious problem for solid oxide devices. Volume-averaging, i.e., a 'homogenised' description, is typically employed in the electrodes, with electronic and ionic charges coexisting within the same computational volume, together with the gas species. Current densities in the electrodes and electrolyte are proportional to the potential gradients:

$$\mathbf{i}''_{\mathrm{el}} = -\sigma^{\mathrm{eff}}_{\mathrm{el}}\mathrm{grad}\phi_{\mathrm{el}} \tag{59}$$

$$\mathbf{i}''_{\mathrm{io}} = -\sigma^{\mathrm{eff}}_{\mathrm{io}}\mathrm{grad}\phi_{\mathrm{io}} \tag{60}$$

where φ_{el} and φ_{io} are the electronic and ionic potentials and $\sigma^{\mathrm{eff}}_{\mathrm{el}}$ and $\sigma^{\mathrm{eff}}_{\mathrm{io}}$ are the effective conductivities of the phases in the electrodes and interconnectors, and the electrodes and electrolyte. The starting point for the conservation equations is the Nernst-Planck relationship, where it is presumed that the flux of charged particles is due to species convection, diffusion, and charge migration. In SOCs, only the latter is considered significant and the system

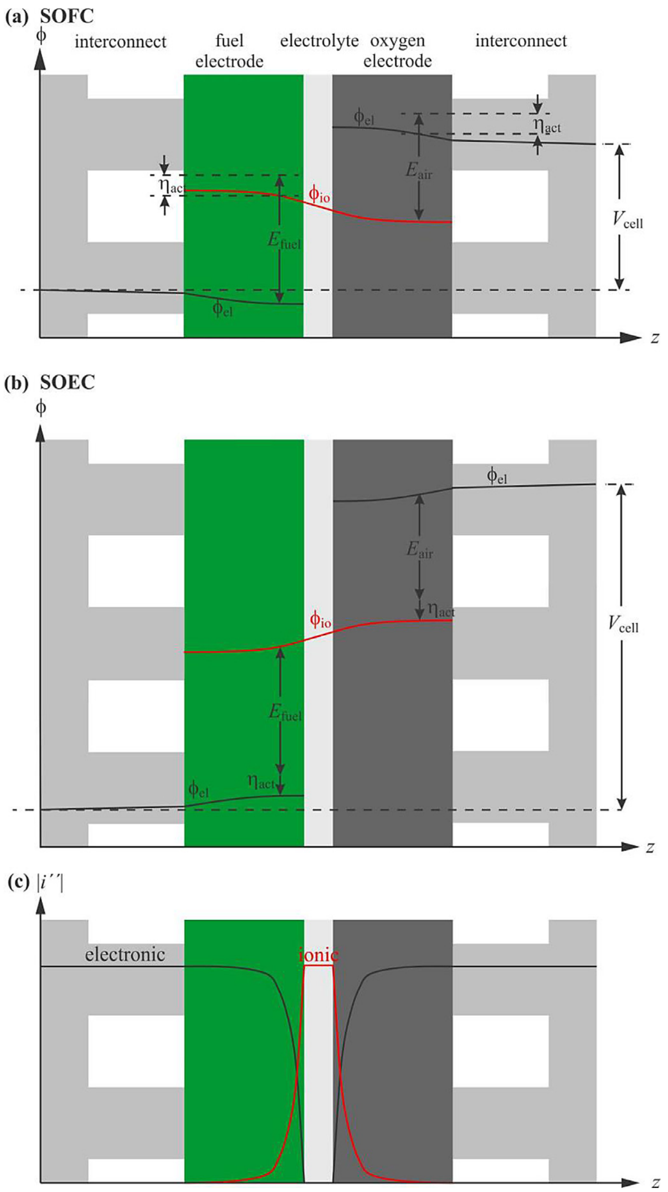

Fig. 9. Distribution of electronic and ionic potentialsacross a repeating unit of a stack and their interconnection through Nernst potentials of the half-cell reactions and activation overpotentials. (a) Fuel cell mode; (b) Electrolysis mode; (c) Current density magnitude, modified from Navasa et al. [136]. Not to scale.

reduces to Ohm's law expressed as a pair of coupled Poisson equations [62]:

$$\mathrm{div}\left(\sigma_{el}^{eff}\mathrm{grad}\phi_{el}\right) = \begin{cases} -i''' \ \text{ in the air electrode} \\ 0 \text{ in the interconnects} \\ i''' \ \text{ in the fuel electrode} \end{cases} \tag{61}$$

$$\mathrm{div}\left(\sigma_{io}^{eff}\mathrm{grad}\phi_{io}\right) = \begin{cases} \ \ i''' \text{ in the air electrode} \\ \quad 0 \text{ in the electrolyte} \\ -i''' \ \text{ in the fuel electrode} \end{cases} \tag{62}$$

The volumetric source terms of charge, $\pm\, i'''$ are given by the Butler-Volmer (or other) equation, as described in the next section. Clearly, $\mathrm{div}(\sigma_{el}^{eff}\mathrm{grad}\phi_{el}) + \mathrm{div}(\sigma_{io}^{eff}\mathrm{grad}\phi_{io}) = 0$. Eqs. (61) and (62) are a coupled, i.e., ϕ_{el} and ϕ_{io} are not independent, but are related via the source term, $\pm\, i'''$.

An illustration the variation of ϕ_{el} and ϕ_{io} in the through direction of the cell is shown in Fig. 9. Here, it is seen how ϕ_{io} is defined through the cell electrodes and electrolyte, although little variation is found other than in the active parts of the cell. The slope through the electrolyte is due to the transport of ions. The variation in the electrodes is partly due to the transport of ions, but also to the gradual generation/depletion of ions moving away from the electrolyte. ϕ_{el} is defined in the electrodes and interconnectors, and is discontinous, as it is not defined in the electrically-insulating electrolyte. Furthermore, due to the good electronic conductivity of the electrodes, the slope is very flat (little resistance entails a good distribution of the electric potential). The direction of the slope is the same as that of the ionic species (both species are negatively charged, and so travel in the same direction).

Generally-speaking, the boundary conditions for ϕ_{el} for at least two or more points in the interconnects may be either potentiostatic (Dirichlet), for example $\phi_{el}= 0$ and $\phi_{el} = V$, or mixed potentiostatic/galvanostatic (Dirichlet/Von Neumann), for example $\phi_{el}= 0$ and $\partial\phi_{el}/\partial n = 0$, whereas for the ionic potential the boundary conditions will be entirely Von Neumann, $\partial\phi_{io}/\partial n = 0$. Although it is possible to code 'jump' or 'slip' boundaries in Dirichlet form [175], this is seldom done in electrochemical codes, a recent exception being the work of Weber *et al.* [176].

ϕ_{io} is an algebraic function of ϕ_{el} and therefore, the problem is well-posed even without fixing ϕ_{io} at an interior point. However, initial values must be carefully chosen and relaxation employed, or convergence may be elusive. Alternatively, it is possible to enumerate the total current at both the air and fuel electrodes and scale the source terms if anodic and cathodic currents are not equal (block adjustment). These issues can be obviated by employing a coupled solution scheme for the two scalar variables.

In many cases a two potential model may not be necessary, if the objective is to understand the overall behaviour of a cell or a stack. In this case single potential models are easier and faster to implement, see section 2.5. The detailed resolution of the overpotential variation does however provide the opportunity to understand the reason for local degradation phenomena, which occur through the thickness of the electrode, see section 2.12.

The Kirchhoff-Ohm form for potential, Eq. (6), can be easily derived from Eqs. (59)-(60), as follows. Reactions and charge transfer are simplified to occur in an infinitely thin volume (a plane). Only one potential is needed, with the reactions at the electrode interfaces represented as potential jumps. Furthermore let σ be assumed to be constant.

$$\sigma\frac{d^2\phi}{dx^2} = 0 \tag{63}$$

with $\phi = 0$ at $x = 0$ and $\phi = V$ at $x = L$. Integrate and set $i = \sigma\phi/L$, where L is the electrolyte thickness, with $R = L/\sigma$ (or more correctly $R = \sum L_i/\sigma_i$ where the summation is conducted across the anode, electrolyte, and cathode), eliminating ϕ one may readily obtain Eq. (6). Thus, the assumption that the ionic charge flux is 1-D locally hinges on a number of premises and corresponds, rather loosely, with the 'segmented cell' employed in experimental measurements of local current density (see Fig. 7). The potential/voltage loss in the interconnector may similarly be written as $\eta = Ri''$where $R = L/S\sigma$, L is interconnect thickness and S is a (conduction) shape factor obtained by solving the Laplacian for the detailed ribbed (or other) geometry. Clearly, for planar geometry, $S = 1$.

2.5. *Electrochemical reactions*

2.5.1. *Electrochemical kinetics*

The relationship between the ionic and electronic potentials is given by a suitable electrochemical kinetic expression, such as the Butler-Volmer equation. This can be derived analytically for a single-step, single-electron transfer process based on Eyring's analysis (see Glasstone *et al.* [177]), on the assumption that the prob-

Table 2
Model parameters obtained through experimental appraisal/property tables, from [35,178].

Parameter	Value	Units	Equation
B_{ohm}	$4.1879 \cdot 10^{12}$	S•K/m^2	(99)
$E_{\mathrm{act,ohm}}$	90.31	kJ/mol	(99)
γ_{H2}	-0.1	-	(67)
γ_{H2O}	0.33	-	(67)
γ_{O2}	0.22	-	(67)
$i^{\mathrm{pre}}_{0,\mathrm{H}_2}$	$1.82527 \cdot 10^6 \cdot T$	A/m^2	(67)
$i^{\mathrm{pre}}_{0,\mathrm{O}_2}$	$1.51556 \cdot 10^8 \cdot T$	A/m^2	(67)
$E_{\mathrm{act,H2}}$	105.04	kJ/mol	(67)
$E_{\mathrm{act,O2}}$	139.86	kJ/mol	(67)
β_{an}	0.59	-	(64)
β_{cat}	0.65	-	(64)
$\mathrm{M_f}$	0.13	-	(56)
$\mathrm{M_a}$	0.022	-	(56)
p_{ref}	1†	Atm	(67)

† Pressures in Eqs. (67) are in Atm.

ability density for ions crossing the electrode follows a Boltzmann distribution:

$$i''_k = i''_{0,k}[\exp(A\eta_k) - \exp(B\eta_k)] \tag{64}$$

where $i''_{0,k}$ is the local exchange transfer current density at the k-electrode (air or fuel) and $n_e = 2$. For convenience, $A = \beta n_e \mathrm{F}/\mathrm{R}T$ and $B = -(1-\beta)n_e\mathrm{F}/\mathrm{R}T$ are defined. β is a forward reaction symmetric factor[6]: Values for the fuel and air electrodes of a Jülich Mark-F SOC, obtained by Leonide *et al.* [35,178], are given in Table 2.

Outside of the equilibrium region, the forward fuel cell reaction is much greater than the reverse electrolysis reaction $\exp(A\eta_k) > > \exp(B\eta_k)$ for a fuel cell. Then, the Butler-Volmer equation simplifies to the Tafel equation:

$$i''_k = i''_{0,k}\exp(A\eta_k) \tag{65}$$

The Tafel equation can be inverted to obtain an explicit expression of $\eta = \max[0, \ln(i''/i''_0)_k]/A$. Conversely, for small i''/i''_0, the Butler-Volmer equation may be linearised as follows:

$$i''_k = i''_{0,k}(A - B)\eta \; = i''_{0,k} n_e F\eta/RT \quad i''/i''_0 \tag{66}$$

For a multi-step, multi-electron reaction, the Butler-Volmer formulation is only considered approximate, not theoretically rigorous, with A and B independently fitted to experimental data. Eq. (64) is given in terms of current density, which is suitable for mathematical models in which the electrodes are treated as surfaces. If the electrodes are treated as volumetric regions of finite thickness, the equivalent expression is $i'''_k = ai''_k$, where $a = a_{12}$ is the specific interfacial area of the space-surface per unit-volume between the ionic electronic carrier in cm^2/cm^3 or, in SI m^{-1}. Kulikovsky [179] obtained a solution of the 1-D equations of Perry *et al.* [180] for the activation overpotential, η, in a 1-D polymer electrolyte cell electrode for the case $B = -A$, in Eq. (64). This provides a rationale to account for concentration changes in computing η in 3-D SOCs, employing a Kirchhoff-Ohm methodology.

The exchange current density can be expressed by means of an Arrhenius equation for both the electrodes [82]:

$$i''_0 = i^{\mathrm{pre}}_0 \prod_k \left(\frac{p_k}{p_{k,\mathrm{ref}}}\right)^{\gamma_k} \exp\left(-\frac{E_{\mathrm{act}}}{\mathrm{R}T}\right) \tag{67}$$

For the fuel electrode with H_2 as fuel, the product contains terms in H_2 and H_2O (for CO it contains terms in CO and CO_2) whereas for the air electrode, it is just O_2. i^{pre}_0 are pre-exponential factors, E_{act} are activation energies, p_{ref} are reference partial pressures normally equal to 101325 Pa. γ_k is the reaction order of species k. Values of i^{pre}_0, E_{act}, p_{ref}, γ_k for Eq. (67), as obtained by Leonide *et al.* [35,178] for a Jülich Mark-F SOC, may be found in Table 2. Note that the activation energy is a crucial parameter when describing the electrochemistry within a SOC, and a range of values between 100 and 190 kJ mol^{-1} is found in literature. The exchange current density is hard to differentiate and estimate, when two or more competing reactions occur at the same time. Notice that most published models in the continuum scale assume a single global charge transfer reaction; An alternative formulation is found in Zhu *et al.* [67] and Hecht *et al.* [181] who proposes a complex reaction order dependence of the exchange current density assuming that the charge transfer mechanism at the TPB is the rate-limiting factor, while the rest of the reactions: adsorption/desorption of H_2 on the nickel surface, adsorption/desorption of H_2O on the YSZ surface and oxygen ion transfer between the bulk and surface of the YSZ are in equilibrium. Similarly at the negative fuel electrode, the authors assume that the formation of O^{2-} ions and the subsequent incorporation into the electrolyte is the rate-limiting reaction in the positive (air) electrode. The electrochemical reactions are described by a five step elementary reaction mechanism by Lee *et al.* [182], among others.

Eqs. (17), (6) and (64) represent four equations in four unknowns, Nernst potential, E, two activation overpotentials, η_a and η_f, and current density, i''. These are to be considered a function of temperature and pressure, species mass/mole fractions and location. Thus, the system is fully coupled. Mass source and sink terms in the species and continuity equations, Eqs. (35) and (27), are prescribed from the local current density, via Faraday's second law of electrolysis, Eq. (2), whereas temperature, pressure and mass fractions are obtained from the solutions of Eqs. (73), (27), (35), and Eq. (30). Alternatively, the system of Eqs. (61)-(62) may be solved in place of Eq. (6), if more detail is required.

In this section the global reaction mechanisms that describe electrochemical kinetics were introduced. These describe the kinetics for modelling in the continuum scale, at a reasonable accuracy. More detailed kinetics may be obtained by using multiple step reaction mechanisms.

The reaction kinetics is mostly dominant at low current densities (activation), and for other type of electrochemical cells the non-linear form of the Butler-Volmer equation Eq. (64) can be used to capture the higher losses here. However, characterisation of an SOC for both electrolysis and fuel cell modes of operation shows that the i''-V curves are basically straight at low currents, see for example, [183,184], indicating that no particular activation losses are present at low current density. Eq. (66) can often thus be applied as a good approximation. Once again, the reader is faced with a dichotomy of opinions when trading off complexity and accuracy for the particular materials used in the SOC.

2.5.2. Electrochemically-active surface area

The oxidation of H_2 and/or CO (SOFC) or the reduction of H_2O and/or CO_2 (SOEC) occurs at the TPB, which is distributed in a thin volume, around 20-40 µm-thick. A larger TPB density results in additional reaction sites, or in other words, a smaller electrode activation polarisation. For the TPB to be active, all three electronic, ionic, and gas phases must form three continuous interconnected regions. If any subregion of a phase is not connected, the TPB cannot be supplied and becomes inactive. In the case of electrolyte-supported cells, Ni/Ceria cermets are favoured [185]. In these electrodes, the ionic conducting YSZ is replaced by doped ceria, a mixed ionic/electronic conductor in the fuel electrode environment. The electrochemical reaction is no longer limited to the TPB, as the reaction can occur across the ceria surface without the presence of a continuous Ni-matrix. Furthermore, ceria offers advantages with respect to sulphur tolerance [186] and carbon deposition [187]. Previous-generation air electrodes were of

---

[6] Some authors include $n_e = 2$ with the symmetry factors.

the composite type, the vast majority of them comprising LSM-YSZ. Nowadays, better performing electrodes are made with mixed ionic-electronic conductors (MIECs) such as LSCF and LSC.

Two distinct approaches regarding the numerical designation of the TPB in composite electrodes can be found in the literature [188]. The first, Costamagna *et al.* [189], hypothesises that the active sites are proportional to the contact area of intersecting electronic and ionic conducting particles and thus expressed as a surface area per unit volume ($m^2 m^{-3}$). This approach is suitable if the electron-conducting phase exhibits a sufficiently high ionic conductivity to transport ions from the surface to the interface and the charge transfer process at this interface is rate limiting. The second approach suggests that the reactions take place on the space-curve formed by the intersection of the electronic and ionic particles, hence being expressed as a length per unit volume ($m \cdot m^{-3}$) [190] and thus is suitable for cermets exhibiting a purely electronic conducting (metallic) phase, such as nickel.

Nowadays, microstructural properties expressed as volume fractions of different phases, particle size distributions, volume-specific surface and interface areas, and TPB lengths, are evaluated by means of tomographic methods and suitable algorithms to extract the desired parameters from the 3-D voxel image, as well as by artificially synthesising and analysing generated 3-D microstructures. For reasonable accuracy, the TPB region may be described as a surface area per unit volume, at the continuum scale. A more detailed approach may be of interest, at smaller length scales.

2.6. Chemical reactions

When a fuel mixture containing methane and carbon monoxide is supplied in SOFC mode, reforming reactions take place. Methane reacts with steam in the methane steam reforming reaction (MSR). Carbon monoxide reacts with water in the water gas shift reaction (WGSR), and can also be oxidised in the electrochemical reaction (see section 2.1). The WGSR takes place in the fuel electrode as well as in the gas channel (e.g., in the bulk flow), while the catalytically-dependent MSR takes place in the electrode, only.

The reforming chemistry can either be described with an elementary heterogeneous approach (as in Zhu *et al.* [67] with a reaction mechanism with 42 reaction steps), see also Hecht *et al.* [181], or according to a global kinetics approach (as in Andersson *et al.* [62,140]) with 2 reactions, i.e., the MSR and the WGSR). Since the focus of this paper is on the continuum scale, the reforming chemistry in sections 2.6.1-2.6.2 are described according to a global kinetics approach. Note that, the MSR reaction at SOFC operating conditions is far from equilibrium, i.e., kinetically controlled, compared to the WGSR that is thermodynamically controlled. There are various methods that describe MSR reactions at a continuum scale, for example first order kinetics, Langmuir-Hinshelwood kinetics, as well as higher-order kinetics [191].

2.6.1. Methane steam reforming

The steam reforming of methane,

$$CH_4+H_2O \leftrightarrow CO + 3H_2 \tag{68}$$

is thermodynamically favoured by high temperatures (strongly endothermic reaction) and low pressures [192], and may be written as an Arrhenius type equation,

$$\dot{r}''' = k \cdot p_{CH_4}^{m} \cdot p_{H_2O}^{n} \cdot \exp\left(\frac{-E_{act}}{RT}\right) \tag{69}$$

The reaction orders of methane and water, m and n in Eq. (69), are fitted to experimental data, with considerably different values possible [93]; m varies between 0.85 and 1.4. Both positive and negative values exist for n, depending on the operating conditions. The large discrepancies between the MSR reaction rates depend on the reaction being strongly dependent on the steam-to-carbon ratio, with various experiments having been carried out with significantly different values [193]. Different values of m, n, were recorded by Nguyen *et al.* [194]. A small steam-to-carbon ratio provides a positive reaction order for water. A ratio of around 2 yields reaction orders of water close to zero, while a high ratio provides negative values [195]. A comparison between different MSR reaction rates, implemented in the same model, can be found in Wang *et al.* [193] and Paradis *et al.* [193,196]. The various expressions describing the reaction originate from different sets of experimental measurements. An alternative to Eq. (69) is a Langmuir-Hinshelwood expression [197]. Haberman and Young's model [198] is also frequently used, when modelling the MSR reaction rate. Another set of empirical equations used regularly was proposed by Lehnert *et al.* [192]. The gas composition was that from the 1996 IEA SOFC benchmark [23], with methane as a fuel. Any correlation should agree with the data for the experimental conditions, mainly with respect to temperature and SC ratio. One of the advantages of the SOFC is the possibility to internally reform methane rich fuels, which also consumes some of the heat generated by the electrochemical reactions. A global MSR reaction rate gives reasonable accuracy for continuum scale modelling.

2.6.2. Water-gas-shift reaction

Steam enhances the conversion of carbon monoxide to carbon dioxide and hydrogen via the reaction:

$$CO+H_2O \leftrightarrow CO_2+H_2 \tag{70}$$

The reaction rate proposed by Haberman and Young [198] for the water gas shift reaction (WGSR) at around 800 °C is given by:

$$\dot{r}''' = k_{sf}\left(p_{H_2O}p_{CO} - \frac{p_{H_2}p_{CO_2}}{K_{ps}}\right) \tag{71}$$

$$k_{sf} = A\exp\left(-\frac{E_{act}}{RT}\right) \tag{72}$$

with $E_{act} = 103191\ J \cdot mol^{-1}$ and $A = 0.0171\ mol \cdot m^{-3} \cdot Pa^{-2} \cdot s^{-1}$ [198]. A modified approach is suggested in Lehnert *et al.* [192]. The WGSR is faster than the electrode reaction with carbon monoxide. The reaction rate for the WGSR is also less critical than for MSR and can occur at relatively high operating temperatures, such as 750 to 900°C, and can be assumed to be in equilibrium [140,192,198,199].

2.7. Heat transfer

Heat transfer and temperature distribution are among the most important concerns in SOC design due to the high operating temperatures. Should thermal gradients become excessive, mechanical failure will occur. Fig. 10 shows the different modes of heat transfer within the SOC. The heat equation in the gas channels involve convection and conduction with no heat generation (neglecting pressure work, radiative flux, species diffusion and viscous dissipation). For the passive electrode layers, the heat equation primarily involves heat generation caused by ohmic heating and conjugate heat transfer by conduction and convection in solid and fluid regions. The heat generation in the electrodes and electrolyte, and subsequent dissipation result in a temperature distribution within the cell that influences its performance.

For a multi-species mixture, the principle of conservation of energy may be written:

$$\rho\frac{De}{Dt} + p\frac{D}{Dt}\left(\frac{1}{\rho}\right) = \rho\frac{Dh}{Dt} - \frac{Dp}{Dt} = \mathrm{div}\left(-\dot{\mathbf{q}}''_{rad} + k\,\mathrm{grad}T - \sum_i \mathbf{j}_i h_i\right) + \dot{q}''' - \Phi \tag{73}$$

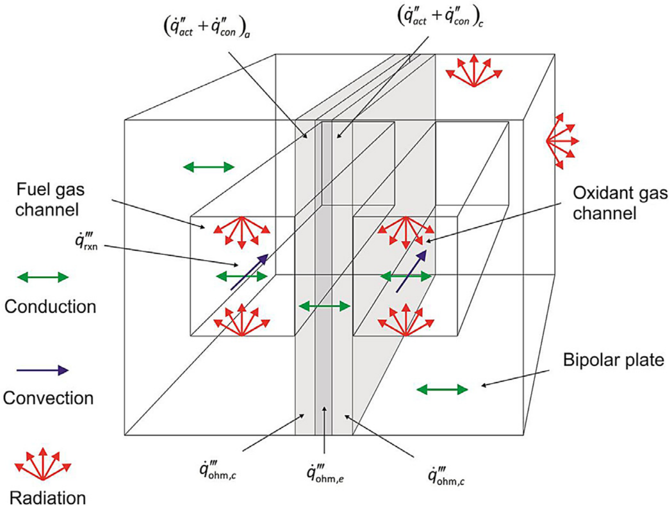

Fig. 10. Illustration of where the heat transfer processes occur.

where e is internal energy, h total enthalpy, $\mathbf{j_i} h_i$ is the product of the diffusion flux, Eq. (35), and individual species enthalpy. The terms on the right-side of Eq. (73) are, respectively, due to radiative flux, heat conduction, species diffusion, volumetric sources of heat, and viscous dissipation. In porous media, the thermal conductivity is an effective value, $k = k_{\text{eff}}$. The reader will note that mass transfer losses are often converted into concentration overpotentials, but generally one does not speak in terms of thermal or temperature overpotentials, even though heat and mass transfer are similar processes.

2.7.1. Heat sources and sinks

The heat sources, $\dot q'''$, in Eq. (73), take into account (i) Joule heating, (ii) heating due to electrochemical/chemical reactions and (iii) latent heat due to the formation of gaseous water. Depending on the model, reactions are assumed to occur at either the electrode/electrolyte interfaces (per unit area) or within the electrodes (per unit volume). The total heat generated is the difference between the enthalpy of the reaction, ΔH, and the electrical energy, as discussed in section 2.1. The total heat dissipated can be written as in Eq. (26), namely $\dot q = i(E_H - V)$, with $E^H = \Delta H/2\text{F}$. This can be prescribed as a volumetric source, $\dot q'''$, by replacing the total current i with the local current density, i'', and dividing by an appropriate electrolyte or electrode thickness.

A better method is to break down individual heat sources and apply these locally within different components. Commonly referred to; are reversible, $\dot q_{rev}$, heat sources/sinks and irreversible, $\dot q_{irr}$, heat sources, see Eq. (26). With reference to Eq. (14), the term $-T\Delta S$ is the chemical energy released/consumed in the form of heat, referred to as the reversible heating/cooling in a SOFC/SOEC.

$$\dot q_{rev} = -\frac{T\Delta S}{2\text{F}} i \tag{74}$$

In theory ΔS may be defined for a single-electrode half-cell reaction, and the entropic heat will generally be different for alternate electrodes. In practice, though, the parameterisation is challenging, e.g., the value of the molar entropy of ions. Therefore Eq. (74) is typically applied across the whole cell in its entirety. The irreversible heating is associated with losses in the cell; a fraction of the electrochemical energy is converted into heat in both fuel cells and electrolysers, $\dot q_{irr}$,

$$\dot q_{irr} = (E - V)i = \eta i \tag{75}$$

Thus the total heat generated may be re-written as $\dot q'' = (-T\Delta S/2F + \eta)i''$ for an active catalyst layer of negligible thickness. The overpotential can be broken into a number of different contributions, which all contribute to the evolution of heat, see section 2.9.

Also, the chemical (not electrochemical) reactions described in section 2.6 can generate or consume heat and can be written according to:

$$\dot q''_{\text{rxn}} = \Delta H \dot r'' \frac{1000}{\text{M}} \tag{76}$$

where ΔH is obtained from Eq. (15) for all reactants/products. For values of ΔH_0 between 600 K and 1200 K, the reaction heat (J/mol) for reversible WGSR and reversible MSR reaction can be approximated as [200,201]:

$$\Delta H = A + BT \tag{77}$$

where $A = $-206205.5 J/mol, $B = $-19.517 J/(mol·K) for MSR and $A = $-45063 J/mol, $B = $-10.28 J/(mol·K) for WGSR. Heat generated is redistributed through the electrodes, electrolyte, and interconnects by conduction, and carried away by gas and coolant streams by convection, and radiation.

2.7.2. Porous media and stacks

Considering Eq. (73), either by neglecting pressure work, radiative flux, species diffusion, volumetric sources of heat and viscous dissipation, or (better) by including them as source terms, $\dot q'''$, we obtain the equation:

$$\frac{\partial}{\partial t}(\alpha \rho c_p T) + \text{div}(\rho \mathbf{U} c_p T) = \text{div}(\alpha k \,\text{grad} T) + \alpha \dot q''' + \sum_{NB} U_v (T_{NB} - T) \tag{78}$$

The first four terms in Eq. (80) are referred to as (i) transient, (ii) convection, (iii) conduction, and (iv) source (sink) terms. Term (v) is absent in porous regions; it is employed in some stack models to account for 'interphase heat transfer' e.g., between, say, the gas channel and the electrolyte and interconnect regions. The quantity U_v is a 'volumetric heat transfer coefficient'. For convenience, only one source term, $\dot q'''$, is shown, although there will be more, as discussed above. The species diffusion terms, $\text{div}\sum_i \mathbf{j_i} h_i$, in Eq. (73) are only negligible in the event of the Lewis number being unity, Le = Pr/Sc = 1. Todd and Young [137] indicate that at 1000 K, Pr for H_2 and H_2O are approximately 0.73 and 0.86, respectively, whereas for 50% mol H_2O/H_2, Sc = 0.36, so that, depending on concentration, 0.4 ≤ Le ≤ 0.5. Under the circumstances, the species diffusion terms should therefore be included as source terms.

The velocity components are derived from the momentum equations, Eq. (29) or Eq. (30). Joule heating is due to the resistance to electron flow, Eq. (29) or (30). For the chemically-active electrodes, reversible heat sources, Eq. (74), are additionally prescribed on a volumetric or per unit area basis. For the solid electrolyte, the main terms in Eq. (80) are due to Joule heating and heat conduction. $\dot q'''$ is generated by Joule heating caused by the migration of charged ions, and by the electrochemical reactions. Both metallic and ceramic interconnectors are employed in planar solid oxide cells. The electrical resistance of the former, while small, should still be accounted for as a heating source. Indeed, a high thermal conductivity is beneficial and ensures that the interconnector redistributes heat and thereby reduces undesirable temperature gradients.

2.7.3. Thermal boundary conditions and contact resistance

For the external boundaries of the entire cell: In the fluid passages, the inlet gas conditions are generally assigned as Dirichlet conditions $T = T_{\text{in}}$ on $\partial\Omega$ (fixed value): outlet fluid values are arbitrary (no boundary value required) for situations where axial conduction is negligible. For low Pe, an outlet value is required,

$T = T_{\mathrm{out}}$ on $\partial\Omega$, which is problematic. Some solid surfaces might be treated as adiabatic, $\dot{q}'' = 0$ on $\partial\Omega$ or constant temperature. More generally, a linear-type relation $\dot{q}'' = U(T_\infty - T)$ on $\partial\Omega$. The overall heat-transfer coefficient, U, could include forced and natural convection, as well as a radiation component. Internal boundary conditions, for example at the electrode/electrolyte interfaces, are based on conservation principles:

$$k\frac{\partial T}{\partial n}\bigg|_{\mathrm{an}} - k\frac{\partial T}{\partial n}\bigg|_{\mathrm{el}} = \dot{q}'' \tag{79}$$

where $\dot{q}''$ is the surface heat generation due to the electrochemical reactions at that interface as described above; see Eqs. (74) and (75).

Thermal contact resistances also exist at the internal interfaces of SOC parts. Such resistances are difficult to assess analytically and depend on temperature, geometry, and the material properties of the contact, as well as solid stresses and strains. The contact resistance of ceramic interfaces between materials used in SOCs is discussed in Koch [202]. Not much work directly devoted to SOCs is available, however, some information can also be obtained from other engineering fields [203-205] and expressed in terms of a finite temperature jump, $\Delta T = \dot{q}''/h_c$, in series with the thermal resistances of the joined solids. The relative magnitudes of the contact conductance, h_c, and the solid conductance k/l (for a layer of thickness l) determine whether contact resistance is significant. Values of the thermal contact resistance are typically in the range of 5×10^{-6} - 5×10^{-4} m^{2}K/W:

2.7.4. Heat transfer in solid oxide stacks

A simple analysis of the thermal behaviour of an SOC can provide a first estimate of temperature distributions for 0-D or 1-D cell models. It can also be employed locally in stack-level heat transfer models [76,88,89]. In the gas channels, convective heat transfer coefficients, h, are assumed to be available or readily determined by correlations. Then, the steady flow of heat flux is given by:

$$\dot{q}'' = U(T_w - T) \tag{80}$$

where T_w is the electrode interface temperature, T is a bulk gas temperature and U is an overall heat-transfer coefficient:

$$\frac{1}{U} = \frac{1}{h} + \frac{H}{k_s^{\mathrm{eff}} s} \tag{81}$$

For unsteady heat transfer, Newton's law of cooling may be applied. Radiation can also be considered as being in parallel, $U = U_{\mathrm{con}} + U_{\mathrm{rad}}$, see Eq. (86), below. The first term on the right side of Eq. (81) is due to convection while the second is due to conduction. H is the solid thickness, k_s^{eff} the effective conductivity and s a conduction shape factor that may be measured experimentally, or obtained by means of a computer simulation [206]. The heat transfer coefficients, h, are commonly presented in a non-dimensional form as a Nusselt number, Nu, and this depends on the flow field, fluid properties and geometry [206]. Shah and London [207] correlate the Nusselt number, Nu, in rectangular and other channels. Typical formulae assume:

$$\mathrm{Nu} = \frac{hD_h}{k_f} = \mathrm{fn}(\mathrm{Re}, \mathrm{Pr}, \mathrm{geometry}) \tag{82}$$

and $\mathrm{Pr} = \mu c_p/k_f$, $\mathrm{Re} = uD_h/\nu$, k_f is thermal conductivity of the fluid, μ dynamic viscosity and c_p fluid-specific heat.

In the electrolyte/electrodes, heat transport primarily occurs by conduction and heat generation by ohmic heating caused by the electron transport, $\mathrm{div}(k\,\mathrm{grad}T) + \dot{q}''' = 0$. The reader should note that for the electrodes, the conductivity is frequently computed as a weighted average of the solid and fluid values, see Eq. (91), below.

2.7.5. Thermal radiation

The high operating temperature of SOCs suggests that radiative heat transfer may be a significant mode of energy transfer. Although water vapour and carbon dioxide occur at high concentrations in the fuel electrode, most models ignore their contributions, despite the fact that these are known to absorb, emit and scatter radiation in various wavelength bands. In most cases where thermal radiation has been considered, only surface-to-surface radiation was treated. Some models have considered radiation in the porous regions and include the absorptivity of the porous material. Damm and Fedorov [208] review some of these issues. Radiation in SOCs is one area where SOC researchers rely almost entirely on model results, as reliable experiments are non-existent.

2.7.6. Surface radiation in internal fuel cell passages

In the channels if the gases are considered to be radiatively non-participating, surface-to-surface radiation calculations may be performed for planar SOC geometries [209-215] and for tubular geometries [214,216-219]. The analyses are based on the presumption of diffuse-grey radiative exchange. The basic equation for element i may be written,

$$\dot{q}_i = \frac{\varepsilon_i}{(1-\varepsilon_i)}\left(\sigma T_i^4 - q_{0i}\right) = \sum_{j=1}^{N} F_{i-j}\left(q_{0j} - q_{0i}\right) \tag{83}$$

where $\varepsilon_i$is the emissivity of the i^{th} element, q_{o} is the radiosity (the total of emitted and reflected radiation) and $F_{i\text{-}j}$ a configuration factor [220]:

$$F_{i-j} = \frac{\cos\theta_i \cos\theta_j}{\pi s^2} dA_j \tag{84}$$

and $\sigma = 5.67 \times 10^{-8}$ W.m^{2}K^4 is the Stefan-Boltzmann constant. Following Modest [220], the unknown radiosities may be eliminated [219] to yield:

$$\dot{q}_i = \varepsilon_i\left(\sigma T_i^4 - H_{oi} - T_k^4 \sum_{j=1}^{N} F_{i-j}\sigma + \sum_{j=1}^{N} \frac{1}{(1-\varepsilon_j)} F_{i-j} q_j\right) \tag{85}$$

where H_{oi} is the external radiosity at any 'holes' in the enclosure periphery. Many authors simplify the analysis by assuming a simple planar [212,215,221] or axisymmetric exchange [215,217,218] at fixed temperature(s). Yakabe *et al.* [209] mysteriously replaced the radiosities in Eq. (85) with emissive power. The problems with Eq. (85) are: (a) the additional effort associated with the one-time computation of $F_{i\text{-}j}$, for complex geometries; (b) the extra run-time effort to update the radiative heat flux. In general, surface radiation may be spectral, and specular rather than diffuse-grey. Of course, the material properties of the porous gas diffusion layer will differ from the channel walls, and if mesh or gauze is employed in place of ribs, these will affect the problem. As the micro-channels are very narrow, only a few immediate neighbours (opposite and sides) in any given channel will be of any consequence, and the computation can then be simplified.

2.7.7. Participative radiation and radiative control

While the gas channels may be analysed by means of a surface radiation analysis, depending on property values, the electrolyte and electrodes of an SOC constitute participating media for which a radiative transfer equation [220] may be derived

Numerical solutions to the this are often conducted using discrete ordinate or Monte Carlo methods to calculate the radiant flux vector in Eq. (73). These are extremely computer-intensive procedures. Fortunately, the literature [222,223] suggest that less than 1K difference in electrolyte temperature is associated with the electrode-electrolyte assembly. Thus, it is widely maintained that for the material properties encountered in SOCs today, participative radiation is inconsequential. The electrolyte may be treated as being optically thin, while the electrodes may be considered as so optically thick as to be opaque for all practical purposes.

For optically-thin regions, a multi-flux model or Schuster-Schwarzschild approximation may be constructed. For thin-plane layers, a two-flux model may be sufficient. For optically-thick regions, a diffusion approximation is considered appropriate, with radiative conductivity defined in terms of a Rosseland mean absorption coefficient, to be added to the conduction term. An optically-thin region would be e.g., a YSZ electrolyte, whereas the Ni-YSZ and LSM electrodes may be considered as optically-thick. The presumption that the electrodes are transparent and the electrolyte opaque is based on the optical properties of the materials employed today. Should those change, a reassessment would be required. Optical properties provide a mechanism to control local stack temperature/gradients, Spinnler *et al.* [224,225]. The above analysis already adds considerably to the complexity of the calculation procedure. Even so, for situations where radiation is important; it is probably over-simplistic: In reality, the electrolyte assembly is a porous media with non-homogeneous optical properties, including dependent scattering, while the interconnect is typically metallic and hence there may be both specular and diffuse components to the surface radiosity.

2.7.8. External radiative exchange between cell stack and enclosure

Achenbach [74] noted that radiation losses from an SOC stack are significant. Numerous authors [89,213,215,216] account for this by implementing a simple radiation boundary condition at the outer stack walls, namely, $\dot{q}'' = \varepsilon\sigma F(T_\infty^4 - T_w^4)$, where T_∞ is an ambient temperature and F is a shape factor. The emissivity, ε, can be estimated, e.g., by placing a cold specimen of the steel outer casing in a pre-heated furnace and observing the transient temperature profile [220]. A radiation heat transfer coefficient may be defined according to:

$$U_{\text{rad}} = \frac{1}{T_\infty - T_w}\sigma\varepsilon F\left(T_\infty^4 - T_w^4\right) \tag{86}$$

While SOC stacks are generally field-operated in an insulated environment, they are frequently laboratory-tested in a furnace. This leads to a number of issues for the purposes of model validation and verification: (i) Both natural and forced convection heat transfer will likely be present at the sides and top of the stack, in addition to thermal radiation; (ii) irradiation of the cell/stack assembly by the guard heaters in the furnaces is seldom uniform; (iii) heat transfer by conduction through the base will be significant; (iv) the cell is made of a lamination of different materials which have different properties and the outer surfaces are rough, not smooth; (v) the surface-optical properties of SOCs will change with time, e.g., due to oxidation and possibly soot deposition (from the furnace) depending on the type of furnace employed. Peksen [68] compared a combined radiation-natural convection condition in a furnace environment to a simple adiabatic model. The furnace problem is illustrative of how experiments used for evaluation of SOCs are not suitable for validation and verification of computer models. It should be noted that SOCs are now operated at lower temperatures than in the past, so radiation heat transfer becomes less important of an issue in the future.

2.7.9. Cell and stack cooling

Cooling an SOFC stack is primarily achieved by internal heat transfer to the air. At the same time, the external boundaries of the hot stack and insulation are in contact with ambient conditions and some cooling of a stack at the external heat surfaces may need to be considered in the model, depending on the U-value of insulation employed. Cooling of a cell/stack will be a combination of internal gas convection and external conduction and radiation to the outer surfaces of the cell/stack where mixed (forced/free) convection is present. Assuming external insulation is employed, the heat transferred by external convection term will likely be small. Heat losses to the ground through the base plate may have some influence on the temperatures of lower cells in a stack. Generally speaking, the overall heat transfer coefficient, U, will vary as a function of position; however, this is usually considered constant. This may readily be evaluated by the construction of a computational heat transfer model of a stack at constant stack temperature, or a physical experiment. The combined contributions of convection and radiation may be considered as being in parallel, with arithmetic averaging employed, $U = U_{con} + U_{rad}$.

Heat transfer is a very important consideration in SOCs. Minimisation of thermal gradients and ‘hot spots’ are of paramount importance, especially for planar designs. Metallic interconnectors act as fins and can reduce thermal gradients. Cooling is generally effected by convection of the air/oxidant, though conduction and radiation within and without the cell/stack are also important. As is true, elsewhere in this review, a range of possible equations from simple rate equations to detailed integral and differential equations may be solved. Local temperatures will directly affect electrical conductivity, Nernst potential, and current density (reaction rates) and therefore thermal calculations should be carefully employed based on suitably-obtained property values. It is recommended to verify mathematical models against stacks operated in a well-insulated environment, where heat losses from the stack will be small in comparison to the fraction of heat that is convected away by the internal flow of air/oxidant (and to a lesser extent, fuel), rather than in a furnace, where it is difficult to define thermal boundary conditions.

2.8. Microstructural analysis of porous electrodes and transport layers

Effective transport properties, may be related to bulk properties [226-228]:

$$\langle k, \sigma, D\rangle^{\text{eff}} = M\langle k, \sigma, D\rangle_0 \tag{87}$$

The M-factor represents the microstructure influence. It requires evaluation for both gaseous (thermal conductivity, k, species diffusivity, D) and solid phases (ionic/electronic conductivity, σ, and thermal conductivity, k). Some solid regions (i) contain mixtures of, e.g., ceramic and metallic components; and (ii) some properties, such as, k, must be averaged between the fluid and one or more solid phases.

2.8.1. Exchange coefficients in porous multiphase electrodes

In porous media, there is an increased diffusion length and a reduced void volume due to microstructural effects. Historically, exchange coefficients (conductivities, diffusivities, and viscosities) were often corrected by tortuosity, τ, and porosity, ε. The geometric tortuosity for phase k is defined as the ratio between the mean path length L_{mean} and the shortest linear distance between two points on a representative element of volume.

$$\tau = \frac{L_{\text{mean}}}{L_{\text{min}}} \tag{88}$$

Tortuosity is always greater than or equal to 1. Note that multiple definitions of tortuosity exist; for example geodesic tortuosity, experimental tortuosity, effective tortuosity; simulated, for example, with CFD or Lattice Boltzmann Method [227,229]. A comparison between the geometric and geodesic tortuosity can be found in Stenzel *et al.* [227].

The M-factor is sometimes written as:

$$M = \frac{\varepsilon}{\tau^m} \tag{89}$$

m has been associated with a power of 1 for the straight-capillary-tube model:$M = \varepsilon/\tau$, Wyllie and Spangler [230], to describe electrical current in brine-saturated rock. This has limitations, as Epstein [150] noted. A more suitable model for gas flow in porous media may be the inclined-capillary tube model, $M = \varepsilon/\tau^2$, developed by Cornell and Katz [231], among others, from data on limestone, sandstone, and dolomites. Neither of these were developed to describe SOC electrodes. τ^2 is commonly referred to as the 'tortuosity factor'. Bruggeman [151] suggested, $\tau = 1/\sqrt{\varepsilon}$ so that $M = \varepsilon^{1.5}$, which is not valid for diffusive transport in composite SOC electrodes for low porosities. Archie [232] considered $M = \varepsilon^m$, which has also proven popular and is another specialisation of Eq. (89). Note that the influence of the microstructural *M*-factor, differs for each distinct phase, i.e., for an SOFC anode, different values are obtained for the pore, Ni and YSZ phase, respectively [226,228,233,234]. The tortuosity may also vary with direction, i.e., $\boldsymbol{\tau} = (\tau_x, \tau_y, \tau_z)$. However, reliable information regarding the direction-dependent electrode tortuosity is rare.

The formulation of Schmidt and co-workers [226,229], accounts for tortuosity, phase connectivity, constrictivity and active TPB length obtained from 3-D image analysis [226,228]. A large dataset with stochastically-generated microstructures was used in Stenzel et al. [228] to determine the *M*-factor. This yields predicted errors of less than 9% compared to 13.6% in earlier studies [228]:

$$M = a\frac{\varepsilon^b \beta^c}{\tau^d} \tag{90}$$

where β is a constriction factor, which can be physically interpreted as the ratio between the average sizes of the bottlenecks and the bulges in the pores, $(r_{\min}/r_{\max})^2$. Values of $b < 2$ are common [229]. c is typically in the range 0.6-0.7, and d around 2. *M*-factors for Ni, YSZ, and pore structures before and after redox, are discussed in Pecho *et al.* [226]. Structural parameters, such as in Eq. (89) do not have a simple geometric meaning: their calculation is a function of geometric concepts from image analysis such as median axis and shortest pathway. Thus, the introduction of a pre-exponential factor, a, can be justified [227,229].

The bulk effective thermal conductivity of heterogeneous materials can be calculated according to a series or parallel approach. For resistance in parallel, it is computed as an arithmetic average of the solid and fluid values:

$$k = k^{\text{eff}} = \varepsilon k_f + (1-\varepsilon)k_s \tag{91}$$

The thermal conductivity of the gas mixture, k_f, may be calculated, for example, by the correlation of Mason and Saxena [235]. The series and parallel approaches correspond to the lower and upper bounds (Wiener bonds) [236,237].

In porous composite electrodes, if the effective electrical conductivities for the electronic and ionic phases, Eqs. (59) and (60), can be expressed in terms of an Archie/Bruggeman type correlation, this may be modified as [238]:

$$\sigma_j^{\text{eff}} = \sigma_j\left[(1-\varepsilon)\phi_j P_j\right]^m \tag{92}$$

where ε is the gas void fraction, ϕ_j is the volume fraction of solid species j and P_j is a percolation factor (i.e., the fraction of pathways that are open not closed). A value of $m = 1.5$ - 3 is typically adopted in the literature. Of course, any of the other relationships Eqs. (89)-(89) may be likewise suitably modified. Eq. (91) and other variants were frequently employed in the past owing to a lack of better data. Accurate effective transport parameters of porous SOC electrodes, not restricted by such heuristic assumptions, can be either determined by means of direct measurements, Kornely *et al.* [239], Dierickx *et al.* [38] or by performing a numerical simulation in a 3-D digital reconstruction of the electrode, Choi *et al.* [152], Joos *et al.* [240]. In the latter approach, a potential difference $\Delta\phi$ may be applied to two opposing faces of the reconstructed geometry. The resulting current, i, can be obtained by directly solving the electronic transport equation with reference to Eqs. (61) and (62) in phase j, namely: $\mathrm{div}(\sigma_j \mathrm{grad}\phi_j) = 0$. The effective conductivity σ_j^{eff}can be calculated from the straight-line distance L between the contact layers of cross sectional area A, as:

$$\sigma_j^{\text{eff}} = \frac{i}{\Delta\phi}\cdot\frac{L}{A} \tag{93}$$

This approach is feasible for most transport processes in porous electrodes (electronic, ionic and heat conduction, as well as gas diffusion). A sufficiently high reconstruction resolution is essential to account for constriction effects at contact points between particles. This is usually not a problem for sintered structures such as SOC electrodes.

2.8.2. Structural property analysis of composite electrodes

A composite electrode is usually fabricated by sintering a mixture of electron-conducting particles and ion-conducting particles at high temperature. In the case of cermets such as Ni/zirconia or Ni/ceria (the fuel electrodes of choice nowadays in most SOCs), the metal is sintered in the oxidised state (NiO) and reduced during the start-up procedure. The electrode performance depends on its effective electronic and ionic conductivities, TPB length, and pore radius. These are functions of morphological properties, including composition, particle size and overlap, porosity, and sintering conditions, as well as intrinsic properties, e.g., conductivities. Methods for characterising the electrode morphology and effective properties typically fall into the three categories: (i) computer simulations of random packings of spherical particles; (ii) predictions by random packing-based percolation theory; and (iii) reconstructions of electrode microstructures based on tomographic methods. Electrode images show that the particles are non-spherical after sintering [241]. Nevertheless, models with random packing of spherical particles [152,242] can yield important qualitative and quantitative insight. In computer simulations, electrode structures are generated by some packing algorithm. The morphological parameters and effective properties are then evaluated against the simulated structures [189,241,243-246]. The deduced effective properties can then be used as inputs for performance model studies.

Unlike numerical simulation methods for packing generation, percolation theory is an analytical predictive method, with effective properties deduced directly from measurable input parameters, such as porosity, particle size, and composition. The development of percolation theory is helped by simulations that provide numerical validation of the analytical model. Percolation theory relies on the evaluation of coordination numbers of particles to predict effective properties. Suzuki and Oshima developed a theoretical model to estimate coordination numbers in multi-component mixtures [247,248]. The Bouvard-Lange model has been widely used to calculate coordination numbers for binary systems [249]. Costamanga *et al.* [189,243] proposed percolation models for SOFC electrodes. Chen *et al.* [250] and Chan *et al.* [246] also proposed SOFC micromodels. Janardhanan *et al.* [251] used percolation theory to predict TPB lengths. Chen *et al.* [252] also developed a percolation model that satisfies the contact-number conservation requirement. Bertei and Nicolella [132] proposed a percolation model that improves on Suzuki and Oshima's theory [247].

In a typical percolation model, the composite electrode is treated as a binary system with a random mixture of electronic-conducting electrode particles (denoted as *ed*) and ionic-conducting electrolyte particles (denoted as *el*). The average number of l-particles in contact with a *k*-particle can be estimated as [252]:

$$Z_{k,l} = 0.5\left(1 + r_k^2/r_l^2\right)\bar{Z}\frac{\psi_l/r_l}{\psi_{ed}/r_{ed} + \psi_{el}/r_{el}} \tag{94}$$

where $\bar{Z}$ is the overall average coordination number of all particles, often set to 6 for a random packing of spheres [252]. k, l=ed, el and $r_{\text{ed(el)}}$ is the average radius of the ed (el) particle. $\psi_{\text{ed(el)}}$ is the volume fraction of the ed (el) particles in the solid electrode structure.

The TPB length for a pair of contacting el and ed particles is the contact perimeter between the particles. The contact perimeter can be evaluated as $l_{k,l}=2\pi r_{\mathrm{C}}$, where r_{C} is the neck radius, which can be calculated as $r_{\mathrm{C}}=\min(r_k,r_l)\sin\theta$, and θ is the contact angle that is usually assigned a value of 15° [253]. The TPB is only effective when the contacting particles form a percolating network, the effective TPB length per unit volume can be estimated as [189,252]:

$$\lambda_{\mathrm{TPB}}^{\mathrm{eff}}=l_{\mathrm{ed,el}}n_{\mathrm{ed}}^{\mathrm{V}}Z_{\mathrm{ed,el}}P_{\mathrm{el}}P_{\mathrm{ed}}=l_{\mathrm{ed,el}}n_{\mathrm{el}}^{\mathrm{V}}Z_{\mathrm{el,ed}}P_{\mathrm{el}}P_{\mathrm{ed}} \tag{95}$$

where n_k^{V} is the number of k-particles per unit volume in the composite electrode, $n_k^{\mathrm{V}}=(1-\varepsilon)\psi_k/(4\pi r_k^3/3)$[247]. The effective TPB length estimated by Eq. (95) is found to agree well with experimental measurements [73]. The probability of k-particles belonging to the percolated network may be calculated as [132]:

$$P_k=1-\left(\frac{4.236-Z_{k,k}}{2.472}\right)^{3.7} \tag{96}$$

where $Z_{k,k}$ is the average number of k-particles in contact with a k-particle and can be estimated with Eq. (94). The average pore radius may be estimated as [252]:

$$r_g=\frac{2}{3(1-\varepsilon)}\left(\frac{1}{\psi_{\mathrm{ed}}/r_{\mathrm{ed}}+\psi_{\mathrm{el}}/r_{\mathrm{el}}}\right) \tag{97}$$

The effective electrical conductivity of the composite electrode can be calculated using a hard-sphere packing model [252,254] with $\sigma_k^{\mathrm{eff}}=M\sigma_k^0$, where σ_k^0 is the electric conductivity of material-k, e.g., using Eq. (93). The results of coordination numbers, percolation probabilities and TPB length predicted by Eqs. (94)-(96) were confirmed in Sanyal *et al.* [255]. The above analysis assumes a single particle size for each component. Generalisation of the percolation theory to that for a multi-component mixture can be found in refs. [132,252].

2.8.3. Structural properties and performance of infiltrated electrodes

In nanoparticle-infiltrated electrodes, nano-sized electronic-conducting particles, e.g., Ni, are coated on the surface of micron-sized scaffold ionic conducting particles, e.g., YSZ [256-258]. Infiltrated electrodes offer numerous advantages over co-sintered composite electrodes, as long as the nanoscaled infiltration exhibits sufficient durability. A high TPB density is obtained due to the use of small particles. The scaffold structure stabilises the mechanical properties of the fuel electrode during redox cycling and mitigates the mismatch of the thermal expansion coefficients of electrolyte and electrode. As the microstructure of an infiltrated electrode is different from that of a conventional composite electrode, dedicated theoretical analyses are necessary.

Numerical analyses were carried out, that cover electrode morphology, effective properties, electrochemical performance. Zhang *et al.* [171] proposed a 3-D kinetic Monte Carlo (KMC) model to generate morphology; porosity and tortuosity factor are calculated during KMC sintering. The KMC model was improved by considering a weighted risk factor for the aggregation of infiltrated particles [259]. A parametric study was conducted to examine the TPB density, percolation probabilities of infiltrated nanoparticles and pores, Synodis *et al.* [260], describing a mechanistic model to mimic each fabrication step. The percolation thresholds and effective conductivities were computed for varied infiltrated particle size, porosity, and pore size. The capability was extended by Reszka *et al.* [261] to include the prediction of TPB density and other morphological quantities. Bertei *et al.* [262,263] estimated TPB length, ratio of electronic to ionic conductivity, and mean pore size for electrodes with composite electronic/ionic backbone particles infiltrated in the electronic conductor phase. Bertei *et al.* [264] reported an approach to quantify the electrochemical microstructural degradation of nanostructured electrodes. Combining this with experimental 3-D tomography and EIS, the simulations provide a quantitative description of the roughness and fractural nature of the TPB in Ni-infiltrated ScSZ fuel electrodes.

Nicollet *et al.* [265] and Mortensen *et al.* [266] performed electrochemical performance and impedance modelling, which led to the determination of transport properties. Surface exchange reaction rates of $\mathrm{La_2NiO_4}$ calculated from the impedance measurements are in agreement with the literature. Bertei *et al.* [263] conducted electrochemical performance simulations with a simplified representative geometry, Tanner *et al.* [267]. Guidelines for the rational design of infiltrated electrodes were deduced. Rahmanipour *et al.* [268] proposed a distributed charge transfer model to simulate the electrochemical performance and impedance spectra of SOFCs with MIEC electrolytes and infiltrated electrodes, used to provide insight into the optimal design of materials/dimensions.

Analytical models for the analysis of infiltrated electrodes began by following the simplified geometric representation of Tanner *et al.* [267] and used a 1-D model equation derived for the activation overpotential of infiltrated electrodes [269-271]. The models are successful for air electrodes infiltrated with various electrocatalysts, however, they omit the description of the microstructure-dependent effective conductivity and active TPB length. Hardjo *et al.* [272] developed a theoretical model based on the formation of a semi-continuous infiltrate film on the surface of an electrolyte scaffold. The model was combined with numerical simulations to account for the effect of microstructures on the electrode properties. Effective electronic conductivity and TPB density were reported as a function of infiltrate particle size, scaffold particle size and porosity. A degradation model associated with infiltrate particle coarsening was also presented.

Simple analytical models that consider an infiltrated electrode as a random packing of some equivalent super-particles were developed by Chen *et al.* [258,273-275]. Each super-particle consists of a core representative of a scaffold backbone unit and a shell of infiltrated nano-particles on the core surface. Combining this with percolation theory, section 2.8.2, all effective properties of an infiltrated electrode can be determined. For example, expressions for the electronic and ionic conductivities of the packing unit as functions of nano-particle loading were derived [273,274]. The conductivities of the packing unit are combined with Eq. (93) or equivalent to yield the effective conductivities. The percolation threshold of nano-particles in the shell of the packing unit agrees with experiments [252,273]. The effective TPB density is determined by the TPB density in the packing unit and the electrode porosity. The TPB densities for both single- and binary-phase infiltrated electrodes are in excellent agreement with experimental data [258]. The hydraulic radius of the pore should not be determined by Eq. (97), but should be calculated based on the radius of the super-particle and the electrode porosity [275]. It is shown that only the super-particle radius-determined hydraulic radius can produce the experimental polarisation relation [275]. The effective TPB density, electrical conductivities and pore radius are all expressed analytically and validated by experimental data, and can be therefore used to design infiltrated electrodes [258,275].

2.8.4. Numerical reconstruction of electrode microstructures

The porous electrode structure plays an important role in SOC performance: A large TPB length is needed, and at the same time, the effective conductivity for electrons and ions and gas permeability should be as high as possible. These factors depend on microstructural properties, which are formed during the fabrication sintering process. High temperatures exceeding 1200°C are required to densify the electrolyte and even at operating temperatures of 600 to 1000°C, the sintering of porous electrode structures may continue. A straightforward approach to applying nanoscale structures exhibiting high volumetric TPB and surface area densities, respectively, is generally not feasible.

To gain a fundamental understanding of the microstructural properties, advanced experimental techniques with different spatial resolution, such as X-ray tomography [276], focused ion beam-scanning electron microscopy [241,277], and high-angle annular dark-field scanning transmission electron microscopy tomography [278] can be employed to understand the different microstructural properties; TPB length, tortuosity, and phase connectivity. Model-based generation of microstructures can provide different microstructures in a shorter timeframe. Rüger *et al.* [279] applied a geometry generator to establish simplified cube-based porous electrode microstructures for simulation studies in LSCF electrodes. Using a KMC model, Zhang *et al.* [171] found that at a typical porosity, the effective electrical conductivity is low with $M = 0.1$, Eq. (87). Reconstructing the microstructure of the fuel electrode functional layer and substrate of four different anode-supported cells, values of $0.16 \leq M \leq 0.26$ were found for the YSZ-phase effective conductivity in the fuel electrode functional layer, whereas lower values $0.08 \leq M \leq 0.12$ were found in the substrate, Joos [280]. Dierickx *et al.* [38], report a further reduction of the ionic conductivity related to Ni-interdiffusion during sintering [281]. With respect to the Ni-phase, the conductivities were even further reduced $0.02 \leq M \leq 0.08$, which is still sufficiently large as the bulk conductivity of Ni is orders of magnitude more than that of YSZ.

Losses in porous electrodes are significantly affected by the transport of ions through the ionically conducting matrix. Many state-of-the-art SOCs are fabricated with thin film electrolytes (about 10 µm), and the losses in the porous electrode, due to ion conduction, are comparable to that of the electrolyte. Extensive efforts are being made to extend the electrochemical reaction into the porous electrode, which will increase the distance for ion transport. Dierickx [38] analysed Ni/YSZ cermet electrodes experimentally, and performed simulations with a transmission line model, Euler and Nonnenmacher [282], revealed penetration depths of between 3 and 14 µm for different material and microstructural properties. In another study [283], it was found that the peak TPB length can be increased by reducing the backbone particle size.

The KMC model can predict the electrode microstructural evolution during sintering procedures. As the electrode microstructure is digitised, calculation of the TPB length, tortuosity, porosity, diffusion coefficient, connectivity, etc. is straightforward. Validation of the microstructures requires the reconstruction of a number of samples. The KMC method is computationally demanding. Moreover, it is not suitable to predict microstructure properties of electrodes fabricated using new materials, due to the lack of material data, such as the interfacial energy. Therefore a microstructure generation method based on spherical particle random packing and dilation was developed. It is simple, material property-independent and applicable to various materials, however, it is not a reconstruction of an actual microstructure. The effective conductivity of composite electrodes was studied in Zheng and Ni [284]. It was found that $M = \sigma^{\mathrm{eff}}/\sigma \leq 0.1$. However in the case of the Jülich fuel electrode functional layer, the volume fraction of 8YSZ is closer to 50% and the tortuosity around 2, resulting in $M \approx 0.25$ [38]. Additionally, the impact of the interdiffused NiO further decreases the 8YSZ bulk conductivity, [281]. These results indicate that the ohmic loss in porous electrodes due to ion transport in the electrodes is significant. Efforts are underway to extend the electrochemical reaction into the porous electrode, increasing the distance for ion transport. Increased ionic conductivity should be considered in the development of new electrode materials and microstructure arrangements.

In one study [283], a spherical particle random packing and dilation method was extended to study the properties of nanostructured SOFC electrodes fabricated by the infiltration method. In another study [259], the structural properties of dual-phase infiltrated electrodes were considered. It should also be noted that the percolation TPB length is zero at a low infiltration loading (i.e., < 6 vol.%), although the total TPB length is still high (300-400 µm/µm^3), as the nanoparticles are not well-connected to form continuous paths for electron/ion conduction. The study demonstrated the feasibility of increasing TPB length by dual-phase infiltration. However, loading must be controlled to achieve peak TPB length, high effective conductivity and gas transport permeability. Optimisation can be achieved by multiphysics simulations of reconstructed electrode structures [285].

The availability of 3-D microstructure reconstructions in the last decade provided highly accurate microstructural parameters that are applicable in cell-level models. The approach was previously limited to artificially-generated cube or sphere models. Multiphysics modelling approaches in 3-D reconstructions were initially developed by Shikazono *et al.* [286] and Shearing *et al.* [277] to model the performance of Ni/YSZ cermet fuel electrodes. Shikazono *et al.* applied a Lattice Boltzmann Method, whereas Shearing *et al.* used a FVM with individual voxels of the reconstruction as the finite volumes. The TPBs represented electrochemically-active sites with localised Butler-Volmer behaviour, using length-specific current density. In the paper by Matsuzaki *et al.* [287], a Lattice Boltzmann Method for MIEC air electrodes in which gas diffusion coupled by a Butler-Volmer-type equation was presented. In these approaches; reconstruction down-sampling was performed to reduce computational efforts. In the work of Kishimoto *et al.* [288], a sub-grid scale model was applied to keep the quality of the structural information that would be otherwise lost. Considering the large number of parameters, an unambiguous parameterisation by means of fitting is difficult, as different parameter combinations may result in the same performance. In the paper by Häffelin *et al.* [289], a 3-D FEM microstructure model of a Ni/8YSZ-cermet fuel electrode was fully parameterised by measured data. With this approach, a good agreement with measured ASR values was obtained. Another possibility to prove the validity of a 3-D microstructure model is to simulate the AC impedance over a wide frequency range. Häffelin *et al.* [290] present a time-dependent impedance model of mixed-conducting air electrodes and compare it to a homogenised approach based on Gerischer impedance, as discussed in Adler *et al.* [291]. Such a microstructural model provides valuable information about the impact of material and microstructural properties on the impedance of mixed-conducting air electrodes.

2.9. Overpotentials

The concept of ‘overpotential’ was introduced in Eq. (6). Current is produced/consumed when there is a change in the difference in electrochemical potentials between the two electrodes or phases within an electrode. The term contains multiple meanings throughout the literature, but essentially represents irreversible enthalpic losses that either require additional energy to overcome (SOEC) or decrease the amount of usable work from the systems (SOFC). For any given electrode k;

$$\eta_{\mathrm{act},k} = \phi_{el,k} - \phi_{io,k} - E^{\mathrm{ref}} \tag{98}$$

i.e., $\eta_{\mathrm{act},a}$, $\eta_{\mathrm{act},f}$ for the air and fuel side respectively. The reference value, E^{ref}, is with respect to a given reference condition electrode, usually taken as a standard hydrogen electrode, but which could also account for local concentrations effects on thermodynamic potential, as given e.g., in Eqs. (17) and (18). In addition to activation losses, the term ‘overpotential’ is an accepted designation for losses due to a number of causes; concentration gradient

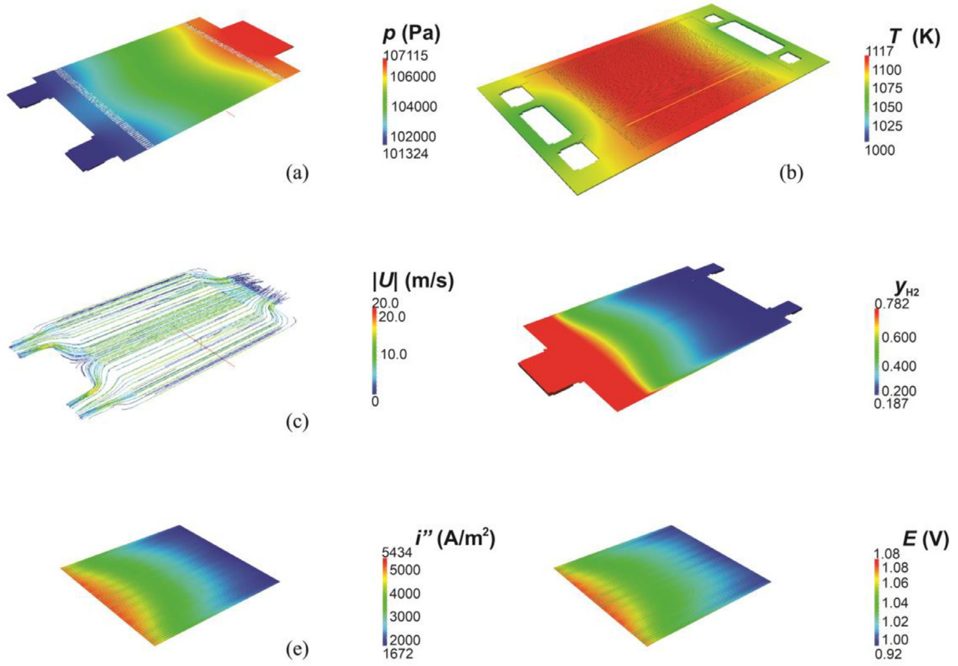

Fig. 11. Results from performance calculations for the Jülich Mark F solid oxide fuel cell showing (a) air-side pressure, (b) plate temperature, (c) stream-lines, (d) hydrogen mass fraction, (e) local current density, (f) Nernst potential. From [124].

and ohmic losses, e.g.,

$$\eta = \eta_{\mathrm{ohm,\ el}} + \eta_{\mathrm{ohm},f} + \eta_{\mathrm{ohm},a} + \eta_{\mathrm{ohm,int}} + \eta_{\mathrm{act},a} + \eta_{\mathrm{act},f} + \eta_{\mathrm{con},a} + \eta_{\mathrm{con},f} \qquad (99)$$

This helps deconvolute the contributions to the cell potential, however the overpotentials are not entirely separable due to their interconnectivity. For a detailed 3-D model, the concept is not particularly useful, though it does provide one way to visualise losses on a common scale, as shown for a 1 cm^2 SOC in Fig. 4(b). The nature of the three main overpotentials are discussed below.

The activation and concentration overpotentials, and Nernst potential are functions of partial pressure of reactants/products and temperature and thus are local values as depicted in Fig. 11. These, in turn affect the local current density distribution, see for example the hydrogen, Nernst potential, and current density distributions in Fig. 11(d-f).

2.9.1. Activation overpotential

The activation overpotentials, η_{act} are associated with overcoming the reaction energy barriers at the TPB or reactive surfaces (the so-called double charge layers). If the concentrations at the TPB are considered within the equilibrium expression, then the activation overpotential is known as a surface overpotential; i.e., directly influencing the reaction rate across the interface. The electrochemical kinetic equations used, e.g., the Butler-Volmer, Eq. (64), establishes a relationship between the current density and the activation overpotential in each electrode.

When multiple fuels are employed, the total current density in the fuel electrode is the result of the individual current densities associated with the reaction of the different fuel species, for example, $i'' = i''_{\mathrm{H}_2} + i''_{\mathrm{CO}}$, where the electrolyte potentials that drive the reactions are the same for each phase, i.e., $\Delta\phi = E_{\mathrm{CO}} - \eta_{\mathrm{CO}} = E_{\mathrm{H}_2} - \eta_{\mathrm{H}_2}$at the fuel electrode; this adds complexity to the solution algorithm. This approach is to be considered a starting point, the actual situation is somewhat more complex as discussed in Bao *et al*. [99].

2.9.2. Concentration overpotential

The concentration overpotential stems from changes in the local concentrations at the reaction site from those assumed at the reference, either standard conditions or those in the channel. The concentration overpotential manifests itself through the concentration dependences of both the kinetic equations Eq. (67), and thermodynamic losses, Eq. (21). Mathematically, these losses are calculated using a mass or mole transport model, e.g., Eqs. (40)-(41). Thus, one can evaluate the concentration overpotential by assuming no reactant transport losses within the electrodes (i.e., conditions are the same at the reaction site as in the channel). However, this generates a somewhat arbitrary definition when mass-transport phenomena are modelled in detail, and thus, while useful for interpretation, should not be included in Eq. (99). Typically, due to the nature of the coupling of mass transport and kinetics and the equilibrium potential, the concentration overpotentials have signatures that are more exponential than linear with current density (see right-side Fig. 4(a)).

For simple 0-D and 1-D models that do not explicitly account for detailed mass transport (e.g., along-the-flow models), modified Nernst equations can be used to account for the expected concentration overpotentials or simple linear transport always can be used as closure expressions [178,292,293]. At the electrode TPB, the partial pressure may be written as a simple algebraic function of the partial pressure in the gas channel and current density,$p_{i,\mathrm{TPB}} = f(p_{i,\mathrm{gc}}, i'')$. The derivation involves writing the 1-D molar balance $\mathbf{J}_i = p_{i,TPB}(u_i - u*)/\mathrm{R}T$and substituting Eq. (41) for the molar conductance according to equivalent film-theory, i.e., $g_i* = D_i^{\mathrm{eff}}/h$, The effective diffusivities, D_i^{eff}, are obtained from Eqs. (43) and (56), and h is electrode thickness. The assumption of equimolar counter diffusion, $\dot{N}_i = J_i$, commonly found in several references is not correct; a flowing current always implies moles are being transferred at the electrodes. The methodology for the computation of concentration overpotentials described here is based on the simplest possible of all the various analyses provided in section 2.3. The molar fluxes of the individual species are computed as $\dot{N}''_j = \nu_j i''/z\mathrm{F}$, as in Table 1. The paper by Beale [144] contains a discussion of

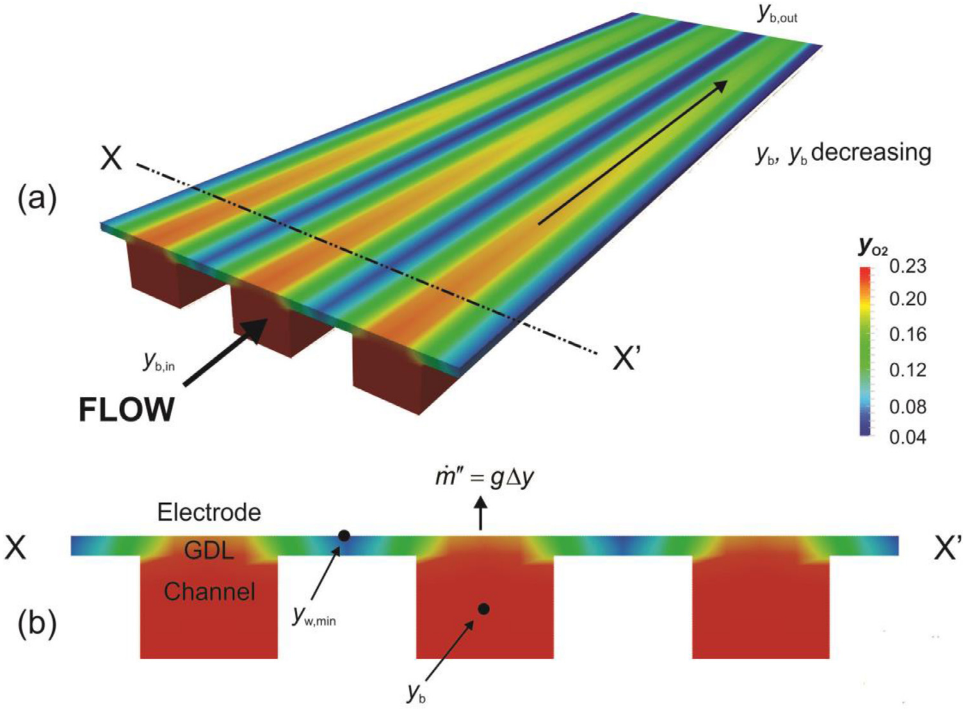

Fig. 12. Local oxygen distribution in a SOFC. Reproduced from Beale *et al.* [295].

the subject. The above discussion was presented in terms of partial pressure, p_i, though any number of alternative dependent variables, c_i, x_i, y_i etc. could be employed.

In a 3-D fuel cell or electrolyser, where ribs are employed, Fig. 12 shows that mass-transfer limitations will occur across-the-flow at the electrode surface located near the ribs/lands. This phenomenon is shown in the papers by Geisler *et al.* [294] and Beale *et al.* [295]. The local current density can go from a maximum to a very small value over a short distance, as local starvation of oxidant or fuel occurs. Under the circumstances, the validity of employing a concentration overpotential in 2-D/3-D is called into question: One can always calculate a 2-D or 3-D concentration overpotential, for display purposes as noted in Andersson *et al.* [62]. The concentration overpotentials are then a function of the ratio of the partial pressures of fuel species at the location of interest to that in the channel. This clearly depends on the choice of location in the channel.

2.9.3. Ohmic overpotential

The ohmic overpotential represents the resistance to getting the ions/electrons to/from the TPB sites, which is a loss of available free energy (SOFC) or that which must be overcome (SOEC). This can be accounted-for by simply introducing an equivalent resistance for ionic or electronic charge transfer which relates to the difference in the ionic or electronic potentials in the Kirchhoff-Ohm, Eq. (6), or Ohm's law, Eqs. (59)-(60). For example, the difference in the ionic potential which for a single-ion conductor and typical definitions is the O^{2-} electrochemical potential between the air electrode TPB and fuel electrode TPB. Similarly, the electronic potential including possible contact resistances can be calculated.

The ohmic overpotential, η_{ohm}, is related to the ohmic resistance $R_{\mathrm{ohm}}(T)$, that is composed of terms in the air and fuel electrodes, electrolyte, interconnects, and additional layers in the cell.

$$\eta_{\mathrm{ohm}} = i'' \cdot \sum_k R_k = i'' \cdot R_{\mathrm{ohm}} \tag{100}$$

The ohmic losses are usually dominated by the electrolyte (but see section 2.8.4). Much smaller electronic losses occur in the interconnectors (at least for metallic components) and electrodes. It should be noted that the ohmic resistance is typically linear, but may not be if the conductivity changes, locally. Also, it is tacitly assumed in calculating an ohmic overpotential that the local current density may be presumed to be locally 1-D throughout the electrode-electrolyte assembly. An Arrhenius equation is usually sufficient to model these losses over a wide temperature range:

$$R_{\mathrm{ohm}}(T) = \frac{T}{B_{\mathrm{ohm}}} \exp\left(\frac{E_{\mathrm{act}}}{RT}\right) \tag{101}$$

Values of B_{ohm} and E_{act} for the materials used in the Jülich cell [35,178] are given in Table 2. For uniform geometry $R_{ohm} \propto 1/\sigma$, and the reader will also encounter inverse expressions of the form,$\sigma = (B_{\mathrm{ohm}}/T)\exp(-E_{\mathrm{act}}/\mathrm{R}T)$, to be used in Eqs. (61) (62). Other expressions, e.g. power-series, may be used to fit the decrease in R_{ohm} with increasing temperature.

While these overpotentials can be used in simplified cell and stack models, where computational speed is a priority, then less information is obtained about e.g., the activation overpotential distribution as in the two potential models described in section 2.4. In the same manner the concentrations of the gas species are only indirectly described through the respective assumed concentration profile through the thickness of the electrodes. The corresponding approach for achieving the resistance from the gas diffusion is simply by describing the gas-transport by the respective PDE, see Section 2.3.

The approach in section 2.3 and section 2.4 as in [136] and the one described in this section with serially connected resistances/overpotentials are thus two alternatives. Depending on the investigations, the different phenomena can be either described as a 0-D overpotential or through a PDE in section 2.3 and section 2.4.

2.10. Code implementation

There are many combinations of the above system of equations which may be used to construct mathematical models of SOCs. Since one goal of the present article is that it be tutorial in nature, with an emphasis on explanation and guidance to the non-expert; two practical implementations are listed here as guidelines.

Either: (i) The Kirchhoff-Ohm relation, Eq. (6), and the Nernst equation, Eq. (17), together with one or two suitable expressions for the activation terms, for instance Eq. (64), constitute a system of coupled equations for E, i'', $\eta_{\mathrm{act},f}$, $\eta_{\mathrm{act},a}$.

or: (ii) The two half-Nernst equations, Eqs. (24) (25) are solved for E_a and E_f along with the Poisson system, Eqs. (59) and (60), for the ionic and electronic potentials with Eq. (64) and $i'''_k = ai''_k$ for the ionic and electronic current densities per unit volume.

In both (i) and (ii), the Nernst potential and activation overpotential are evaluated as a function of temperature, pressure, and composition. Sources/sinks of mass, heat, and momentum are computed, as described above. In both cases (i) and (ii) the following additional steps are taken

(1) The continuity, Eq. (27), momentum, Eq. (29)/(30), energy, Eq. (73), and species equations, Eq. (35) are solved and used to compute pressures, temperatures, and concentrations, see Fig. 8.
(2) Bulk properties are enumerated at current temperature, pressure and concentration levels from which effective property values are enumerated.
(3) The process is repeated until a satisfactory measure of convergence is obtained.

The local resistance/conductivity is obtained from correlations of the form Eq. (101). Typical values of parameters such as the reaction orders, γ, the pre-exponential terms, i_0^{pre}, the symmetry coefficients, β, and the geometric factors, M, as well as B_{ohm} and E_{act}, needed for the Ohmic losses in Eq. (6), Leonide et al. [35,178] are shown in Table 2. The methods used to obtain these values are described, below, in section 3. For alternative geometries/components, the user must carefully obtain values of these and other parameters experimentally.

In ref [124], a mesh is defined as a region upon which a particular set of differential equations is solved. Fig. 13 illustrates the regions upon which the various transport equations are employed when the Kirchhoff-Ohm approach is adopted: The energy equation is solved on the entire cell, whereas momentum equations are solved only in fluid regions, and electrochemistry in electrode and electrolyte regions. For a full two potential model, a different domain decomposition strategy would be employed with the electronic potential being solved for in the electrodes and interconnectors and the ionic potential in the electrodes and electrolyte, see Zhang *et al.* [296] for details.

Fig. 11 shows sample calculations from the former implementation, based on Eqs. (6), (17), and (64), with hydrogen as fuel and dry air as oxidant for a 1-cell insulated stack, for a Jülich Mark F design, Fig. 3, as described in the paper by Beale *et al.* [124]. Fig. 11(a) shows air-side pressure, whereas Fig. 11(b) displays temperature. It can be seen, for counter flow, the temperature is a maximum in the central region of the cell and that the temperature gradient is significant, a matter for concern in SOC design due to stresses along the periphery of the cell and at the glass-metal seals. Fig. 11(c) exhibits air-side streamlines coloured by velocity magnitude. The flow is generally uniform other than in the manifold regions. Fig. 11(d) shows hydrogen mass fraction which does not decrease at the sides of the cell due to there being an electrochemically inactive region there. Fig. 11(e)(f) show the local current density and Nernst potential in the electrochemically active region of the cell. A comparison of the results of methods (i) and (ii) for a high temperature polymer electrolyte fuel cell may be found in the recent paper by Zhang *et al.* [296]

The results of Fig. 11 were obtained by coding original source code within an existing open source library OpenFOAM [297], which employs equation mimicking. The advantages of employing open source codes are: (a) The user has complete control of the model equations employed. (b) He/she does not have to write the CFD solvers, they already exist. (c) The models may be shared freely with others, who do not have to pay expensive license fees. (d) Similarly, high performance computers employing numerous ranks may be deployed. Both open source and commercial software may also be linked [298] to chemistry software such as Cantera [65,66] should a higher order kinetic scheme be considered necessary.

2.11. Stack and multiscale modelling

Solid oxide cells are generally operated in stacks, and the performance will vary from cell-to-cell. While it is theoretically possible to solve the systems of equations described above; a very large number of computational cells will be required to tessellate the region occupied by a stack, including manifolds [299,300]. The solution of Beale and Zhubrin [76] is a volume-averaging or ‘homogenising’ technique. This means that the details of the individual parts, Fig. 3, are lost. Rate equations are substituted for the prescription of drag and heat transfer. Within the ‘core’ of the stack (channels, electrodes and electrolyte, interconnects) the energy and momentum equations in the form of Eqs. (81) and (30) are solved, with:

$$F = \frac{2f\mu \mathrm{Re}}{\varepsilon D_h^2} \tag{102}$$

$$VU_v = AU \tag{103}$$

in place of Eqs. (31) and (80). In Eqs. (102) and (103) f is a friction coefficient and U_v is a volumetric heat transfer coefficient obtained from U, as given by Eq. (81) thereby eliminating cross-wise diffusion terms in the channels. Values of f and U may be obtained by physical experiment, analytical and/or numerical solutions e.g., of Sturm Liouville differential equations, or by conducting detailed CFD calculations in a repeating unit. Stream-wise diffusion is still permitted, so low Reynolds/Péclet flows are properly considered. In the manifolds, the standard momentum, Eq. (29), and energy, Eq. (73), equations are solved, in detail. With the addition of mass transfer, Eq. (40), the Kirchhoff-Ohm relationship, Eq. (6), and Nernst equation, Eq. (17), a stack model is created. Volume-averaged results were compared to a detailed simulation with near-identical results, with a significant (100 ×) increase in computational speed, and decrease in required memory. Nishida *et al.* [301] developed and applied the method [89] to a Jülich Mark-F 18-cell stack for which experimental data had been gathered [302]. Stack modelling in fuel cells is the subject in the recent article by Beale *et al.* [303].

Further developments in stack modelling include the work of Molla *et al.* and Navasa *et al.* [304,305] who modified the charge transport equation so the computational volumes are able to contain multiple SOC cells. Mechanical stresses/strains are also considered. Steady state simulations of a full stack in 3-D can be simulated in the range of minutes (10-15 minutes) on a workstation [16]. The geometry in this type of homogenised model is indirectly included through effective material parameters such as the overall resistance, Eq. (102) and volumetric heat transfer coefficient in Eq. (103) for the stack. The submodel of a repeating unit can also be used to obtain local parameters, such as overpotentials, or stress

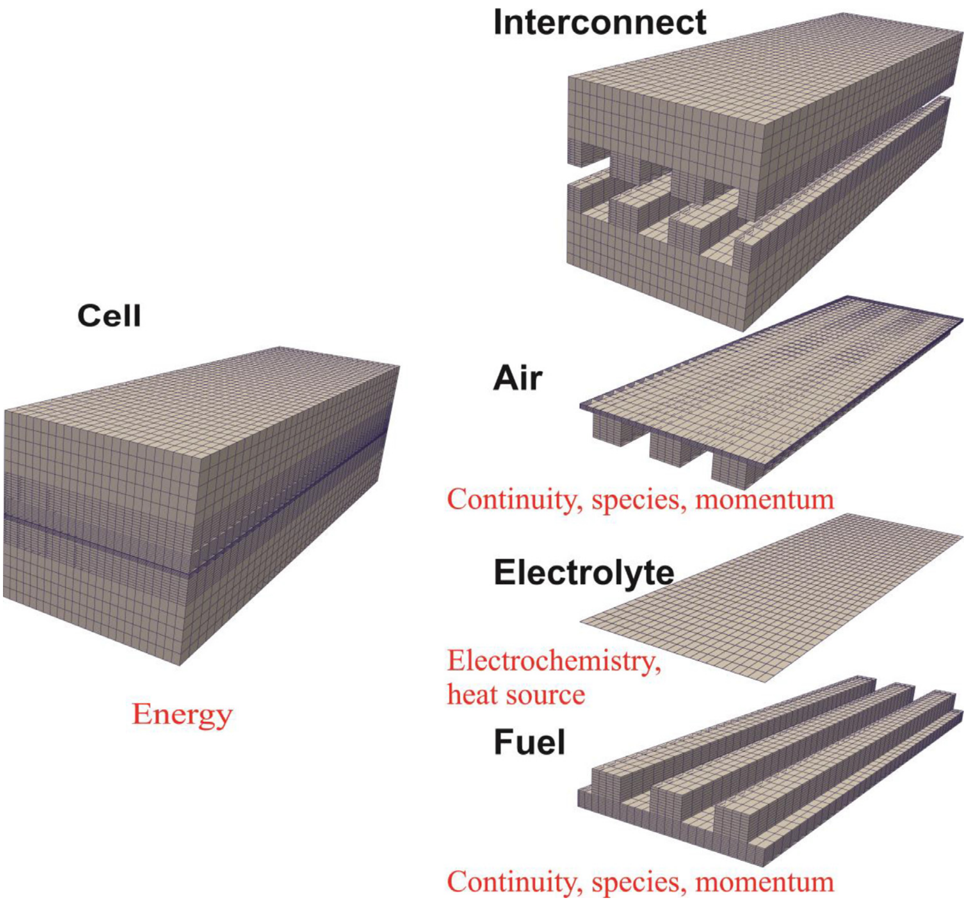

Fig. 13. Example of domain decomposition strategy. Reproduced from Beale *et al.* [124].

concentrations [16]. The homogenised stack model and the submodel of the repeating unit constitute a multi-scale model, which can be run with limited computational resources, e.g., on high-end computer workstations, obviating the need for supercomputers.

Computational capacity is continuously increasing and with this the opportunity for running more extensive simulations, such as full stack models based on the single-cell formulations described in this paper. However, except for a very few published works [299,306] this has not been utilised to-date in the SOC modelling community.

While massively parallel computational resources could help push the boundaries for what is possible in computational engineering of electrochemical cells; SOC technology also requires practical modelling tools to develop prototypes of new stack designs and predict long-term performance, realistically. For this, multiscale modelling approaches based on employing the results of fine-scale calculations within a coarse-scale approach are accessible. Such models can readily be run on high-end computer workstations and are both reliable and efficient.

It is recommended that in the future, not only should efforts be taken towards harnessing the resources of high-performance super-computers to obtain detailed numerical solutions, but also in the meantime, computationally efficient multiscale models should be further developed and further refined.

2.12. Degradation and durability modelling

Understanding and controlling SOC degradation mechanisms are among the greatest challenges for the maturation of the technology. Degradation is the comprehensive term used for performance deterioration over time due to intrinsic property variations (conductivities etc.), microstructural changes (TPB lengths, porosity etc.), poisoning effects, and macroscopic failures, for example delamination, contact loss, electrolyte cracking, that are the result of operation. These are difficult to predict deterministically, even if specific external phenomena, such as chromium/sulphur poisoning, carbon deposition, gas formation and pressurization, can be identified as causes of degradation. Mechanistic correlations are difficult in the cases of microstructural, contacting, and catalytic wear of active components resulting from seemingly safe operation.

Different research groups have looked into modelling the various degradation processes occurring in SOCs. These include chromium-poisoning of the air electrode, corrosion scale forming on the air side of the interconnect, nickel agglomeration and nickel migration. Whereas some works focus on characterising and modelling one phenomenon at a time, e.g., corrosion [307], chromium poisoning [308,309], and Ni-agglomeration [310]; others attempt to integrate all of them in a single 1-D or 2-D model [311-317]. Simulating transient degradation in 3-D for a full stack has not yet been accomplished.

The interrelation of all processes taking place in SOCs at all scales would render any numerical extrapolation of these dependences, over the long term, completely unfeasible in terms of calculation resources. Simplified modelling approaches need to be employed, compatible with useful lifetime predictions. This relies on statistical methodologies for mapping and correlation of parameters (among others Bayesian inference, the method of moments and maximum likelihood estimation procedures), and on the development of approximation models which mimic the behaviour of a deterministic model. The input-output behaviour is solely important. In the case of stochastic degradation mechanisms, these can be modelled by certain random mathematical processes, such as the Gaussian process, random walk, (non-homogeneous) Poisson point processes, or gamma processes.

It follows that the model must rely on data generated by the tested system, to capture significant behavioural correlations over the complete operational space. The surrogate model can only emulate those parts of the SOC that are confined by the location of experimental measurement. This means the influence of any peripherals inside the cell (such as cell frames, or stack manifolds, or similar) must be carefully considered. If properly carried out, this approach provides a way, not only to predict the global behaviour of the system, but also to provide validation of complex, deterministic models. The approach is very sensitive to the quality and quantity of initial experimental data.

Yan *et al*. [318] developed a 2-D dynamic model for heat and mass transfer coupled with electron and ion transport equations, adopting a simplified approach based on ordinary differential equations to model catalyst activity and anodic porosity time evolution. The dependence of the variables on operating conditions was accounted-for through synthetic parameters extracted by the model. Regarding the estimation of SOFC cell/stack remaining useful life (RUL); Wu and Ye [319] proposed an algorithm combining diagnostic and prognostic functionalities. Voltage is used as a performance reference to estimate RUL under fuel-electrode poisoning and air-electrode humidification. The combination of a least-squares support vector machine, supervised-learning methods, and hidden semi-Markov models allows estimation of RUL within a ±20% error margin.

Some useful approaches to predict RUL, *in operando*, can be derived from statistical literature focusing on reliability assessment, though this is rarely adopted. In Guida *et al*. [320], a Bayesian estimation procedure for a degradation process modelled as a non-homogeneous gamma process is proposed, and the RUL probability density functions computed efficiently. The approach in Guida *et al*. [321] correlated degradation mechanisms, affected variables and operating conditions in a fault-tree analysis to enhance the results of statistical analysis highlighting which variable is predominant. It provides a reference computational framework yielding a better interpretation of the root-cause analysis of the occurring degradation phenomena.

Although some chemical degradation processes (Ni oxidation, carbon deposition, sulfur poisoning) can be included in continuum-scale models, see [322-324], the degradation of the SOC cells are, in many cases, at a scale smaller than continuum mechanical models can handle. Effects like poisoning of reactive sites, taking place on a molecular/atomic level, will impact macroscale parameters such as polarisation resistance or exchange current density in the model. The same holds for degradation phenomena occurring on the micro-scale such as Ni agglomeration, Ni migration, corrosion, propagation of cracks etc. These can be addressed by phase field modelling approaches. In this type of model, the numerical codes (CFD, FEM) are overlaid with an energy criterion and rate equations for changes to the microstructure. There have been a few attempts to simulate microstructural changes and the resulting performance loss by phase-field approaches [325-327]. In ref [328], the authors studied the agglomeration and migration of Ni in an SOEC. This can thus be used to describe the evolution of the microstructure and the impact on the performance of the solid oxide cells and adjoining materials.

In some cases, it is possible to represent the degradation phenomena going on at a lower scale (than modelled) by employing a number of simplifications, e.g., carbon deposition in CO_2 electrolysis [135], or corrosion of a metallic supported SOFC [276]. However although multi-scale modelling approaches including degradation, are currently under development, these must become a clear objective for the SOC modelling research community: In order to truly predict the lifetime of SOC products, performance variations in the stack as a function of degradation processes must be correctly described.

3. Experimental appraisal of modelling parameters

3.1. Input parameters and calibration

The modelling equations for a SOC include a number of parameters which require prescription. Usually geometric parameters are readily available. The same holds for some intrinsic material properties, which are available in established reference and table books, as empirical correlations and online data bases [329]. Accurate values of transport parameters such as conductivities and diffusion coefficients are critical, and have a significant impact on the results. An example is the interdiffusion of nickel into an 8YSZ-electrolyte, which affects conductivity [330,331] over time. For nominally identical materials, published values of intrinsic material property parameters can vary by one to two orders of magnitude [332,333]. The same holds for electrochemical parameters such as surface exchange coefficients of MIEC-air electrode materials [334] and line specific resistance at the nickel/YSZ/pore TPB [335], which may be affected by segregated impurities [336-338]. Furthermore, ageing phenomena [339] alter material properties over time [340,341] and therefore influence published values. The choice of model parameters and/or the lack of knowledge of their behaviour over time presents a major problem in assessing the fidelity of SOC modelling results. Furthermore, the bulk material properties have to be transformed into effective parameters considering microstructural features as volume fraction, tortuosity, volume specific surface/interface area, TPB length, etc., which may not be known. Such effective parameters are required in all cell and stack models employing volume-averaging, or ‘homogenised’, techniques.

Often, certain material parameters, for example the ionic resistivity of the electrolyte substrate or e.g., the internal resistance of the cell dominate. Therefore, values which properly reflect the system under investigation have to be selected from the literature, or better, measured in-house. In cell models, the parameter may be varied within the range of published values and this presented as a result interval [342,343]. Parameters of little significance can be fixed. The relevant parameters should either be measured directly, or, if this is impossible, a fitting procedure should be applied to adjust the simulation result to measured values, hopefully by simultaneously fitting various sets of data under different conditions. Such a sensitivity analysis may not always be practical, in view of the number of parameters.

The ASR can be determined from a polarisation curve of a small-scale (1 cm^2) cell operated at homogeneous conditions [239], so there should not be any gradients of temperature, gas composition, or current density over the active cell area. The contact resistance between cell and interconnect can be included by contacting the single cell with interconnects or by measuring an ideally contacted cell and the contact resistance in a separate experiment. A technique to increase the measurement sensitivity of intrinsic electrode catalytic properties, especially related to TPB length such as charge transfer and overpotential, is the use of patterned film electrodes of the material to be examined, where length-to-surface (and length-to-volume) ratio of the electrode material is maximised, in order to minimise bulk factors which are difficult to control experimentally, including the geometry, microstructure, and transport properties of the electrode as well as its physical and chemical compatibility with the electrolyte. The patterned electrode functions as the working electrode deposited on a regular cell substrate and can provide insights in tailored structuring of electrode materials as well as yield values for intrinsic parameters [344-347]. The measurements have to be performed in the relevant range of stack operating conditions, providing measured values as a function of temperature, fuel and oxidant composition, and current density.

For more detailed modelling, impedance spectroscopy is the reliable method to deconvolute the different mechanisms. Leonide *et al.* [126] applied impedance spectroscopy and the distribution of relaxation times [33,34] to set up and parameterise an equivalent circuit model for a SOC. A non-linear 0-D DC polarisation model coupling oxygen reduction, hydrogen electro-oxidation, gas diffusion, and ohmic losses was derived to simulate current-voltage characteristics [178] under different circumstances, based on Butler-Volmer and Fickś law with excellent agreement with measured data [22]. In the case of high performance SOCs, deconvolution is only possible if (i) the cell is operated homogeneously without any lateral gradients and (ii) an appropriate series of spectra highlighting the considered loss mechanism are measured. The testing conditions should not be fixed to a narrow, system-relevant testing parameter field but to exaggerate and thereby identify and enable the deconvolution of the different loss mechanisms in the cell. There are different approaches to access required parameters such as testing at much lower temperatures to access, for example, bulk and grain boundary conductivity of the electrolyte [348-351], and above nominal operating temperature to reduce the impact of thermally activated loss processes. Furthermore, gas mixtures can be selected that uncover loss mechanisms, such as air electrode electrochemistry [352] or gas diffusion [239].

The data presented in Table 2 include electrochemical parameters of electrodes and cells [35,36,353], microstructural parameters of porous electrode structures [240,354], and material interface parameters evaluated on model samples such as bulk ceramics and patterned electrodes. To model large area cells in 3-D, the coupling of gas phase transport, electrochemical reactions and ionic as well as electronic conduction in a porous, multiphase electrode has to be simplified. There are a number of electrochemical models [342,355-361] predicting the polarisation diagram of SOCs. These models commonly consider physical backgrounds, such as the Butler-Volmer equation, Eq. (64), and Fick's law, Eq. (38), but the equations are often simplified. The Butler-Volmer equation may be replaced by an ASR, linear function Eq. (66), or a Tafel equation Eq. (65) [359,360]. The partial pressure-dependencies of the exchange current densities are often simplified/neglected, i.e., $\gamma = 1$ in Eq. (67) [342,357,362], or a constant value is used for the exchange current density, i''_0 [356,360]. Frequently parameters are used that are either generally estimated, or taken from literature [253,363,364]. Leonide *et al.* [178] present a 0-D cell model for fuel electrode supported SOFCs, fully parameterised by means of impedance spectroscopy and an appropriate equivalent circuit model, Fickian gas diffusion in the electrodes, Butler-Volmer kinetics, with the ohmic resistance in the electrolyte being predominant. A similar approach and data values may readily be employed in 3-D models [124,365]. In [35,353], methods to deduce the model parameters from a series of impedance measurements with appropriate operating parameter variations are discussed and appropriate model equations are given. The concept is represented, schematically, in Fig. 6(b).

To model the current voltage behaviour, the voltage losses in the substrate, electrodes, and electrolyte are subtracted from the open circuit voltage as detailed in Eqs. (99) and (6). A number of parameters are required. These may be obtained by means of impedance spectroscopy measurements on single cells. Details on the procedure are to be found in [36,126,353]. Measurements are performed on small scale cells without any gradients in temperature, gas composition or current density.

The effective diffusion coefficient $D_k^{\text{eff}} = M \cdot D_k$ of gas species k is given by Eq. (87) where the parameter M is notionally written according to Eq. (89) and the structural parameters of the fuel electrode and air electrode can either be evaluated from impedance spectra [126] or calculated using the microstructural parameters, porosity, ε, and tortuosity, τ. The applicability of the model has been presented in a number of papers. Klotz applied the underlying equivalent circuit model to simulate the impedance of a stack in a 1-D approach [366]. In [22], Njodzefon proved the applicability of the model in electrolyser mode. Furthermore, the model can be integrated in FEM and FVM codes that analyse the impact of the flow field geometry [127,367] and predict local gas composition and electrochemical performance of hydrocarbon fuelled stacks [368,369]. In such approaches, the diffusive and convective gas transport in the fuel electrode substrate and the air electrode are modelled considering the cell and stack geometry. In volume-averaged or homogenised models, gas transport and catalysis are treated in a spatially resolved way, considering porosity, tortuosity and active catalyst surface evaluated by means of tomography.

3.1.1. Validation

A model without validation is of little use. The most common measure, by far, is the polarisation curve (section 1.2.1, Fig. 4). This is clearly inadequate. The development of a proper set of independent procedures, both to validate and to reliably calibrate models, is a long-term goal of the current authors, among others. It is part of an ongoing mandate of the IEA Advanced Fuel Cells Technology Collaboration Programme Modelling Annex, Annex 37, of which all of the present authors are members. The challenges are significant; SOCs are tested under extreme operating conditions, typically at elevated temperatures, often with far-from-ideal boundary conditions. Validation of the results of complex cell and stack models is an extremely important task. Most CFD models, when based on a reasonable equation set, will generate results that are qualitatively correct, and of great utility to the end user who is thus able to 'look into' the design. The step to quantitively correct results is fraught with difficulties. A model validation with published experimental data is mostly insufficient as the number of measured published parameters for SOCs is limited. In many cases, just the cell or stack performance data and some information about cell/stack design and operating parameters is available. Internal values such as local temperature distribution or local gas compositions are often missing. The 1996 International Energy Agency (IEA) SOFC benchmark [23], with hydrogen (benchmark #1) methane (benchmark #2) as a fuel has been reproduced by a number of workers [24,370-373]. It is not, however, a piece of real hardware/operating conditions, but rather a set of idealised model parameters and geometry. It is also very old. While there is no reason not to compare numerical models with other numerical models, more modern benchmarks, based on physical hardware are required. The provision of open source data bases of reliable experimental data would then allow for round robin comparisons of the results of numerical procedures to be made. Such benchmarks must be 'neutral' in nature and not steered towards any given methodology/code.

First and foremost, it is necessary, to separate out validation data from calibration data. For instance, an ASR approach, where the resistance, R, is obtained from the i''-V characteristic is very likely to show good agreement with experiments under similar operating conditions. In many cases the measured polarisation curves are approximately straight lines. Validation of a model by means of the polarisation curves should therefore include, as a minimum, varying the operating temperature, see Eq. (101), and also if possible the fuel (%H_2) and air (%O_2) gas composition, and utilisations (via the gas velocities), Eq. (1), over a reasonably wide range. In other words, one has to take care that the tests are performed over a wide range of operating parameters. Similar issues occur, for example, when activation parameters such as i''_0 in Eq. (64) are evaluated from the polarisation curves in the lim $i \rightarrow 0$.

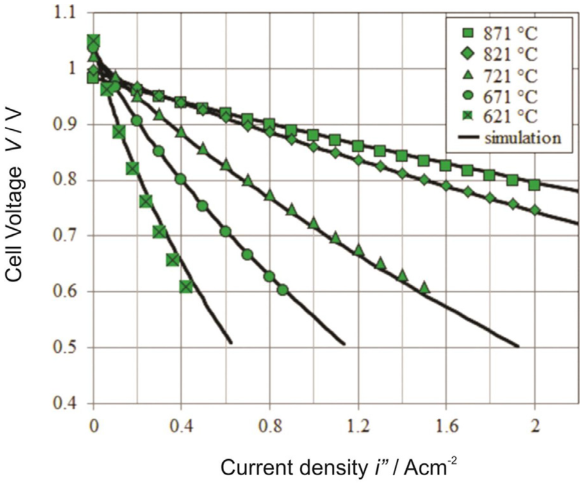

Fig. 14. Numerical and experimental polarisation curves. From Geisler *et al.* [294], with permission.

Fig. 14 shows a comparison between experimental and numerical results in terms of a polarisation curve at various operating temperatures. The authors also compared results for a variety of oxygen and hydrogen inlet concentrations. If possible, different geometries (size, flow configuration, active area, etc.) should also be considered and compared. Fig. 15 shows a comparison between experimentally and numerically obtained results gas composition in terms of mole fractions of a model reformate.

Many difficulties associated with SOC validation are, in fact, experimental quality-control issues. Normally only a single Nernst potential, corresponding to open circuit, with no internal heat sources/sinks, is measured. Conversely, solutions of Eq. (17) and (24), (25) admit to 2-D and 3-D fields of values, which are evaluated under finite current densities, see Fig. 11. Physical experiments typically employ a digital controller which ramps up and down through a program of values of current density or cell voltage, and possibly (though not always) adjusting the flow rates beyond a certain minimum current density threshold, to obtain predefined values of fuel and air utilisation: For this reason, a minimum dwell-time at any given operating point is needed, and in addition, the cell temperatures also change, due to the variation in heat sources/sinks with current density, see Eq. (26). In view of the large amount of data required for a polarisation curve; experimental results are seldom gathered under true steady-state conditions, which may under circumstances lead to damage to the specimen due to overheating. The requirement for the mathematical model to replicate transient conditions corresponding to an actual controller cycle might seem excessive, but may ultimately be necessary. Cell and stack tests are frequently conducted with cells irradiated with thermal radiation laterally in a furnace, and sitting under compression from above on a solid base, such as an uninsulated floor. Such complex thermal boundary conditions are almost impossible to replicate in numerical implementations, and they will affect the results. Ideally tests would be conducted under adiabatic (well-insulated) wall boundary conditions, and flow Reynolds numbers sufficiently high that heat metering is of high accuracy.

Two quantities of great utility for model validation are (i) local values of current density, obtained using a current scan shunt and (ii) a field of local temperatures. The former (i) would appear to be extremely difficult to obtain with the present technology, due to the high operating temperatures of SOCs, a notable exception being the work of Bessler *at al.* [374]. The resolution of current scan shunts is presently far coarser than the meshes associated with numerical simulations. Moreover it is the fine details of the electrochemical conversion process that are desired when performing cell calculations. Regarding (ii), temperature measurements are typically obtained inside SOCs by inserting thermocouples near the surface boundaries rather than in the centre of the cell, a situation which is little better than the situation (i) for current density. A deficiency for model validation is cell degradation, discussed in section 2.12; until degradation issues are addressed/resolved, modelling is limited in its range of application to performance under idealised conditions. While it is difficult to propose a 'standard procedure' for SOC model validation at this time, such an exercise (or exercises) would be of great utility, and would allow for round robin tests, of both computer codes and of experimental facilities, to be conducted.

If possible, operating parameters affecting a single loss mechanism should be selected, for example: high fuel utilisation enhancing gas conversion/depletion, diluted gases enhancing gas diffusion, lowered temperatures enhancing thermally activated losses etc. Then, one has to consider model stability limits [295] as well as inhomogeneities [375]. An uneven fuel distribution between the layers in a stack in combination with a high (average) fuel utilisation might even re-oxidise an undersupplied layer and thus change its properties irreversibly.

It is of great value if internal parameters of the cell/stack are accessible for model validation. In the case of stack testing, the most commonly measured values are the individual cell voltages. There have been some attempts to acquire in plane localised values, such as measuring the temperature distribution in a stack [376], the local fuel composition and temperature in a cell [54] or the current density distribution in segmented cells [374,377]. Different loss contributions in a SRU are accessible by means of a local potential measurement using potential probes [239]. Continuous advances are being brought about in test rig adaptation. Even different loss contributions in a SRU are accessible by means of a local potential measurement using potential probes [239].

Any numerical study should present results showing computational grid/mesh independence and convergence criteria within some minimum residual bound. Numerical convergence may be considered to have been achieved when the utilisation computed by Eqs. (1) and (3) yield identical values, to within a margin-of-error. Typically, overall values of current density, temperature, and species mass/mole fraction will change marginally as the mesh is refined. However, local extrema will change, and these are important, see for example Fig. 12. Therefore rather than recording the usual local spot values of variables, such as current density, mole fraction etc., as a function of mesh size, rather defining a ϕ-distribution by,

$$f_k(\phi) = \frac{N(\phi_k, \phi_{k+\delta k})}{\sum N} \tag{104}$$

where $f(\phi)$ represents the frequency of values located in the interval $\phi_k \le \phi \le \phi_k + \Delta\phi$ and $\phi = T,\ y,\ i''$ etc. No change in the shape (mean, variance, skewness, etc.) of f_k vs ϕ_k, as the computational mesh is refined, is indicative that mesh independent results have been attained. Modern post-pressing software can readily integrate a field of results, and generate the frequency distribution defined in Eq. (104) through a surface or volume region.

3.1.2. Verification

Analytical solutions for electrochemical processes are few and far between. A notable exception is to found in the book by Kulikovsky [133]. Analytical solutions may be adopted for code verification, as opposed to validation for which physical data are required. The 1-D solution of Kulikovsky *et al.* [378] was originally developed for an idealised polymer electrolyte fuel cell, however it may also be applied to an idealised SOC where it assumed that the fuel electrode is sufficiently fast that it may be neglected and in addition the cathodic overpotential may be taken constant. Mass

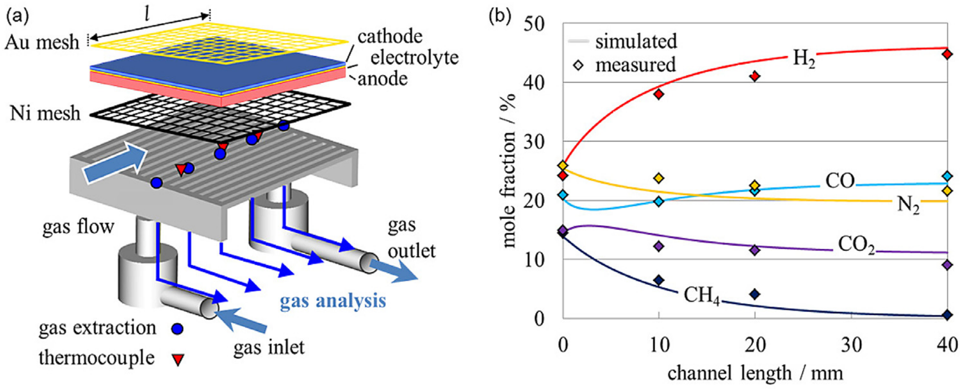

Fig. 15. (a) Single cell housing enabling localised measurements of temperatures and gas compositions; (b) gas conversion of a model reformate along the anode gas channel, measured and simulated values. From Geisler *et al.* [368].

transfer is presumed to be a passive process, so mass flux at the electrode leads to no changes in mixture density, ρ and velocity, u is constant. This implies no overall continuity change, which is clearly not true in the air electrode of a SOFC except for very small utilisation, $\varepsilon_u \to 0$. Furthermore, mixing is presumed to be 'perfect'. Let the oxygen reaction order be such that

$$i'' = \left(\frac{c}{c_{\mathrm{ref}}}\right)^{\gamma} f(\eta) \tag{105}$$

where $f(\eta)$ is the air electrode activation overpotential, which is assumed constant, and c is the concentration of, say, oxygen. It is assumed that $\gamma = \gamma_{\mathrm{O_2}}$, i.e., $\gamma_{\mathrm{H_2O}} = 0$. The concentration is related to the current density according to; $dc/dx = -i''/2Fuh$ and it can readily be shown that,

$$\frac{c}{c_i} = \begin{cases} \left(1-(1-\varepsilon_u)^{1-\gamma}\right)^{x/L} & \gamma \neq 1 \\ (1-\varepsilon_u)^{x/L} & \gamma = 1 \end{cases} \tag{106}$$

where $c_i = c(0)$, and ε_u is (oxygen) utilisation,

$$\frac{i''(x)}{\bar{i}''} = \begin{cases} \frac{1}{\varepsilon_u}\left\{1-\left(1-(1-\varepsilon_u)^{1-\gamma}\left(\frac{x}{L}\right)\right)^{\frac{1}{1-\gamma}}\right\} & \gamma \neq 1 \\ \frac{1}{\varepsilon_u}[\ln(1-\varepsilon_u)](1-\varepsilon_u)^{x/L} & \gamma = 1 \end{cases} \tag{107}$$

where $\bar{i}''$ is the mean current density. Eqs. (106) and (107) suggest that the normalised concentration and current density are a function only of $\gamma_{\mathrm{O_2}}$, and ε_u, which will not be true at high mass transfer rates. Eqs. (106) and (107) may be used as verification for computer codes. In practice it may not be possible to impose all the assumptions, above, precisely. Nonetheless, such analytical expressions are useful not only as a 'reality check' during code debugging, but also serve to give the user 'a feel' for the problem at-hand. It is of course possible to introduce additional complexity into the problem, for example by supposing that, say, $i'' = (c_{\mathrm{H_2O}}/c_{\mathrm{ref,H_2O}})^{\gamma_{\mathrm{H_2O}}}(c_{\mathrm{O_2}}/c_{\mathrm{ref,O_2}})^{\gamma_{\mathrm{O_2}}} f(\eta)$. However, this adds substantial complexity, and does not significantly increase confidence in the verification process.

3.2. Microstructure

3.2.1. Measurements of porosity

The open porosity of an electrode can be measured using porosimetry methods [379] or approximated through microscope image analysis. When analysing the fuel electrode of an SOC, it needs to be in its reduced (operating) state, hence the sample, usually delivered in its oxidised state needs to be reduced under nominal conditions, and subsequently cooled down to ambient conditions with a controlled temperature ramp (e.g., 2°C/min). The cell can then be broken into samples by mechanical means and these can be used for porosity analysis. To assess the porosity of the fuel electrode by means of Archimedean porosimetry, the air electrode and the electrolyte need to be polished and the resulting sample needs to be cleaned with distilled water and kept in a dry oven overnight at 120°C. The sample can then be cooled down in dry air to room temperature and then weighed. Following this, the sample needs to be put in a beaker with distilled water, and heated up to 100°C to displace air from the pores. After cooling to room temperature, the sample has to be weighed submerged in distilled water at 25°C. A final measurement is made by drying the outermost part of the sample leaving its structure completely saturated with water. The porosity is obtained as $\varepsilon = (m_{sat} - m_{dry})/(m_{sat} - m_{wet})$, where m_{sat} is the weight of the sample after drying its external surface, m_{dry} is the weight under dry conditions and m_{wet} is the weight when completely immersed in distilled water.

3.3. Electrochemistry

3.3.1. Reaction order

One way to evaluate the reaction order(s), γ, is to use data from EIS and equivalent circuit modelling as explained by Leonide [353]. Following Boigues-Muñoz *et al.* [380], a first-order approximation of the Butler-Volmer equation, Eq. (64), can be made with negligible error in the case of very small overpotentials, near the open circuit voltage. Such an approximation produces a linear relationship between the activation overpotential and the current density, namely: $\eta_{\mathrm{act}} \approx \mathrm{R}Ti''/z\mathrm{F}i_0''$. It should be noted that the local exchange transfer current density is dependent on the current density generated (SOFC) or consumed (SOEC) through the mole fraction of the reactants and products, hence theoretically the gas-diffusion equation should also be solved. However, because the calculations are made at low current densities, the concentrations can be assumed to be those of the bulk gas. The resistance associated with the activation overpotential can then be expressed in the following terms:

$$\left.\frac{d\eta_{\mathrm{act}}}{di''}\right|_{i''\to 0} = r_{\mathrm{act}} = \frac{\mathrm{R}T}{z\mathrm{F}i''{}_0} \tag{108}$$

By substituting the appropriate exchange current density expression, for instance Eq. (67) into Eq. (108) and applying common logarithms to both sides of the equation, the following expression for the fuel electrode is obtained:

$$\log(r_{\mathrm{act}}) = \log\left(\frac{\mathrm{R}T}{2\mathrm{F}i_{0,\mathrm{H_2}}^{\mathrm{pre}}\, exp\left(-\frac{E_{a,\mathrm{H_2}}}{\mathrm{R}T}\right)}\right) - \gamma_{\mathrm{H_2O}} \cdot \log(x_{\mathrm{H_2O}}) - \gamma_{\mathrm{H}} \cdot \log(x_{\mathrm{H_2}}) \tag{109}$$

Eq. (109) correlates the activation resistance to the reactant mole fractions. This has the form of a straight line on a log-log

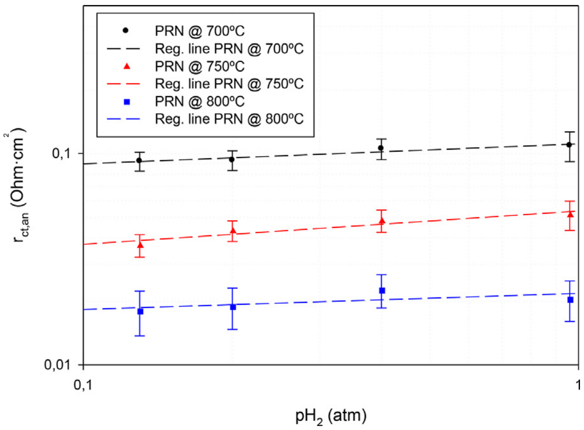

Fig. 16. Charge transfer resistance in the fuel electrode of an SOFC as a function of hydrogen partial pressure at 800, 750 and 700°C.

scale with the slope the reaction order when, H_2 or H_2O, are varied *caeteris paribus*. The charge transfer resistance of each electrode can be deduced from an equivalent circuit after deconvolution of EIS spectra and characterisation of relaxation times for each process, as described in section 1.2.2. By carrying out EIS in OCV under different compositions of H_2 and H_2O, and measuring the obtained charge transfer resistance, the values can be plotted in a log-log graph, Fig. 16 and from the gradient of the linear relationship, the reaction orders are obtained.

3.3.2. Exchange current density pre-exponential factor and activation energy

Analogously, the pre-exponential factor, i_0^{pre}, and the activation energy, E_{act}, can be obtained by applying natural logarithms to Eq. (67):

$$\ln\left(\frac{r_{\mathrm{act}}}{T}\right) = \ln\left(\frac{\mathrm{R}}{2\mathrm{F}i_0^{pre} x_{\mathrm{O}_2}{}^{\gamma_{\mathrm{O}_2}}}\right) + \frac{E_{\mathrm{act}}}{\mathrm{RT}} \tag{110}$$

The pre-exponential factor, i_0^{pre}, can be obtained from the intercept of the resulting graph as a function of 1/T, and the activation energy, $\mathrm{E}_{\mathrm{act}}$. can be obtained from the slope.

3.3.3. Forward reaction symmetry factor

The resistances associated with the charge transfer mechanisms in SOC electrodes are inherently correlated with the current being generated (SOFC) or consumed (SOEC) by means of the Butler-Volmer equation or equivalent. The methodology presented in this work is based on a two-stage data fitting approach. The first step relies on the use of an equivalent-circuit model on impedance data obtained under different current densities so as to characterise the resistance in the fuel and air electrodes. The integration of the charge transfer resistance with respect to the current density yields the mathematical manifestation of the activation overpotential as a function of the current density.

$$\eta_{act,k} = \int r_{ct,k} di'' + a_1 \tag{111}$$

where $\eta_{act,k}$ is the activation overpotential of electrode k, $r_{ct,k}$ is the charge transfer resistance associated with electrode k, and a_1 is a constant of integration.

Experimental values of the charge transfer resistance can be fitted by means of a function in a defined range, for instance a polynomial, in which the current density is the variable term. The Dirichlet boundary condition for Eq. (111) is that under open circuit voltage the activation overpotential is zero. Hence the constant of integration can be evaluated.

The second stage of the methodology foresees to fit with the Butler-Volmer equation the points generated from the activation overpotential function. As the forward reaction symmetry factor, β_f, is the only unknown in Eq. (64), it can be easily obtained by iteration methods. At low current densities, local exchange transfer current densities can be considered to be constant, hence fitting with the Butler-Volmer equation in this region will yield a more precise value of forward reaction symmetry factor.

3.3.4. Charge transport

The resistance associated with ion or electron transport can be measured either *ex-situ* or *in-situ* and is typically accomplished using EIS with an AC perturbation so that concentration gradients do not develop [381]. For multiple components, one can use the high-frequency resistance or intercept of the impedance spectra with the real axis on a Nyquist plot. This value results in a shorting of the cell, so all contact resistances and those associated with the dominant conductive pathways will be measured. To delineate between different components or interfaces, one can assemble different types of configurations, e.g., by removing the separator or changing the material thickness and measuring the overall resistance. While this technique is powerful, as it can interrogate the system under different operating conditions, it cannot distinguish the separate contributions when mixed electronic/ionic conductors are present in the same layer (e.g., electrodes) since the least resistance pathway will be measured. To determine the ionic and electronic resistance in those parts, more complicated impedance analysis such as sheet-resistance techniques are required.

3.4. Degradation measurements

In most SOC modelling approaches, the model represents the cell or stack at a fixed state. Usually, all electrochemical measurements for model parameterisation and validation are performed within a short period of time after commissioning. The same holds for material parameters evaluated by means of samples, i.e., bulk conductivities, porosities, etc. Thus, the model will represent the initial performance of the stack. This performance deteriorates with operation, due to degradation of cell materials, morphology, and chemical composition. Some approaches to degradation phenomena in SOC-models were described in section 2.12, the most advanced approach of which is a complex model that considers aging of the different electrochemical and catalytic reactions as well as diffusive and migrative transport mechanisms.

In any case, it is required to parameterise the degradation processes included in the model. In the case of space-resolved cell or stack models, one has to consider gradients in temperature, fuel and oxidant composition, and current density. As most degradation processes are affected by those parameters, the degradation is nonhomogeneous and has to be treated in a spatially resolved manner also. Thus, it is necessary to obtain information about individual degradation processes of air electrode, electrolyte, fuel electrode, contact layers, coatings, interconnects, etc., and their dependences on operating parameters. The intrinsic degradation of ionic and electronic conductivities as well as contact resistances can be measured on model samples under relevant temperature and gas composition ranges. If the conductivity decrease is caused by an interdiffused species, either from a neighbouring layer, or from impurities in the supplied gases, the measurement has to be performed under realistic conditions, i.e., in a small sized cell or repeat unit. Endler *et al.* [352,382] deconvoluted the different degradation mechanisms in a fuel electrode-supported cell by means of impedance spectroscopy and the distribution of relaxation times. A similar approach was applied to study chromium [383,384] and sulphur poisoning [385,386]. Ploner [387] studied the impact of operating parameters on the degradation of anode supported cells with a special emphasis on the aging of the Ni/YSZ cermet fuel electrode. Data were analysed and compared to evaluate the impact of temperature, fuel composition, fuel utilisation and current load. It is critical to extrapolate degradation rates evaluated during the first 1000 to 2000 hours of operation because the degradation levels off after time. In [388], the analysis of the difference of impedance spectra [389] was applied to study the degradation of SOECs. Approaches that enable deconvolution of different degradation mechanisms are essential to obtain parameters for a degradation model. The degradation is measured at fixed operating conditions without lateral gradients, which would result in an inhomogeneous degradation. Large-area cells or stacks, exhibiting extensive gradients in temperature and gas composition, should not be used to resolve individual degradation mechanisms, although they are still useful to parameterise 0-D models without spatial resolution.

Overall, the most common measurement of degradation is by measuring the i''-V relation, e.g., the development of the cell voltage under a constant current [390]. This is clear and simple for a description of the overall cell degradation over time. However, it does not reveal the origins of the degradation. The impedance spectrum is another commonly used measurement of degradation and can provide more in-depth information [391]. Both the i''-V curve and impedance spectrum are usually used to measure the degradation of the whole fuel cell and are the only known methods that can be applied *operando*. Different measurements are used to characterise the degradations of individual cell components, and these generally require post-operation characterisation.

The degradation of interconnectors usually comes from the oxidation of interconnect material, which can be measured by the increase of resistance and the weight gain. The area-specific resistance is usually measured by a 4 probe DC technique [392]. The measured resistance and weight gain are used to deduce the parameters concerning the interconnect oxide scale growth [393]. The degradation mechanisms of the SOFC fuel electrode include different phenomena such as micro-structural alteration, coking, poisoning by fuel impurities, and redox-cycling. These are accompanied by a change of microstructure of the fuel electrode that can be measured by SEM imaging [394]. Through analysis of SEM images of the composite fuel electrode at different times, the changes in the particle sizes of Ni and YSZ, and the porosity and pore sizes of the fuel electrode can be obtained. The TPB length may be deduced from the microstructure data obtained by the SEM image [395]. The change in the fuel electrode conductivity is usually measured by a 4-probe DC technique.

Degradation of the electrolyte originates from the decline of ionic conductivity of electrolyte materials such as YSZ. The ionic conductivity can be measured by a 4 probe DC technique, while the impedance spectrum can be used to identify the contribution of the bulk and grain boundary resistivity on the degradation of the electrolyte [396,397]. TEM and SEM have also been used to measure the microstructure change of YSZ [398]. Degradation mechanisms of the air electrode include interfacial chemical reactions, microstructure change, and chromium poisoning. The chemical reactions between air electrode materials and electrolyte materials will happen during the sintering process and cell operation at high temperatures [399]. X-ray diffraction is often used to identify the reaction product. X-ray photoelectron spectroscopy is also used to measure the Sr segregation on the surface of the LSM/BSCF [400]. Microstructural changes of the air electrode can be measured by SEM imaging [401,402]. The change of the particle size of LSM/LSCF and YSZ, the porosity of air electrode and the pore sizes can be obtained through analysis of SEM images. Chromium poisoning affects the electrochemical activity and the stability of air electrode and impedance spectroscopy is often used to measure the influence of poisoning [403].

4. Conclusion and recommendations

In this review the governing equations for modelling SOCs on the continuum scale have been presented, with recommendations for their use, together with an outline for future research needed on the topic.

The objectives of an SOC model include the desire to understand and predict operational behaviour, and degradation, in order to lead in the direction of continuous improvement of the technology. With enhanced predictability of SOCs and stacks, safe operation strategies can be devised, and better designs made. This will enhance product lifetime, and increase the competitiveness of the technology. This work focused on simulations at the cell and stack level, while also bridging towards microstructural scale and experimental approaches, for a more precise prediction of the effective material parameters used at the cell and stack scales.

Thus this work covers the modelling of SOCs at multiple length scales, and as found in this paper it is clear that an enormous effort has already gone into multiphysics model development. It is also clear that various approaches for simplifying the governing partial differential equations have been successfully applied to minimise computational load. But as discussed, the authors also note that there is a need to provide a stronger focus on multiscale models, which can bind together the phenomena occurring at the different length scales into a single model. This can be done either by using computational clusters, or so-called homogenisation and localisation, to combine the models at the different length scales.

Various efforts for modelling the microstructure of the porous electrodes were thus described. Likewise, advanced experimental methods, using impedance spectroscopy and relaxation times, were covered. Both can provide a better understanding of the effective cell/stack parameters. The authors find that while there are relatively few works that combine advanced experimental techniques and microstructural scale models, there is much to be learned by doing so. For multi-species mass and heat transfer in porous media, there still appear to be many different models, with no consensus on which is the needed level of complexity. This is needs to be addressed by the community.

There is no single set of formula for developing a good mathematical model of a SOC; a range of possibilities exist for the description of heat and mass transfer, electric field potentials, overpotentials, and current density. These range from simple rate equations combined with an ASR based on lumped parameters, to complex transient 3-D two potential models, involving a breakdown of all salient physicochemical processes in a detailed manner. In this paper we have outlined the different routes and discussed the limitations and advantages. While many modern CFD and other codes contain well-developed mathematics, which are amenable to relatively comprehensive models by previous standards, the modeller will still be posed with the challenge to strike a balance between described detail and computational speed and memory, to obtain the desired result.

To predict lifetime performance of SOCs, this paper also covers various work on degradation. While some simple physical relationships can be used to describe certain degradation phenomena at the continuum scale; others occur at a submicron level, making the bridging of length scales more challenging, or (at this stage) impossible. Thus, advanced characterisation of SOCs over their lifetime is essential to predict the lifetime of a stack with the cells operating at various conditions through the stack. The stochastic nature of these processes and the length of time required to make statistically significant tests are formidable challenges for the empirical communities of scientists. Some works have covered this area, but the immense experimental effort needed for this has limited model development. As the technologies mature, systematic characterisation must be undertaken to a greater extent and degradation must be put in the frame of a stack with various operating points inside. Ideally, degradation should be modelled transiently for a full stack, such that time dependent interactions between different parts of the stack are described.

Due to the high operating temperatures of SOCs, ceramics are extensively used in the current stacks with the potential for brittle failure of cells and interfaces. In this work we have also reviewed various works on mechanical modelling of failure in the SOC stacks. Detailed models for fracture in interfaces, creep of components and statistical analysis of cell failure have been presented in the literature, but not in an integrated manner and not for a full stack, due to the computational load. This, again, sets a target for the SOC modelling community: A full stack model including both time dependent mechanical behaviour and the impact on the chance of failure of the various components.

Public data bases, containing effective property values suitable for solid oxide materials, are not commonly encountered. Obtained data should be shared openly for researchers to work-with, jointly. There is a need for further developing standardised experimental techniques/results, which precisely mimic the constraints of models; for instance employing highly-insulated full-sized cells, under steady-state conditions, as well as miniature button cells. Similarly, it is recommended that the research community work towards establishing an open dataset of reliable test data from stack experiments and relevant stack design which is publicly available. The data should contain as much interior information as possible, e.g., from thermal probes during operation.

Originally, scientists wrote simple codes in source languages such as FORTRAN and C [23,74]. Subsequently general purpose commercial CFD codes were modified, both by code developers and end users, in user-defined functions and subroutines. The code vendors often worked in tandem with industry and academia to improve the functionality. In the last 10 years, open source codes have been used increasingly as the basis for the development of modern SOC models. The object-oriented paradigm allows for overloading of models; for instance different diffusion or kinetics models can be implemented in different SOC parts at run time. This facilitates comparison of sub-component models. Moreover, open source code libraries can be freely shared in international collaborations, and the license model is favourable to high performance computing installations. For example, the CFD code OpenFOAM was used as a basis for the development of the openFuelCell code [124,297]. Cantera [65,66] is another example of an object-oriented code that can be applied to electrochemical applications. This trend is likely to continue in the future and is to be encouraged. The IEA Advanced Fuel Cells Technology Collaboration Programme, Annex 37, was specifically set up to allow for the discussion and comparison of open source codes in electrochemical applications.

While much progress has been made over the last 3 decades, the science and engineering both of SOC modelling, and experimental parameterisation, and visualisation are still young and vital. Mathematical/computer models are a fact-of-life in modern engineering practice, not only for improving existing products, but increasingly-so for those under development. With patient and careful development of validated models, the disruptive changes to the barriers required to allow this important technological innovation to achieve market penetration, can be overcome.

It is hard to predict the future of SOC technology; Transportation applications for SOFCs will most likely be confined to constant operation uses, for example in the shipping industry. Probably, in the immediate future, the widest application for SOC technology is going to be SOECs, as the need for water electrolysis expands, and SOECs are currently more efficient than other (alkaline and polymer electrolyte) electrolysers, when integrated with downstream processes. Micro co-generation systems may also have a role, but at the present time are too expensive. A position paper describing the state of SOC technology was published by the IEA [404]. Other reports [20,405,406] are concerned with the techno-economic concerns related to solid-oxide and other fuel cell and electrolyser technologies and the barriers to market penetration facing the business, the main concerns being reliability and cost. If and when these can be addressed, the technology will be able to contribute to sustainable energy in a significant way.

Declaration of Competing Interest

The authors declare that they have no known competing financial interests or personal relationships that could have appeared to influence the work reported in this paper.

Acknowledgements

This work was made possible by discussion between members of Annex 37 of the Advanced Fuel Cells Technology Collaboration Programme part of the Technology Platform of the IEA. Annex 37 focuses on the design, development, and application of suites of open source computational fluid dynamics software for application to fuel cells, electrolysers, and other electrochemical applications. A number of individuals have also made useful comments on the text of this article. These include (in alphabetical order) L. Blum, Q. Fang, L.G.J. de Haart, W. Lehnert, R.T. Nishida, R. Peters, J.G. Pharoah, and S. Zhang. This research did not receive any specific grant from funding agencies in the public, commercial, or not-for-profit sectors.

References

[1] Karakasidis T, Charitidis C. Multiscale modeling in nanomaterials science. *Mater Sci Eng C-Biomimetic Supramol Syst* 2007;**27**(5-8):1082–9.
[2] Schichlein H, Feuerstein M, Müller A, Weber A, Krügel A, Ivers-Tiffée E. ystem identification: a new modelling approach for SOFC single cells. *ECS Proc Vol* 1999;**1999**:1069–77.
[3] Levich VG. Physicochemical Hydrodynamics. Engelwood Cliffs. NJ: Prentice-Hall; 1962. p. 372–94.
[4] Levins R. The strategy of model building in population biology. *American Scientist* 1966;**54**(4):421–31.
[5] Levins R. Evolution in changing environments; some theoretical explorations, ix. Princeton, N.J.: Princeton University Press; 1968. p. 120.
[6] Blomen L, Mugerwa M. Fuel cell systems: Springer Science & Business Media; 2013.
[7] Baur E, Preis H. Über Brennstoff-Ketten mit Festleitern. *Zeitschrift für Elektrochemie und angewandte physikalische Chemie* 1937;**43**(9):727–32.
[8] Yamamoto O. Solid oxide fuel cells: fundamental aspects and prospects. *Electrochimica Acta* 2000;**45**(15):2423–35.
[9] Irvine J, Connor P. *Solid oxide fuels cells: Facts and figures*. Springer; 2013.
[10] Dönitz W, Erdle E. High-temperature electrolysis of water vapor—status of development and perspectives for application. *Int J Hydro Energy* 1985;**10**(5):291–5.
[11] Laguna-Bercero M. Recent advances in high temperature electrolysis using solid oxide fuel cells: A review. *J Pow Sour* 2012;**203**:4–16.
[12] Frandsen HL, Ramos T, Faes A, Pihlatie M, Brodersen K. Optimization of the strength of SOFC anode supports. *J Eur Ceram Soc* 2012;**32**(5):1041–52.
[13] Howe KS, Thompson GJ, Kendall K. Micro-tubular solid oxide fuel cells and stacks. *J Pow Sour* 2011;**196**(4):1677–86.
[14] Traversa E. Toward the miniaturization of solid oxide fuel cells. *Electrochem Soc Interface* 2009;**18**(3):49.
[15] Beale SB, Dong W. Advanced Modelling of Fuel Cells: Phase II Heat and Mass Transfer with Electrochemistry. Ottawa: National Research Council of Canada; January 2002. Technical Report no. PET-1515-02S.
[16] Molla TT, Kwok K, Frandsen HL. Modeling the Mechanical Integrity of Generic Solid Oxide Cell Stack Designs Exposed to Long-term Operation. *Fuel Cells* 2019;**19**(1):96–109.
[17] Beale SB, Ginolin A, Jerome R, Perry M, Ghosh D. Use of Computational Fluid Dynamics and Virtual Reality for Design of Fuel Cell Stacks. Proceedings of the 8th Conference of the CFD Society of Canada - CFD2K; 2000; Montreal.
[18] Noponen M, Hallanoro P, Göös J, Õunpuu E. Status of Elcogen unit cell and stack development Proceedings of the 12th European Fuel Cell Forum 2016; Lucerne, Switzerland.
[19] Bertoldi M, Bucheli O, Ravagnia AV. High-efficiency cogenerators from SOLIDpower SpA 12th European Fuel Cell Forum 2016; Lucerne, Switzerland.

[20] Fuel cell technologies - Part 7-2: Test methods - Single cell and stack performance tests for solid oxide fuel cells (SOFC). Technical Specification. International Electrotechnical Commission; 2014. Report No.: TS 62282-7-2:2014.

[21] Energy storage systems using fuel cell modules in reverse mode - Solid oxide single cell and stack performance including reversing operation. Technical Specification. International Electrotechnical Commission; 2016. Report No.: TS 62282-8-101.

[22] Njodzefon J-C, Klotz D, Kromp A, Weber A, Ivers-Tiff,e E. Electrochemical modeling of the current-voltage characteristics of an SOFC in fuel cell and electrolyzer operation modes. *J Electrochem Soc* 2013;**160**(4):F313–FF23.

[23] Achenbach E. IEA Programme on R, D&D on Advanced Fuel Cells Annex II: Modeling and Evaluation of Advanced Solid Oxide Fuel Cells, SOFC Stack Modeling. Juelich: International Energy Agency; 1996. IEA Programme on Advanced Fuel Cells Annex II.

[24] Ferguson J, Fiard J, Herbin R. Three-dimensional numerical simulation for various geometries of solid oxide fuel cells. *J Pow Sour* 1996;**58**(2):109–22.

[25] Le AD, Beale SB, Pharoah JG. Validation of a solid oxide fuel cell model on the International Energy Agency benchmark case with hydrogen fuel. *Fuel Cells* 2015;**15**(1):27–41.

[26] Macdonald JR. Impedance spectroscopy: emphasizing solid materials and systems. *ApOpt* 1989;**28**(6):1083.

[27] Barsoukov E, Macdonald JR. Impedance Spectroscopy Theory, Experiment, and. Applications. Hoboken, NJ: John Wiley &Sons, Inc; 2005. p. 2005.

[28] Orazem ME, Tribollet B. *Electrochemical impedance spectroscopy*. New Jersey; 2008.

[29] Lasia A. Electrochemical impedance spectroscopy and its applications. Modern aspects of electrochemistry: Springer; 2002. p. 143–248.

[30] Klotz D, Weber A, Ivers-Tiffée E. Practical guidelines for reliable electrochemical characterization of solid oxide fuel cells. *Electrochimica Acta* 2017;**227**:110–26.

[31] Schönleber M, Klotz D, Ivers-Tiffée E. A Method for Improving the Robustness of linear Kramers-Kronig Validity Tests. *Electrochimica Acta* 2014;**131**:20–7.

[32] Karlsruhe Institute of Technoloy, IAM-ET web site http://www.iam.kit.edu/et/english/Lin-kk.php.

[33] Schichlein H, Muller A, Voigts M, Krugel A, Ivers-Tiffee E. Deconvolution of electrochemical impedance spectra for the identification of electrode reaction mechanisms in solid oxide fuel cells. *J Appl Electrochem* 2002;**32**(8):875–82.

[34] Ivers-Tiffee E, Weber A. Evaluation of electrochemical impedance spectra by the distribution of relaxation times. *J Ceram Soc Jpn* 2017;**125**(4):193–201.

[35] Leonide A, Hansmann S, Weber A, Ivers-Tiffée E. Performance simulation of current/voltage-characteristics for SOFC single cell by means of detailed impedance analysis. *J Pow Sour* 2011;**196**(17):7343–6.

[36] Leonide A, Hansmann S, Ivers-Tiffée E. A 0-Dimensional Stationary Model for Anode-Supported Solid Oxide Fuel Cells. *ECS Transactions* 2010;**28**(11):341–6.

[37] Endler-Schuck C, Joos J, Niedrig C, Weber A, Ivers-Tiffée E. The chemical oxygen surface exchange and bulk diffusion coefficient determined by impedance spectroscopy of porous La0.58Sr0.4Co0.2Fe0.8O3 $-\delta$ (LSCF) cathodes. *Solid State Ionics* 2015;**269**:67–79.

[38] Dierickx S, Joos J, Weber A, Ivers-Tiffée E. Advanced impedance modelling of Ni/8YSZ cermet anodes. *Electrochimica Acta* 2018;**265**:736–50.

[39] Bessler WG. A new computational approach for SOFC impedance from detailed electrochemical reaction–diffusion models. *Solid State Ionics* 2005;**176**(11-12):997–1011.

[40] Bessler WG. Rapid impedance modeling via potential step and current relaxation simulations. *J Electrochem Soc* 2007;**154**(11):B1186.

[41] Bessler WG, Gewies S, Vogler M. A new framework for physically based modeling of solid oxide fuel cells. *Electrochimica Acta* 2007;**53**(4):1782–800.

[42] Klotz D, Njodzefon J-C, Weber A, Ivers-Tiffée E. Current-voltage and temperature characteristics of anode supported solid oxide electrolyzer cells (SOEC). *ECS Transactions* 2012;**45**(1):523–30.

[43] Silva-Mosqueda DM, Elizalde-Blancas F, Pumiglia D, Santoni F, Boigues–Muñoz C, McPhail SJ. Intermediate temperature solid oxide fuel cell under internal reforming: critical operating conditions, associated problems and their impact on the performance. *Applied Energy* 2019;**235**:625–40.

[44] Guk E, Kim J-S, Ranaweera M, Venkatesan V, Jackson L. In-situ monitoring of temperature distribution in operating solid oxide fuel cell cathode using proprietary sensory techniques versus commercial thermocouples. *Applied Energy* 2018;**230**:551–62.

[45] Tallgren J, Boigues Muñoz C, Mikkola J, Himanen O, Kiviaho J. Determination of Temperature and Fuel Utilization Distributions in SOFC Stacks with EIS. *ECS Transactions* 2017;**78**(1):2141–50.

[46] Fang Q, Blum L, Batfalsky P, Menzler NH, Packbier U, Stolten D. Durability test and degradation behavior of a 2.5 kW SOFC stack with internal reforming of LNG. *Int J Hydro Energy* 2013;**38**(36):16344–53.

[47] Blum L, De Haart LB, Malzbender J, Menzler NH, Remmel J, Steinberger-Wilckens R. Recent results in Jülich solid oxide fuel cell technology development. *J Pow Sour* 2013;**241**:477–85.

[48] Freundt P. Systemnahe thermische Charakterisierung eines oxidkeramischen Brennstoffzellen-Stacks für die mobile Anwendung: Universität Stuttgart; 2015.

[49] Mai BE, Heller T, Schimanke D, Lawrence J, Wunderlich C. Influence of operating conditions on the reliable performance of stacks and integrated stack modules. *ECS Transactions* 2009;**25**(2):187.

[50] Yan A, Huang S, Li S, Chen R, Ohodnicki P, Buric M, et al. Distributed optical fiber sensors with ultrafast laser enhanced Rayleigh backscattering profiles for real-time monitoring of solid oxide fuel cell operations. *Sci Rep-Uk* 2017;**7**(1):1–9.

[51] Pumiglia D, Santoni F, Viceconti E, Conti B, Boigues Muñoz C, Bosio B, et al. SOFC anode process characterization by means of a spot-sampling set-up for in-operando gas analysis. *ECS Transactions* 2017;**75**(49):1–8.

[52] Ravussin F, Autissier N, Molinelli M, Larrain D, Favrat D. Local current measurement in a solid oxide fuel cell repeat element. *J Eur Ceram Soc* 2007;**27**(2-3):1035–40.

[53] Wuillemin Z, Antonetti Y, Beetschen C, Millioud O, Ceschini S, Madi H. Local activation and degradation of electrochemical processes in a SOFC. *ECS Transactions* 2013;**57**(1):561–70.

[54] Timmermann H, Fouquet D, Weber A, Ivers-Tiff,e E, Hennings U, Reimert R. Internal reforming of methane at Ni/YSZ and Ni/CGO SOFC cermet anodes. *Fuel Cells* 2006;**6**(3-4):307–13.

[55] Santoni F, Mosqueda DS, Pumiglia D, Viceconti E, Conti B, Muñoz CB, et al. In--situ study of the gas-phase composition and temperature of an intermediate-temperature solid oxide fuel cell anode surface fed by reformate natural gas. *J Pow Sour* 2017;**370**:36–44.

[56] Lu X, Faguy PW, Liu M. In Situ Potential-Dependent FTIR Emission Spectroscopy: A Novel Probe for High Temperature Fuel Cell Interfaces. *J Electrochem Soc* 2002;**149**(10):A1293–A12A8.

[57] Brett DJL, Aguiar P, Clague R, Marquis AJ, Schöttl S, Simpson R, et al. Application of infrared thermal imaging to the study of pellet solid oxide fuel cells. *J Pow Sour* 2007;**166**(1):112–19.

[58] Pomfret MB, Steinhurst DA, Kidwell DA, Owrutsky JC. Thermal imaging of solid oxide fuel cell anode processes. *J Pow Sour* 2010;**195**(1):257–62.

[59] Pomfret MB, Owrutsky JC, Walker RA. In situ studies of fuel oxidation in solid oxide fuel cells. *Anal Chem* 2007;**79**(6):2367–72.

[60] Saunders JEA, Davy MH. High-temperature vibrational Raman spectroscopy of gaseous species for solid-oxide fuel cell research. *Int J Hydro Energy* 2012;**37**(4):3403–14.

[61] Schiller G, Auer C, Bessler WG, Christenn C, Ilhan Z, Szabo P, et al. A novel concept for in situ gas-phase laser Raman spectroscopy for solid oxide fuel cell research. *Applied Physics B* 2013;**111**(1):29–38.

[62] Andersson M, Paradis H, Yuan JL, Sunden B. Three dimensional modeling of an solid oxide fuel cell coupling charge transfer phenomena with transport processes and heat generation. *Electrochimica Acta* 2013;**109**:881–93.

[63] Bieberle A, Gauckler L. Reaction mechanism of Ni pattern anodes for solid oxide fuel cells. *Solid State Ionics* 2000;**135**(1-4):337–45.

[64] DeCaluwe SC, Weddle PJ, Zhu H, Colclasure AM, Bessler WG, Jackson GS, et al. On the fundamental and practical aspects of modeling complex electrochemical kinetics and transport. *J Electrochem Soc* 2018;**165**(13):E637.

[65] Goodwin DG, Moffat HK, Speth RL. *Cantera: An object-oriented software toolkit for chemical kinetics, thermodynamics, and transport processes*. Caltech, Pasadena, CA; 2009.

[66] Goodwin DG, Speth R, Moffat H, Weber B. Cantera: An object-oriented software toolkit for chemical kinetics, thermodynamics, and transport processes, Version. 2.4. 0, 2018. https://www.cantera.org.

[67] Zhu H, Kee RJ, Janardhanan VM, Deutschmann O, Goodwin DG. Modeling elementary heterogeneous chemistry and electrochemistry in solid-oxide fuel cells. *J Electrochem Soc* 2005;**152**(12):A2427.

[68] Peksen M. 3D thermomechanical behaviour of solid oxide fuel cells operating in different environments. *Int J Hydro Energy* 2013;**38**(30):13408–18.

[69] Peksen M, Peters R, Blum L, Stolten D. Hierarchical 3D multiphysics modelling in the design and optimisation of SOFC system components. *Int J Hydro Energy* 2011;**36**(7):4400–8.

[70] Rashid K, Dong SK, Khan RA, Park SH. Optimization of manifold design for 1 kW-class flat-tubular solid oxide fuel cell stack operating on reformed natural gas. *J Pow Sour* 2016;**327**:638–52.

[71] Bi WX, Li JY, Lin ZJ. Flow uniformity optimization for large size planar solid oxide fuel cells with U-type parallel channel designs. *J Pow Sour* 2010;**195**(10):3207–14.

[72] Liu S, Song C, Lin Z. The effects of the interconnect rib contact resistance on the performance of planar solid oxide fuel cell stack and the rib design optimization. *J Pow Sour* 2008;**183**(1):214–25.

[73] Chen Q, Zeng M, Zhang J, Wang Q. Optimal design of bi-layer interconnector for SOFC based on CFD-Taguchi method. *Int J Hydro Energy* 2010;**35**(9):4292–300.

[74] Achenbach E. Three-dimensional and time-dependent simulation of a planar solid oxide fuel cell stack. *J Pow Sour* 1994;**49**(1-3):333–48.

[75] Bessette NF, Wepfer WJ. Prediction of on-design and off-design performance for a solid oxide fuel cell power module. *Energy Conver Manage* 1996;**37**(3):281–93.

[76] Beale SB, Zhubrin SV. A distributed resistance analogy for solid oxide fuel cells. *Numerical Heat Transfer Part B* 2005;**47**(6):573–91.

[77] Chan S, Khor K, Xia Z. A complete polarization model of a solid oxide fuel cell and its sensitivity to the change of cell component thickness. *J Pow Sour* 2001;**93**(1):130–40.

[78] Recknagle KP, Williford RE, Chick LA, Rector DR, Khaleel MA. Three-dimensional thermo-fluid electrochemical modeling of planar SOFC stacks. *J Pow Sour* 2003;**113**(1):109–14.

[79] Khaleel M, Lin Z, Singh P, Surdoval W, Collin D. A finite element analysis modeling tool for solid oxide fuel cell development: coupled electrochemistry, thermal and flow analysis in MARC®. *J Pow Sour* 2004;**130**(1-2):136–48.

[80] Khaleel M, Rector D, Lin Z, Johnson K, Recknagle K. Multiscale electrochemistry modeling of solid oxide fuel cells. *Int J Multiscale Comput Eng* 2005;**3**(1):33–47.

[81] Janardhanan VM, Deutschmann O. Numerical study of mass and heat transport in solid-oxide fuel cells running on humidified methane. *Chem Eng Sci* 2007;**62**(18):5473–86.

[82] Janardhanan VM, Deutschmann O. CFD analysis of a solid oxide fuel cell with internal reforming: Coupled interactions of transport, heterogeneous catalysis and electrochemical processes. *J Pow Sour* 2006;**162**(2):1192–202.

[83] Zhu W, Ding D, Xia C. Enhancement in three-phase boundary of SOFC electrodes by an ion impregnation method: a modeling comparison. *Electrochem Solid-State Lett* 2008;**11**(6):B83–BB6.

[84] Kim J, Liu W, Lee C. Multi-scale solid oxide fuel cell materials modeling. *Comput Mech* 2009;**44**(5):683–703.

[85] Shi J, Xue X. CFD analysis of a symmetrical planar SOFC with heterogeneous electrode properties. *Electrochimica Acta* 2010;**55**(18):5263–73.

[86] Sudaprasert K, Travis R, Martinez-Botas R. A study of temperature distribution across a solid oxide fuel cell stack. *J Fuel Cell Sci Tech* 2010;**7**(1).

[87] He Z, Birgersson E, Li H. Reduced non-isothermal model for the planar solid oxide fuel cell and stack. *Energy* 2014;**70**:478–92.

[88] Nishida RT, Beale SB, Pharoah JG. Computational Fluid Dynamics Modelling of Solid Oxide Fuel Cell Stacks. *Int J Hydro Energy* 2016 Submitted.

[89] Nishida R, Beale S, Pharoah J, de Haart L, Blum L. Three-dimensional computational fluid dynamics modelling and experimental validation of the Jülich Mark-F solid oxide fuel cell stack. *J Pow Sour* 2018;**373**:203–10.

[90] Li A, Fang X, Lin Z. A High Resolution Multi-Physics Numerical Model for Planar SOFC Stack. *ECS Transactions* 2015;**68**(1):3025–42.

[91] Kakaç S, Pramuanjaroenkij A, Zhou XY. A review of numerical modeling of solid oxide fuel cells. *Int J Hydro Energy* 2007;**32**(7):761–86.

[92] Colpan C, Dincer I, Hamdullahpur F. A review on macro-level modeling of planar solid oxide fuel cells. *Int J Energy Res* 2008;**32**(4):336–55.

[93] Andersson M, Yuan J, Sunden B. Review on modeling development for multiscale chemical reactions coupled transport phenomena in solid oxide fuel cells. *Applied Energy* 2010;**87**(5):1461–76.

[94] Bavarian M, Soroush M, Kevrekidis I, Benziger J. Mathematical Modeling, Steady-State and Dynamic Behavior, and Control of Fuel Cells: A Review. *Indust Eng Chem Res* 2010;**49**(17):7922–50.

[95] Hajimolana SA, Hussain MA, Daud WAW, Soroush M, Shamiri A. Mathematical modeling of solid oxide fuel cells: A review. *Renew Sustain Energy Rev* 2011;**15**(4):1893–917.

[96] Wang K, Hissel D, Péra M, Steiner N, Marra D, Sorrentino M, et al. A review on solid oxide fuel cell models. *Int J Hydro Energy* 2011;**36**(12):7212–28.

[97] Grew K, Chiu W. A review of modeling and simulation techniques across the length scales for the solid oxide fuel cell. *J Pow Sour* 2012;**199**:1–13.

[98] Peksen M. Numerical thermomechanical modelling of solid oxide fuel cells. *Prog Energy Combust Sci* 2015;**48**:1–20.

[99] Bao C, Wang Y, Feng D, Jiang Z, Zhang X. Macroscopic modeling of solid oxide fuel cell (SOFC) and model-based control of SOFC and gas turbine hybrid system. *Prog Energy Combust Sci* 2018;**66**:83–140.

[100] Zabihian F, Fung AS. Macro-level modeling of solid oxide fuel cells, approaches, and assumptions revisited. *J Renew Sustain Energy* 2017;**9**(5):054301.

[101] Torabi M, Karimi N, Peterson GP, Yee S. Challenges and progress on the modelling of entropy generation in porous media: A review. *Int J Heat and Mass Transfer* 2017;**114**:31–46.

[102] Ryan EM, Mukherjee PP. Mesoscale modeling in electrochemical devices—A critical perspective. *Prog Energy Combust Sci* 2019;**71**:118–42.

[103] Tjaden B, Brett DJL, Shearing PR. Tortuosity in electrochemical devices: a review of calculation approaches. *Int Mater Rev* 2018;**63**(2):47–67.

[104] Jiang C, Gu Y, Guan W, Zheng J, Ni M, Zhong Z. 3D thermo-electro-chemo-mechanical coupled modeling of solid oxide fuel cell with double-sided cathodes. *Int J Hydro Energy* 2019.

[105] Kim YJ, Lee MC. Numerical investigation of flow/heat transfer and structural stress in a planar solid oxide fuel cell. *Int J Hydro Energy* 2017;**42**(29):18504–13.

[106] Wang C, Jj Yang, Huang W, Zhang T, Yan D, Pu J, et al. Numerical simulation and analysis of thermal stress distributions for a planar solid oxide fuel cell stack with external manifold structure. *Int J Hydro Energy* 2018;**43**(45):20900–10.

[107] Zeng S, Parbey J, Yu G, Xu M, Li T, Andersson M. Thermal stress analysis of sulfur deactivated solid oxide fuel cells. *J Pow Sour* 2018;**379**:134–43.

[108] Muramatsu M. Numerical simulations of non-stationary distributions of electrochemical potentials in SOFC. *Eng Comput* 2017;**34**(6):1956–88.

[109] Chen B, Xu H, Tan P, Zhang Y, Xu X, Cai W, et al. Thermal modelling of ethanol-fuelled Solid Oxide Fuel Cells. *Applied Energy* 2019;**237**:476–86.

[110] Perna A, Minutillo M, Jannelli E, Cigolotti V, Nam SW, Han J. Design and performance assessment of a combined heat, hydrogen and power (CHHP) system based on ammonia-fueled SOFC. *Applied Energy* 2018;**231**:1216–29.

[111] Palomba V, Ferraro M, Frazzica A, Vasta S, Sergi F, Antonucci V. Experimental and numerical analysis of a SOFC-CHP system with adsorption and hybrid chillers for telecommunication applications. *Applied Energy* 2018;**216**:620–33.

[112] Brunaccini G, Sergi F, Aloisio D, Ferraro M, Blesznowski M, Kupecki J, et al. Modeling of a SOFC-HT battery hybrid system for optimal design of off-grid base transceiver station. *Int J Hydro Energy* 2017;**42**(46):27962–78.

[113] Giacoppo G, Barbera O, Briguglio N, Cipitì F, Ferraro M, Brunaccini G, et al. Thermal study of a SOFC system integration in a fuselage of a hybrid electric mini UAV. *Int J Hydro Energy* 2017;**42**(46):28022–33.

[114] Rossi I, Traverso A, Tucker D. SOFC/Gas Turbine Hybrid System: A simplified framework for dynamic simulation. *Applied Energy* 2019;**238**:1543–50.

[115] Ni M, Leung MKH, Leung DC. A modeling study on concentration overpotentials of a reversible solid oxide fuel cell. *J Pow Sour* 2006;**163**(1):460–6.

[116] Ni M, Leung MKH, Leung DY. Theoretical analysis of reversible solid oxide fuel cell based on proton-conducting electrolyte. *J Pow Sour* 2008;**177**(2):369–75.

[117] Udagawa J, Aguiar P, Brandon N. Hydrogen production through steam electrolysis: Model-based steady state performance of a cathode-supported intermediate temperature solid oxide electrolysis cell. *J Pow Sour* 2007;**166**(1):127–36.

[118] Udagawa J, Aguiar P, Brandon N. Hydrogen production through steam electrolysis: Model-based dynamic behaviour of a cathode-supported intermediate temperature solid oxide electrolysis cell. *J Pow Sour* 2008;**180**(1):46–55.

[119] Ni M. Computational fluid dynamics modeling of a solid oxide electrolyzer cell for hydrogen production. *Int J Hydro Energy* 2009;**34**(18):7795–806.

[120] Ni M. Modeling of a solid oxide electrolysis cell for carbon dioxide electrolysis. *Chem Eng J* 2010;**164**(1):246–54.

[121] Ni M. 2D thermal modeling of a solid oxide electrolyzer cell (SOEC) for syngas production by H2O/CO2 co-electrolysis. *Int J Hydro Energy* 2012;**37**(8):6389–99.

[122] Hawkes G, O'Brien J, Stoots C, Hawkes B. 3D CFD model of a multi-cell high-temperature electrolysis stack. *Int J Hydro Energy* 2009;**34**(9):4189–97.

[123] Choi H, Pharoah J, Ryland D, Kettner A, Gnanapragasam N, Kawada T, et al. Computational fluid dynamics modeling of solid oxide electrolysis cell. *Solid Oxide Fuel Cells 13 (Sofc-Xiii)* 2013;**57**(1):3161–70.

[124] Beale S, Choi H, Pharoah J, Roth H, Jasak H, Jeon D. Open-source computational model of a solid oxide fuel cell. *Comp Phys Commun* 2016;**200**:15–26.

[125] Ni M, Leung MKH, Leung DYC. Technological development of hydrogen production by solid oxide electrolyzer cell (SOEC). *Int J Hydro Energy* 2008;**33**(9):2337–54.

[126] Leonide A, Sonn V, Weber A, Ivers-Tiffée E. Evaluation and modeling of the cell resistance in anode-supported solid oxide fuel cells. *J Electrochem Soc* 2008;**155**(1):B36–41.

[127] Geisler H, Kromp A, Weber A, Ivers-Tiffée E. Stationary FEM model for performance evaluation of planar solid oxide fuel cells connected by metal interconnectors I. Model framework and validation. *J Electrochem Soc* 2014;**161**(6):F778–FF88.

[128] Gong W, Cai Z, Yang J, Li X, Jian L. Parameter identification of an SOFC model with an efficient, adaptive differential evolution algorithm. *Int J Hydro Energy* 2014;**39**(10):5083–96.

[129] Danilov VA, Tade MO. A new technique of estimating anodic and cathodic charge transfer coefficients from SOFC polarization curves. *Int J Hydro Energy* 2009;**34**(16):6876–81.

[130] Reiss G, Frandsen HL, Brandstätter W, Weber A. Numerical evaluation of micro-structural parameters of porous supports in metal-supported solid oxide fuel cells. *J Pow Sour* 2015;**273**:1006–15.

[131] Zheng K, Zhang Y, Li L, Ni M. On the tortuosity factor of solid phase in solid oxide fuel cell electrodes. *Int J Hydro Energy* 2015;**40**(1):665–9.

[132] Bertei A, Nicolella C. Percolation theory in SOFC composite electrodes: effects of porosity and particle size distribution on effective properties. *J Pow Sour* 2011;**196**(22):9429–36.

[133] Kulikovsky A. *Analytical modelling of fuel cells*. Amsterdam: Elsevier; 2010.

[134] Beale SB, Lin Y, Zhubrin SV, Dong W. Computer methods for performance prediction in fuel cells. *J Pow Sour* 2003;**118**(1-2):79–85.

[135] Navasa M, Frandsen HL, Skafte TL, Sundén B, Graves C. Localized carbon deposition in solid oxide electrolysis cells studied by multiphysics modeling. *J Pow Sour* 2018;**394**:102–13.

[136] Navasa M, Graves C, Chatzichristodoulou C, Skafte T, Sunden B, Frandsen H. A three dimensional multiphysics model of a solid oxide electrochemical cell: A tool for understanding degradation. *Int J Hydro Energy* 2018;**43**(27):11913–31.

[137] Todd B, Young JB. Thermodynamic and transport properties of gases for use in solid oxide fuel cell modelling. *J Pow Sour* 2002;**110**(1):186–200.

[138] Hernandez-Pacheco E, Mann MD. The rational approximation method in the prediction of thermodynamic properties for SOFCs. *J Pow Sour* 2004;**128**(1):25–33.

[139] Gileadi E. *Electrode Kinetics for Chemists, Chemical Engineers and Materials Scientists*. Wiley; 1993.

[140] Andersson M, Yuan J, Sunden B. SOFC modeling considering hydrogen and carbon monoxide as electrochemical reactants. *J Pow Sour* 2013;**232**:42–54.

[141] Bird RB, Stewart WE, Lightfoot EN. *Transport Phenomena*. 2nd edn. New York: Wiley; 2002.

[142] Beale SB. A simple, effective viscosity formulation for turbulent flow and heat transfer in compact heat exchangers. *Heat Transfer Eng* 2012;**33**(1):4–11.

[143] Wilke C. A viscosity equation for gas mixtures. *J Chem Phys* 1950;**18**(4):517–19.

[144] Beale S. Calculation procedure for mass transfer in fuel cells. *J Pow Sour* 2004;**128**(2):185–92.

[145] Beale SB. Mass transfer in plane and square ducts. *Int J Heat and Mass Transfer* 2005;**48**(15):3256–60.

[146] Taylor R, Krishna R. *Multicomponent mass transfer*. New York: Wiley-Interscience; 1993.

[147] Wilke CR. Diffusional properties of multicomponent gases. *Chem Eng Progress* 1950;**46**(2):95–104.

[148] Fuller E, Schettler P, Giddings J. New method for prediction of binary gas-phase diffusion coefficients. *Indust Eng Chem* 1966;**58**(5):18–27.

[149] Poling B, Prausnitz J, Connell J. *The properties of gases and liquids*. McGraw-Hill New York; 2001.

[150] Epstein N. On Tortuosity and the Tortuosity Factor in Flow and Diffusion through Porous Media. *Chem Eng Sci* 1989;**44**(3):777–9.

[151] Bruggeman D. Calculation of various physics constants in heterogenous substances I Dielectricity constants and conductivity of mixed bodies from isotropic substances. *Annalen Der Physik* 1935;**24**(7):636–64.

[152] Choi H, Berson A, Pharoah J, Beale S. Effective transport properties of the porous electrodes in solid oxide fuel cells. *Proc Inst Mech Eng Part A J Power and Energy* 2011;**225**(2):183–97.

[153] Maxwell J. Diffusion. Encyclopedia Britannica. 9th ed 1878. p. 214-21.

[154] Stefan J. Über das Gleichgewicht und Bewegung, insbesondere die Diffusion von Gemischen. *Sitzungsberichte der Kaiserlichen Akademie der Wissenschaften Wien, 2te Abteilung* 1871;**63**:63–124.

[155] Tseronis K, Bonis I, Kookos I, Theodoropoulos C. Parametric and transient analysis of non-isothermal, planar solid oxide fuel cells. *Int J Hydro Energy* 2012;**37**(1):530–47.

[156] Runstedtler A. On the modified Stefan–Maxwell equation for isothermal multicomponent gaseous diffusion. *Chem Eng Sci* 2006;**61**(15):5021–9.

[157] Kleijn C, Van Der Meer TH, Hoogendoorn C. A mathematical model for LPCVD in a single wafer reactor. *J Electrochem Soc* 1989;**136**(11):3423–33.

[158] Krishna R, Standart GL. Mass and energy-transfer in multiomponent systems. *Chem Eng Commun* 1979;**3**(4-5):201–75.

[159] Krishna R. Simulation and optimization of an industrial ammonia reactor - comments. *Indust Eng Chem Res* 1989;**28**(8):1266.

[160] Kubota H, Yamanaka Y, Dalla Lana IG. Effective diffusivity of multicomponent gaseousreaction systems. application to catalyst effectiveness factor. *J Chem Eng Jpn* 1969;**2**:71–5.

[161] Bosanquet C. British TA Report BR-507. 1944.

[162] Pollard WG, Present RD. On gaseous self-diffusion in long capillary tubes. *Phys Rev* 1948;**73**(7):762–74.

[163] Mason EA, Malinauskas A. *Gas transport in porous media: the dusty-gas model*. Elsevier Science Ltd; 1983.

[164] Veldsink J, Van Damme R, Versteeg G, Van Swaaij W. The use of the dusty-gas model for the description of mass transport with chemical reaction in porous media. *Chem Eng J Biochem Eng J* 1995;**57**(2):115–25.

[165] Webb SW. *Gas-phase diffusion in porous media: Evaluation of an advective-dispersive formulation and the dusty-gas model including comparison to data for binary mixtures*. Sandia National Laboratories; 1996.

[166] Nield DA, Bejan A. *Mechanics of fluid flow through a porous medium*. Convection in Porous Media: Springer; 2013. p. 1–29.

[167] Bertei A, Nicolella C. Common inconsistencies in modeling gas transport in porous electrodes: The dusty-gas model and the Fick law. *J Pow Sour* 2015;**279**:133–7.

[168] Evans III R, Watson G, Truitt J. Interdiffusion of gases in a low permeability graphite at uniform pressure. *J Appl Phys* 1962;**33**(9):2682–8.

[169] Kong W, Zhu H, Fei Z, Lin Z. A modified dusty gas model in the form of a Fick's model for the prediction of multicomponent mass transport in a solid oxide fuel cell anode. *J Pow Sour* 2012;**206**:171–8.

[170] Suwanwarangkul R, Croiset E, Fowler M, Douglas P, Entchev E, Douglas M. Performance comparison of Fick's, dusty-gas and Stefan–Maxwell models to predict the concentration overpotential of a SOFC anode. *J Pow Sour* 2003;**122**(1):9–18.

[171] Zhang YX, Xia CR, Ni M. Simulation of sintering kinetics and microstructure evolution of composite solid oxide fuel cells electrodes. *Int J Hydro Energy* 2012;**37**(4):3392–402.

[172] Bao C, Jiang Z, Zhang X. Modeling mass transfer in solid oxide fuel cell anode: I. Comparison between Fickian, Stefan-Maxwell and dusty-gas models. *J Pow Sour* 2016;**310**:32–40.

[173] Kerkhof PJAM. A modified Maxwell-Stefan model for transport through inert membranes: the binary friction model. *Chem Eng J Biochem Eng J* 1996;**64**(3):319–43.

[174] Young JB, Todd B. Modelling of multi-component gas flows in capillaries and porous solids. *Int J Heat and Mass Transfer* 2005;**48**(25):5338–53.

[175] Beale SB. Use of streamwise periodic boundary conditions for problems in heat and mass transfer. *J Heat Transfer* 2007;**129**(4):601–5.

[176] Weber N, Landgraf S, Mushtaq K, Nimtz M, Personnettaz P, Weier T, et al. Modeling discontinuous potential distributions using the finite volume method, and application to liquid metal batteries. *Electrochimica Acta* 2019;**318**:857–64.

[177] Glasstone S, Laidler KJ, Eyring H. *The Theory of Rate Processes: The Kinetics of Chemical Reactions, Viscosity, Diffusion and Electrochemical Phenomena*. New York: McGraw-Hill; 1941.

[178] Leonide A, Apel Y, Ivers-Tiffée E. SOFC modeling and parameter identification by means of impedance spectroscopy. *ECS Transactions* 2009;**19**(20):81–109.

[179] Kulikovsky A. A physically–based analytical polarization curve of a PEM fuel cell. *J Electrochem Soc* 2014;**161**(3):F263–FF70.

[180] Perry ML. Mass Transport in Gas-Diffusion Electrodes: A Diagnostic Tool for Fuel-Cell Cathodes. *J Electrochem Soc* 1998;**145**(1):5.

[181] Hecht ES, Gupta GK, Zhu H, Dean AM, Kee RJ, Maier L, et al. Methane reforming kinetics within a Ni–YSZ SOFC anode support. *Appl Catal A Gen* 2005;**295**(1):40–51.

[182] Lee WY, Wee D, Ghoniem AF. An improved one-dimensional membrane-electrode assembly model to predict the performance of solid oxide fuel cell including the limiting current density. *J Pow Sour* 2009;**186**(2):417–27.

[183] Hauch A, Jensen SH, Ramousse S, Mogensen M. Performance and durability of solid oxide electrolysis cells. *J Electrochem Soc* 2006;**153**(9):A1741.

[184] Klotz D, Leonide A, Weber A, Ivers-Tiffée E. Electrochemical model for SOFC and SOEC mode predicting performance and efficiency. *Int J Hydro Energy* 2014;**39**(35):20844–9.

[185] Steele BC. Survey of materials selection for ceramic fuel cells II. Cathodes and anodes. *Solid State Ionics* 1996;**86**:1223–34.

[186] Ouweltjes J, Aravind P, Woudstra N, Rietveld G. Biosyngas utilization in solid oxide fuel cells with Ni/ GDC anodes. *J Fuel Cell Sci Tech* 2006;**3**(4):495–8.

[187] Murray EP, Tsai T, Barnett SA. A direct-methane fuel cell with a ceria-based anode. *Nature* 1999;**400**(6745):649–51.

[188] Völker B, McMeeking RM. Impact of particle size ratio and volume fraction on effective material parameters and performance in solid oxide fuel cell electrodes. *J Pow Sour* 2012;**215**:199–215.

[189] Costamagna P, Costa P, Antonucci V. Micro-modelling of solid oxide fuel cell electrodes. *Electrochimica Acta* 1998;**43**(3):375–94.

[190] Sunde S. Simulations of composite electrodes in fuel cells. *J Electroceram* 2000;**5**(2):153–82.

[191] Serincan MF, Pasaogullari U, Singh P. Controlling reformation rate for a more uniform temperature distribution in an internal methane steam reforming solid oxide fuel cell. *J Pow Sour* 2020;**468**:228310.

[192] Lehnert W, Meusinger J, Thom F. Modelling of gas transport phenomena in SOFC anodes. *J Pow Sour* 2000;**87**(1):57–63.

[193] Wang B, Zhu J, Lin Z. A theoretical framework for multiphysics modeling of methane fueled solid oxide fuel cell and analysis of low steam methane reforming kinetics. *Applied Energy* 2016;**176**:1–11.

[194] Nguyen VN, Deja R, Peters R, Blum L. Methane/steam global reforming kinetics over the Ni/YSZ of planar pre-reformers for SOFC systems. *Chem Eng J* 2016;**292**:113–22.

[195] Nagel F, Schildhauer T, Biollaz S, Wokaun A. Performance comparison of planar, tubular and Delta8 solid oxide fuel cells using a generalized finite volume model. *J Pow Sour* 2008;**184**(1):143–64.

[196] Paradis H, Andersson M, Yuan J, Sunden B. CFD modeling: different kinetic approaches for internal reforming reactions in an anode-supported SOFC. *J Fuel Cell Sci Tech* 2011;**8**(3).

[197] Drescherl. Kinetik der Methan-Dampf-Reformierung (Kinetics of methane steam reforming). Jülich, Germany: Forschungszentrum Jülich GmbH, Energietechnik IfWuVd; 1999 September 1999. Report No.: Berichte des Forschungszentrum Jülich 3699.

[198] Haberman B, Young J. Three-dimensional simulation of chemically reacting gas flows in the porous support structure of an integrated-planar solid oxide fuel cell. *Int J Heat and Mass Transfer* 2004;**47**(17):3617–29.

[199] Andersson M, Nakajima H, Kitahara T, Shimizu A, Koshiyama T, Paradis H, et al. Comparison of humidified hydrogen and partly pre-reformed natural gas as fuel for solid oxide fuel cells applying computational fluid dynamics. *Int J Heat and Mass Transfer* 2014;**77**:1008–22.

[200] Ni M. Modeling of SOFC running on partially pre-reformed gas mixture. *Int J Hydro Energy* 2012;**37**(2):1731–45.

[201] Chase Jr MW. NIST-JANAF thermochemical tables. *J Phys Chem Ref Data Monograph* 1998:9.

[202] Koch S. *Contact resistance of ceramic interfaces between materials used in solid oxide fuel cell applications*. Denmark Technical University; 2002.

[203] Singhal V, Litke P, Black A, Garimella S. An experimentally validated thermo-mechanical model for the prediction of thermal contact conductance. *Int J Heat and Mass Transfer* 2005;**48**(25-26):5446–59.

[204] Black A, Singhal V, Garimella S. Analysis and prediction of constriction resistance for contact between rough engineering surfaces. *J Thermophys Heat Transfer* 2004;**18**(1):30–6.

[205] Fletcher L. Thermal contact resistance. In: Hewitt G, Shires G, Polezhaev Y, editors. *International Encyclopedia of Heat and Mass Transfer, 1997*. New York: CRC Press; 1997. p. 1147–9.

[206] Beale SB. Conjugate mass transfer in gas channels and diffusion layers of fuel cells. *J Fuel Cell Sci Tech* 2006;**4**(1):1–10.

[207] Shah RK, London AL. Laminar flow forced convection in ducts. *Advances in Heat Transfer*. Irvine TF, Hartnett JP, editors. New York: Academic Press; 1978.

[208] Damm DL, Fedorov AG. Radiation heat transfer in SOFC materials and components. *J Pow Sour* 2005;**143**(1-2):158–65.

[209] Yakabe H, Ogiwara T, Hishinuma M, Yasuda I. 3-D model calculation for planar SOFC. *J Pow Sour* 2001;**102**(1-2):144–54.

[210] Burt AC, Celik IB, Gemmen RS, Smirnov AV. A numerical study of cell-to-cell variations in a SOFC stack. *J Pow Sour* 2004;**126**(1-2):76–87.

[211] VanderSteen JDJ, Pharoah JG. Modeling radiation heat transfer with participating media in solid oxide fuel cells. *J Fuel Cell Sci Tech* 2006;**3**(1):62–7.

[212] Janardhanan VM, Heuveline V, Deutschmann O. Performance analysis of a SOFC under direct internal reforming conditions. *J Pow Sour* 2007;**172**(1):296–307.

[213] Goldin GM, Zhu H, Kee RJ, Bierschenk D, Barnett SA. Multidimensional flow, thermal, and chemical behavior in solid-oxide fuel cell button cells. *J Pow Sour* 2009;**187**(1):123–35.

[214] Bao C, Cai NS, Croiset E. An analytical model of view factors for radiation heat transfer in planar and tubular solid oxide fuel cells. *J Pow Sour* 2011;**196**(6):3223–32.

[215] Aguiar P, Chadwick D, Kershenbaum L. Modelling of an indirect internal reforming solid oxide fuel cell. *Chem Eng Sci* 2002;**57**(10):1665–77.

[216] Haynes C, Wepfer WJ. Characterizing heat transfer within a commercial-grade tubular solid oxide fuel cell for enhanced thermal management. *Int J Hydro Energy* 2001;**26**(4):369–79.

[217] Xue X, Tang J, Sammes N, Du Y. Dynamic modeling of single tubular SOFC combining heat/mass transfer and electrochemical reaction effects. *J Pow Sour* 2005;**142**(1-2):211–22.

[218] Sanchez D, Munoz A, Sanchez T. An assessment on convective and radiative heat transfer modelling in tubular solid oxide fuel cells. *J Pow Sour* 2007;**169**(1):25–34.

[219] Garcia-Camprubi M, Jasak H, Fueyo N. CFD analysis of cooling effects in H-2-fed solid oxide fuel cells. *J Pow Sour* 2011;**196**(17):7290–301.

[220] Modest M. *Radiative heat transfer*. Academic press; 2013.

[221] Tanaka T, Inui Y, Urata A, Kanno T. Three dimensional analysis of planar solid oxide fuel cell stack considering radiation. *Energy Conver Manage* 2007;**48**(5):1491–8.

[222] Damm DL, Fedorov AG. Spectral radiative heat transfer analysis of the planar SOFC. *J Fuel Cell Sci Tech* 2005;**2**(4):258–62.

[223] Daun KJ, Beale SB, Liu F, Smallwood GJ. Radiation heat transfer in planar SOFC electrolytes. *J Pow Sour* 2006;**157**(1):302–10.

[224] Spinnler M, Winter ERF, Viskanta R, Sattelmayer T. Theoretical studies of high-temperature multilayer thermal insulations using radiation scaling. *J Quant Spectrosc Radiat Transf* 2004;**84**(4):477–91.

[225] Spinnler M, Winter ERF, Viskanta R. Studies on high-temperature multilayer thermal insulations. *Int J Heat and Mass Transfer* 2004;**47**:1305–12.

[226] Pecho O, Stenzel O, Iwanschitz B, Gasser P, Neumann M, Schmidt V, et al. 3D microstructure effects in Ni-YSZ anodes: prediction of effective transport properties and optimization of redox stability. *Materials* 2015;**8**(9):5554–85.

[227] Stenzel O, Pecho O, Holzer L, Neumann M, Schmidt V. Predicting effective conductivities based on geometric microstructure characteristics. *AIChE J* 2016;**62**(5):1834–43.

[228] Stenzel O, Pecho O, Holzer L, Neumann M, Schmidt V. Big data for microstructure-property relationships: a case study of predicting effective conductivities. *AIChE J* 2017;**63**(9):4224–32.

[229] Gaiselmann G, Neumann M, Schmidt V, Pecho O, Hocker T, Holzer L. Quantitative relationships between microstructure and effective transport properties based on virtual materials testing. *AIChE J* 2014;**60**(6):1983–99.

[230] Wyllie MRJ, Spangler MB. Application of electrical resistivity measurements to problem of fluid flow in porous media. *AAPG Bulletin* 1952;**36**(2):359–403.

[231] Cornell D, Katz DL. Flow of gases through consolidated porous media. *Indust Eng Chem* 1953;**45**(10):2145–52.

[232] Archie G. The electrical resistivity log as an aid in determining some reservoir characteristics. *Trans Am Inst Mining Metal Eng* 1942;**146**:54–61.

[233] Andersson M, Yuan J, Sunden B. SOFC cell design optimization using the finite element method based CFD approach. *Fuel Cells* 2014;**14**(2):177–88.

[234] Andersson M, Yuan JL, Sunden B. SOFC modeling considering electrochemical reactions at the active three phase boundaries. *Int J Heat and Mass Transfer* 2012;**55**(4):773–88.

[235] Mason E, Saxena S. Approximate formula for the thermal conductivity of gas mixtures. *Physics of Fluids* 1958;**1**(5):361–9.

[236] Bart GCJ. *Thermal conduction in non homogeneous and phase change media*. TU Delft, Delft University of Technology; 1994.

[237] Carson JK, Lovatt SJ, Tanner DJ, Cleland AC. Thermal conductivity bounds for isotropic, porous materials. *Int J Heat and Mass Transfer* 2005;**48**(11):2150–8.

[238] Nam JH, Jeon DH. A comprehensive micro-scale model for transport and reaction in intermediate temperature solid oxide fuel cells. *Electrochimica Acta* 2006;**51**(17):3446–60.

[239] Kornely M, Leonide A, Weber A, Ivers-Tiffée E. Performance limiting factors in anode-supported cells originating from metallic interconnector design. *J Pow Sour* 2011;**196**(17):7209–16.

[240] Joos J, Carraro T, Weber A, Ivers-Tiffée E. Reconstruction of porous electrodes by FIB/SEM for detailed microstructure modeling. *J Pow Sour* 2011;**196**(17):7302–7.

[241] Wilson JR, Kobsiriphat W, Mendoza R, Chen H-Y, Hiller JM, Miller DJ, et al. Three-dimensional reconstruction of a solid-oxide fuel-cell anode. *Nat Mater* 2006;**5**:541.

[242] Gawel DA, Pharoah JG, Beale SB. Development of a SOFC performance model to analyze the powder to power performance of electrode microstructures. *ECS Transactions* 2015;**68**(1):1979–87.

[243] Costamagna P, Panizza M, Cerisola G, Barbucci A. Effect of composition on the performance of cermet electrodes. Experimental and theoretical approach. *Electrochimica Acta* 2002;**47**(7):1079–89.

[244] Zhu H, Kee RJ. Modeling distributed charge-transfer processes in SOFC membrane electrode assemblies. *J Electrochem Soc* 2008;**155**(7):B715–BB29.

[245] Yoon J, Araujo R, Grunbaum N, Baque L, Serquis A, Caneiro A, et al. Nanostructured cathode thin films with vertically-aligned nanopores for thin film SOFC and their characteristics. *Appl Surf Sci* 2007;**254**(1):266–9.

[246] Chan S, Chen X, Khor K. Cathode micromodel of solid oxide fuel cell. *J Electrochem Soc* 2004;**151**(1):A164–AA72.

[247] Suzuki M, Oshima T. Estimation of the co-ordination number in a multi-component mixture of spheres. *Powder Technology* 1983;**35**(2):159–66.

[248] Suzuki M, Oshima T. Comparison between the computer-simulated results and the model for estimating the co-ordination number in a three-component random mixture of spheres. *Powder Technology* 1985;**43**(1):19–25.

[249] Bouvard D, Lange F. Relation between percolation and particle coordination in binary powder mixtures. *Acta metallurgica et materialia* 1991;**39**(12):3083–90.

[250] Chen X, Khor K, Chan S, Yu L. Influence of microstructure on the ionic conductivity of yttria-stabilized zirconia electrolyte. *Mater Sci Eng A* 2002;**335**(1-2):246–52.

[251] Janardhanan VM, Heuveline V, Deutschmann O. Three-phase boundary length in solid-oxide fuel cells: A mathematical model. *J Pow Sour* 2008;**178**(1):368–72.

[252] Chen D, Lin Z, Zhu H, Kee RJ. Percolation theory to predict effective properties of solid oxide fuel-cell composite electrodes. *J Pow Sour* 2009;**191**(2):240–52.

[253] Costamagna P, Honegger K. Modeling of solid oxide heat exchanger integrated stacks and simulation at high fuel utilization. *J Electrochem Soc* 1998;**145**(11):3995–4007.

[254] Jeon DH, Nam JH, Kim C-J. Microstructural optimization of anode-supported solid oxide fuel cells by a comprehensive microscale model. *J Electrochem Soc* 2006;**153**(2):A406–AA17.

[255] Sanyal J, Goldin GM, Zhu H, Kee RJ. A particle-based model for predicting the effective conductivities of composite electrodes. *J Pow Sour* 2010;**195**(19):6671–9.

[256] Park S, Craciun R, Vohs JM, Gorte RJ. Direct oxidation of hydrocarbons in a solid oxide fuel cell: I. Methane oxidation. *J Electrochem Soc* 1999;**146**(10):3603–5.

[257] Park S, Vohs JM, Gorte RJ. Direct oxidation of hydrocarbons in a solid-oxide fuel cell. *Nature* 2000;**404**(6775):265.

[258] Chen M, Lin Z. Theoretical models for effective electrical and electrochemical properties of nano-particle infiltrated electrode of solid oxide fuel cell. *Int J Hydro Energy* 2014;**39**(28):15982–8.

[259] Zhang YX, Ni M, Xia CR. Microstructural insights into dual-phase infiltrated solid oxide fuel cell electrodes. *J Electrochem Soc* 2013;**160**(8):F834–F8F9.

[260] Synodis MJ, Porter CL, Vo NM, Reszka AJ, Gross MD, Snyder RC. A model to predict percolation threshold and effective conductivity of infiltrated electrodes for solid oxide fuel cells. *J Electrochem Soc* 2013;**160**(11):F1216–F1F24.

[261] Reszka AJL, Snyder RC, Gross MD. Insights into the Design of SOFC Infiltrated Electrodes with Optimized Active TPB Density via Mechanistic Modeling. *J Electrochem Soc* 2014;**161**(12):F1176–F1F83.

[262] Bertei A, Pharoah JG, Gawel DAW, Nicolella C. Microstructural Modeling and Effective Properties of Infiltrated SOFC Electrodes. *ECS Transactions* 2013;**57**(1):2527–36.

[263] Bertei A, Pharoah JG, Gawel DAW, Nicolella C. A particle-based model for effective properties in infiltrated solid oxide fuel cell electrodes. *J Electrochem Soc* 2014;**161**(12):F1243–F1F53.

[264] Bertei A, Ruiz-Trejo E, Kareh K, Yufit V, Wang X, Tariq F, et al. The fractal nature of the three-phase boundary: A heuristic approach to the degradation of nanostructured solid oxide fuel cell anodes. *Nano Energy* 2017;**38**:526–36.

[265] Nicollet C, Flura A, Vibhu V, Rougier A, Bassat JM, Grenier JC. $La_2NiO_4+\delta$ infiltrated into gadolinium doped ceria as novel solid oxide fuel cell cathodes: Electrochemical performance and impedance modelling. *J Pow Sour* 2015;**294**:473–82.

[266] Mortensen JE, Søgaard M, Jacobsen T. Analytical, 1-dimensional impedance model of a composite solid oxide fuel cell cathode. *J Electrochem Soc* 2014;**161**(3):F161–FF75.

[267] Tanner CW, Fung KZ, Virkar AV. The effect of porous composite electrode structure on solid oxide fuel cell performance: I. Theoretical analysis. *J Electrochem Soc* 1997;**144**(1):21–30.

[268] Rahmanipour M, Pappacena A, Boaro M, Donazzi A. A distributed charge transfer model for IT-SOFCs based on ceria electrolytes. *J Electrochem Soc* 2017;**164**(12):F1249–F1F64.

[269] Shah M, Nicholas JD, Barnett SA. Prediction of infiltrated solid oxide fuel cell cathode polarization resistance. *Electrochem Commun* 2009;**11**(1):2–5.

[270] Nicholas JD, Barnett SA. Measurements and Modeling of Sm0.5Sr0.5CoO3 – x – Ce0.9Gd0.1O1.95 SOFC Cathodes Produced Using Infiltrate Solution Additives. *J Electrochem Soc* 2010;**157**(4):B536–BB41.

[271] Nicholas JD, Wang L, Call AV, Barnett SA. Use of the Simple Infiltrated Microstructure Polarization Loss Estimation (SIMPLE) model to describe the performance of nano-composite solid oxide fuel cell cathodes. *Phys Chem Chem Phys* 2012;**14**(44):15379–92.

[272] Hardjo EF, Monder DS, Karan K. An effective property model for infiltrated electrodes in solid oxide fuel cells. *J Electrochem Soc* 2014;**161**(1):F83–93.

[273] Chen M, Liu T, Lin Z. Theory for the electrical conductivity of nanoparticle-infiltrated composite electrode of solid oxide fuel cell. *ECS Electrochem Lett* 2013;**2**(11):F82–FF4.

[274] Chen M, Liu D, Lin Z. A theoretical model for the electrical conductivity of core–shell nano-composite electrode of SOFC. *Solid State Ionics* 2014;**262**:370–3.

[275] Chen M, Song C, Lin Z. Property models and theoretical analysis of novel solid oxide fuel cell with triplet nano-composite electrode. *Int J Hydro Energy* 2014;**39**(25):13763–9.

[276] Reiss G, Frandsen HL, Persson ÅH, Weiss C, Brandstätter W. Numerical evaluation of oxide growth in metallic support microstructures of Solid Oxide Fuel Cells and its influence on mass transport. *J Pow Sour* 2015;**297**:388–99.

[277] Shearing PR, Cai Q, Golbert JI, Yufit V, Adjiman CS, Brandon NP. Microstructural analysis of a solid oxide fuel cell anode using focused ion beam techniques coupled with electrochemical simulation. *J Pow Sour* 2010;**195**(15):4804–10.

[278] Dieterle L, Bockstaller P, Gerthsen D, Hayd J, Ivers-Tiffée E, Guntow U. Microstructure of Nanoscaled La0.6Sr0.4CoO3-δ Cathodes for Intermediate-Temperature Solid Oxide Fuel Cells. *Adv Energy Mater* 2011;**1**(2):249–58.

[279] Rüger B, Weber A, Ivers-Tiffée E. 3D-Modelling and Performance Evaluation of Mixed Conducting (MIEC) Cathodes. *ECS Transactions* 2007;**7**(1):2065–74.

[280] Joos J. Microstructural Characterisation, Modelling and Simulation of Solid Oxide Fuel Cell Cathodes [Ph.D. thesis]. *Karlsruher Institut für Technologie* 2017.

[281] Butz B, Lefarth A, Störmer H, Utz A, Ivers-Tiffée E, Gerthsen D. Accelerated degradation of 8.5mol% Y2O3-doped zirconia by dissolved Ni. *Solid State Ionics* 2012;**214**:37–44.

[282] Euler J, Nonnenmacher W. Stromverteilung in porösen elektroden. *Electrochimica Acta* 1960;**2**(4):268–86.

[283] Zhang YX, Sun Q, Xia CR, Ni M. Geometric properties of nanostructured solid oxide fuel cell electrodes. *J Electrochem Soc* 2013;**160**(3):F278–FF89.

[284] Zheng KQ, Ni M. Reconstruction of solid oxide fuel cell electrode microstructure and analysis of its effective conductivity. *Sci Bull* 2016;**61**(1):78–85.

[285] Suzue Y, Shikazono N, Kasagi N. Micro modeling of solid oxide fuel cell anode based on stochastic reconstruction. *J Pow Sour* 2008;**184**(1):52–9.

[286] Shikazono N, Kanno D, Matsuzaki K, Teshima H, Sumino S, Kasagi N. Numerical assessment of SOFC anode polarization based on three-dimensional model microstructure reconstructed from FIB-SEM images. *J Electrochem Soc* 2010;**157**(5):B665–BB72.

[287] Matsuzaki K, Shikazono N, Kasagi N. Three-dimensional numerical analysis of mixed ionic and electronic conducting cathode reconstructed by focused ion beam scanning electron microscope. *J Pow Sour* 2011;**196**(6):3073–82.

[288] Kishimoto M, Iwai H, Saito M, Yoshida H. Three-dimensional simulation of SOFC anode polarization characteristics based on sub-grid scale modeling of microstructure. *J Electrochem Soc* 2012;**159**(3):B315–BB23.

[289] Häffelin A, Joos J, Weber A, Ivers-Tiffée E. Three-Dimensional Performance Simulation of SOFC Anodes Using FIB-Tomography Reconstructions. *ECS Transactions* 2013;**57**(1):2563–72.

[290] Häffelin A, Joos J, Ender M, Weber A, Ivers-Tiffée E. Time-Dependent 3D Impedance Model of Mixed-Conducting Solid Oxide Fuel Cell Cathodes. *J Electrochem Soc* 2013;**160**(8):F867–FF76.

[291] Adler SB, Lane J, Steele B. Electrode kinetics of porous mixed-conducting oxygen electrodes. *J Electrochem Soc* 1996;**143**(11):3554–64.

[292] Kim JW, Virkar AV, Fung KZ, Mehta K, Singhal SC. Polarization effects in intermediate temperature, anode-supported solid oxide fuel cells. *J Electrochem Soc* 1999;**146**(1):69–78.

[293] Primdahl S, Mogensen M. Gas diffusion impedance in characterization of solid oxide fuel cell anodes. *J Electrochem Soc* 1999;**146**(8):2827–33.

[294] Geisler H, Kromp A, Weber A, Ivers-Tiffée E. Stationary FEM Model for Performance Evaluation of Planar Solid Oxide Fuel Cells Connected by Metal Interconnectors: I. Model Framework and Validation. *J Electrochem Soc* 2014;**161**(6):F778–FF88.

[295] Beale SB, Reimer U, Froning D, Jasak H, Andersson M, Pharoah JG, et al. Stability issues of fuel cell models in the activation and concentration regimes. *J Electrochem Energy* 2018;**15**(4) 041008–7.

[296] Zhang S, Beale SB, Reimer U, Andersson M, Lehnert W. Polymer electrolyte fuel cell modeling - A comparison of two models with different levels of complexity. *Int J Hydro Energy* 2020;**45**(38):19761–77.

[297] openFuelCell web site [Available from: https://openfuelcell.sourceforge.io/.

[298] Zhang F, Bonart H, Zirwes T, Habisreuther P, Bockhorn H, Zarzalis N. *Direct numerical simulation of chemically reacting flows with the public domain code OpenFOAM. High Performance Computing in Science and Engineering '14*. Springer; 2015. p. 221–36.

[299] Peksen M. 3D transient multiphysics modelling of a complete high temperature fuel cell system using coupled CFD and FEM. *Int J Hydro Energy* 2014;**39**(10):5137–47.

[300] Li A, Song C, Lin ZJ. A multiphysics fully coupled modeling tool for the design and operation analysis of planar solid oxide fuel cell stacks. *Applied Energy* 2017;**190**:1234–44.

[301] Nishida RT, Beale SB, Pharoah JG. Comprehensive computational fluid dynamics model of solid oxide fuel cell stacks. *Int J Hydro Energy* 2016;**41**(45):20592–605.

[302] Blum L, Batfalsky P, Fang Q, de Haart LGJ, Malzbender J, Margaritis N, et al. Solid Oxide Fuel Cell, Stack and System Development Status at Forschungszentrum Jülich. *ECS Transactions* 2015;**68**(1):157–69.

[303] Beale SB, Zhang S, Andersson M, Nishida RT, Pharoah JG, Lehnert W. Heat and Mass Transfer in Fuel Cells and Stacks. In: Runchal A, editor. *50 Years of CFD in Engineering Sciences: A Commemorative Volume in Memory of D Brian Spalding*. Singapore: Springer Singapore; 2020. p. 485–511.

[304] Molla TT, Kwok K, Frandsen HL. Efficient modeling of metallic interconnects for thermo-mechanical simulation of SOFC stacks: Homogenized behaviors and effect of contact. *Int J Hydro Energy* 2016;**41**(15):6433–44.

[305] Navasa M, Miao X-Y, Frandsen HL. A fully-homogenized multiphysics model for a reversible solid oxide cell stack. *Int J Hydro Energy* 2019;**44**(41):23330–47.

[306] Al-Masri A, Peksen M, Blum L, Stolten D. A 3D CFD model for predicting the temperature distribution in a full scale APU SOFC short stack under transient operating conditions. *Applied Energy* 2014;**135**:539–47.

[307] Zhu J, Lin Z. Degradations of the electrochemical performance of solid oxide fuel cell induced by material microstructure evolutions. *Applied Energy* 2018;**231**:22–8.

[308] Miyoshi K, Iwai H, Kishimoto M, Saito M, Yoshida H. Chromium poisoning in (La,Sr)MnO3 cathode: Three-dimensional simulation of a solid oxide fuel cell. *J Pow Sour* 2016;**326**:331–40.

[309] Iwai H, Yamaguchi Y, Kishimoto M, Saito M, Yoshida H. Numerical Study on Progress of Cr Poisoning in LSM-YSZ Cathode of a Planar Solid Oxide Fuel Cell. *Meeting Abstracts* 2017;**MA2017-03**(1):146.

[310] Gao S, Li J, Lin Z. Theoretical model for surface diffusion driven Ni-particle agglomeration in anode of solid oxide fuel cell. *J Pow Sour* 2014;**255**:144–50.

[311] Nakajo A, Wuillemin Z, Metzger P, Diethelm S, Schiller G, Van herle J, et al. Electrochemical Model of Solid Oxide Fuel Cell for Simulation at the Stack Scale I. Calibration Procedure on Experimental Data. *J Electrochem Soc* 2011;**158**(9):B1083–BB101.

[312] Nakajo A, Tanasini P, Diethelm S, Van herle J, Favrat D. Electrochemical Model of Solid Oxide Fuel Cell for Simulation at the Stack Scale II: Implementation of Degradation Processes. *J Electrochem Soc* 2011;**158**(9):B1102–B1B18.

[313] Nakajo A, Mueller F, Brouwer J, Van herle J, Favrat D. Progressive activation of degradation processes in solid oxide fuel cell stacks: Part II: Spatial distribution of the degradation. *J Pow Sour* 2012;**216**:434–48.

[314] Nakajo A, Mueller F, Brouwer J, Van herle J, Favrat D. Progressive activation of degradation processes in solid oxide fuel cells stacks: Part I: Lifetime extension by optimisation of the operating conditions. *J Pow Sour* 2012;**216**:449–63.

[315] Zaccaria V, Tucker D, Traverso A. A distributed real-time model of degradation in a solid oxide fuel cell, part I: Model characterization. *J Pow Sour* 2016;**311**:175–81.

[316] Zaccaria V, Tucker D, Traverso A. A distributed real-time model of degradation in a solid oxide fuel cell, part II: Analysis of fuel cell performance and potential failures. *J Pow Sour* 2016;**327**:736–42.

[317] Larrain D, Van herle J, Favrat D. Simulation of SOFC stack and repeat elements including interconnect degradation and anode reoxidation risk. *J Pow Sour* 2006;**161**(1):392–403.

[318] Yan M, Zeng M, Chen Q, Wang Q. Numerical study on carbon deposition of SOFC with unsteady state variation of porosity. *Applied Energy* 2012;**97**:754–62.

[319] Wu X, Ye Q. Fault diagnosis and prognostic of solid oxide fuel cells. *J Pow Sour* 2016;**321**:47–56.

[320] Guida M, Postiglione F, Pulcini G. A Bayesian Estimation Procedure for the Non-homogeneous Gamma Process. 9th International Conference on Mathematical Methods in Reliability (MMR 2015); 2015; Tokyo.

[321] Guida M, Postiglione F, Pulcini G. A random-effects model for long-term degradation analysis of solid oxide fuel cells. *Reliab Eng Syst Safety* 2015;**140**:88–98.

[322] Walters KM, Dean AM, Zhu H, Kee RJ. Homogeneous kinetics and equilibrium predictions of coking propensity in the anode channels of direct oxidation solid-oxide fuel cells using dry natural gas. *J Pow Sour* 2003;**123**(2):182–9.

[323] Neidhardt JP, Bessler WG. Microkinetic Modeling of Nickel Oxidation in Solid Oxide Cells: Prediction of Safe Operating Conditions. *Chemie Ingenieur Technik* 2019;**91**(6):843–55.

[324] Riegraf M, Schiller G, Costa R, Friedrich KA, Latz A, Yurkiv V. Elementary kinetic numerical simulation of Ni/YSZ SOFC anode performance considering sulfur poisoning. *J Electrochem Soc* 2014;**162**(1):F65.

[325] Jiao Z, Shikazono N. Simulation of Solid Oxide Fuel Cell Anode Microstructure Evolution Using Phase Field Method. *J Electrochem Soc* 2013;**160**(6):F709–FF15.

[326] Abdeljawad F, Volker B, Davis R, McMeeking RM, Haataja M. Connecting microstructural coarsening processes to electrochemical performance in solid oxide fuel cells: An integrated modeling approach. *J Pow Sour* 2014;**250**:319–31.

[327] Jiao Z, Shikazono N. Prediction of Nickel Morphological Evolution in Composite Solid Oxide Fuel Cell Anode Using Modified Phase Field Model. *J Electrochem Soc* 2018;**165**(2):F55–63.

[328] Trini M, De Angelis S, Jørgensen PS, Hauch A, Chen M, Hendriksen PV. Phase Field Modelling of Microstructural Changes in NI/YSZ Solid Oxide Electrolysis Cell Electrodes. Proceeding of the 42nd International Conference on Advanced Ceramics and Composites.

[329] NIST-JANAF Thermochemical Tables [Internet]. Available from: https://janaf.nist.gov/.

[330] Linderoth S, Bonanos N, Jensen KV, Bilde-Sorensen JB. Effect of NiO-to-Ni transformation on conductivity and structure of yttria-stabilized ZrO2. *J Am Ceram Soc* 2001;**84**(11):2652–6.

[331] Butz B, Lefarth A, Stormer H, Utz A, Ivers-Tiffee E, Gerthsen D. Accelerated degradation of 8.5 mol% Y2O3-doped zirconia by dissolved Ni. *Solid State Ionics* 2012;**214**:37–44.

[332] Fergus J. Electrolytes for solid oxide fuel cells. *J Pow Sour* 2006;**162**(1):30–40.

[333] Niedrig C, Wagner S, Menesklou W, Baumann S, Ivers-Tiffee E. Oxygen equilibration kinetics of mixed-conducting perovskites BSCF, LSCF, and PSCF at 900 degrees C determined by electrical conductivity relaxation. *Solid State Ionics* 2015;**283**:30–7.

[334] Leonide A, Ruger B, Weber A, Meulenberg WA, Ivers-Tiffée E. Performance Study of Alternative (La,Sr)FeO 3- ë and (La,Sr)(Co,Fe)O 3- ë MIEC Cathode Compositions. *ECS Trans* 2009;**25**(2):2487–96.

[335] Utz A, Hansen KV, Norrman K, Ivers-Tiff,e E, Mogensen M. Impurity Features in Ni-YSZ-H2-H2O Electrodes. *Solid State Ionics.* 2011;**183**(1):60–70.

[336] Mogensen M, Jensen KV, Jorgensen MJ, Primdahl S. Progress in understanding SOFC electrodes. *Solid State Ionics* 2002;**150**(1-2):123–9.

[337] Jensen KV, Wallenberg R, Chorkendorff I, Mogensen M. Effect of impurities on structural and electrochemical properties of the Ni-YSZ interface. *Solid State Ionics* 2003;**160**(1-2):27–37.

[338] Yokokawa H, Yamaji K, Brito M, Kishimoto H, Horita T. General considerations on degradation of Solid Oxide Fuel Cell anodes and cathodes due to impurities in gases. *J Pow Sour* 2011;**196**(17):7070–5.

[339] Yokokawa H, Tu H, Iwanschitz B, Mai A. Fundamental mechanisms limiting solid oxide fuel cell durability. *J Pow Sour* 2008;**182**(2):400–12.

[340] Utz A, St"rmer H, Leonide A, Weber A, Ivers-Tiff,e E. Degradation and Relaxation Effects of Ni Patterned Anodes in H 2 /H 2 O Atmosphere. *J Electrochem Soc* 2010;**157**(6):B920–BB30.

[341] Endler-Schuck C, Joos J, Niedrig C, Weber A, Ivers-Tiffée E. The chemical oxygen surface exchange and bulk diffusion coefficient determined by impedance spectroscopy of porous $La_{0.58}Sr_{0.4}Co_{0.2}Fe_{0.8}O_{3-\delta}$ (LSCF) cathodes. *Solid State Ionics* 2015;**269**:67–79.

[342] Campanari S, Iora P. Definition and sensitivity analysis of a finite volume SOFC model for a tubular cell geometry. *J Pow Sour* 2004;**132**(1-2):113–26.

[343] Carraro T, Joos J, Ruger B, Weber A, Ivers-Tiffee E. 3D finite element model for reconstructed mixed-conducting cathodes: II. Parameter sensitivity analysis. *Electrochimica Acta* 2012;**77**:309–14.

[344] Bieberle A, Meier L, Gauckler L. The electrochemistry of Ni pattern anodes used as solid oxide fuel cell model electrodes. *J Electrochem Soc* 2001;**148**(6):A646.

[345] Utz A, Stormer H, Leonide A, Weber A, Ivers-Tiffee E. Degradation and Relaxation Effects of Ni Patterned Anodes in H-2-H2O Atmosphere. *J Electrochem Soc* 2010;**157**(6):B920–BB30.

[346] Sukeshini AM, Habibzadeh B, Becker BP, Stoltz CA, Eichhorn BW, Jackson GS. Electrochemical oxidation of H2, CO, and CO/ H2 mixtures on patterned Ni anodes on YSZ electrolytes. *J Electrochem Soc* 2006;**153**(4):A705.

[347] Liu M, Lynch ME, Blinn K, Alamgir FM, Choi Y. Rational SOFC material design: new advances and tools. *Materials Today* 2011;**14**(11):534–46.

[348] Bauerle JE. Study of solid electrolyte polarization by a complex admittance method. *J Phys Chem Solids* 1969;**30**(12):2657–70.

[349] Verkerk MJ, Middelhuis BJ, Burggraaf AJ. Effect of grain boundaries on the conductivity of high-purity ZrO/sub 2/-Y/sub 2/O/sub 3/ ceramics. *Solid State Ionics* 1982;**6**(2):159–70.

[350] Maier J. On the conductivity of polycrystalline materials. *Berichte der Bunsen-Gesellschaft-Phys Chem Chem Phys* 1986;**90**(1):26–33.

[351] Peters C, Weber A, Butz B, Gerthsen D, Ivers-Tiffée E. Grain-Size Effects in YSZ Thin-Film Electrolytes. *J Am Ceram Soc* 2009;**92**(9):2017–24.

[352] Endler C, Leonide A, Weber A, Tietz F, Ivers-Tiffée E. Time-dependent electrode performance changes in intermediate temperature solid oxide fuel cells. *J Electrochem Soc* 2010;**157**(2):B292–B2B8.

[353] Leonide A. *SOFC Modelling and Parameter Identification by means of Impedance Spectroscopy: Karlsruhe Institute of Technology*; 2010.

[354] Joos J, Ender M, Rotscholl I, Menzler NH, Ivers-Tiffée E. Quantification of double-layer Ni/YSZ fuel cell anodes from focused ion beam tomography data. *J Pow Sour* 2014;**246**:819–30.

[355] Virkar AV, Chen J, Tanner CW, Kim JW. The role of electrode microstructure on activation and concentration polarizations in solid oxide fuel cells. *Solid State Ionics* 2000;**131**(1-2):189–98.

[356] Aguiar P, Adjiman CS, Brandon NP. Anode-supported intermediate temperature direct internal reforming solid oxide fuel cell. I: model-based steady-state performance. *J Pow Sour* 2004;**138**(1-2):120–36.

[357] Akkaya AV. Electrochemical model for performance analysis of a tubular SOFC. *Int J Energy Res* 2007;**31**(1):79–98.

[358] Wang Y, Yoshiba F, Watanabe T, Weng SL. Numerical analysis of electrochemical characteristics and heat/species transport for planar porous-electrode–supported SOFC. *J Pow Sour* 2007;**170**(1):101–10.

[359] Noren DA, Hoffman MA. Clarifying the Butler-Volmer equation and related approximations for calculating activation losses in solid oxide fuel cell models. *J Pow Sour* 2005;**152**(1):175–81.

[360] Jiang W, Fang RX, Khan JA, Dougal RA. Parameter setting and analysis of a dynamic tubular SOFC model. *J Pow Sour* 2006;**162**(1):316–26.

[361] Sanchez D, Chacartegui R, Munoz A, Sanchez T. Thermal and electrochemical model of internal reforming solid oxide fuel cells with tubular geometry. *J Pow Sour* 2006;**160**(2):1074–87.

[362] Ni M, Leung MKH, Leung DYC. Parametric study of solid oxide steam electrolyzer for hydrogen production. *Int J Hydro Energy* 2007;**32**(13):2305–13.

[363] YamamuraT, TagawaH, SaitoT, MizusakiJ, KamitaniK, HiranoK, et al., editors. Reaction kinetics at the nickel pattern electrode on YSZ and its dependence on temperature. SOFC IV; 1995.

[364] Costamagna P, Selimovic A, Del Borghi M, Agnew G. Electrochemical model of the integrated planar solid oxide fuel cell (IP-SOFC). *Chem Eng J* 2004;**102**(1):61–9.

[365] Beale SB, Zhubrin SV, Dong W. Numerical Studies of Solid-oxide Fuel Cells. Proceedings 12th International Heat Transfer Conference; 2002; Grenoble France.

[366] Klotz D, Weber A, Ivers-Tiffée E. Dynamic Electrochemical Model for SOFC-Stacks. *ECS Trans* 2009;**25**(2):1331–40.

[367] Geisler H, Kornely M, Weber A, l Ivers-Tiff,e. Enhancing SOFC-Stack Performance by Model-based Adaptation of Cathode Gas Transport Conditions. *ECS Trans* 2013;**57**(1):2871–81.

[368] Geisler H, Dierickx S, Weber A, Ivers-Tiffee E. A 2D Stationary FEM Model for Hydrocarbon Fuelled SOFC Stack Layers. *ECS Trans* 2015;**68**(1):2151–8.

[369] Russner N, Geisler H, Dierickx S, Weber A. Ivers-Tiff+©e E. A Non-Isothermal 2D Stationary FEM Model for Hydrocarbon Fueled SOFCs Stack Layers. *ECS Trans* 2017;**78**(1):2673–82.

[370] Braun RJ. *Optimal design and operation of solid oxide fuel cell systems for small-scale stationary applications [PhD]*. Madison: University of Wisconsin-Madison; 2002.

[371] Colpan CO, Hamdullahpur F, Dincer I. Transient heat transfer modeling of a solid oxide fuel cell operating with humidified hydrogen. *Int J Hydro Energy* 2011:36.

[372] Li M, Powers JD, Brouwer J. A Finite Volume SOFC Model for Coal-Based Integrated Gasification Fuel Cell Systems Analysis. *J Fuel Cell Sci Tech* 2010;**7**(4):041017.

[373] Lueth CA, Walchshofer CF. Automated SOFC Design Exploration. *ECS Transactions* 2017;**78**(1):2607–20.

[374] Bessler WG, Gewies S, Willich C, Schiller G, Friedrich KA. Spatial Distribution of Electrochemical Performance in a Segmented SOFC: A- Combined Modeling and Experimental Study. *Fuel Cells* 2010;**10**(3):411–18.

[375] Dekker N, Van Wees JF, Rietveld BG. Determination of the anode flow distribution in a sofc stack at nominal operating conditions by eis. *ECS Trans* 2009;**25**(2):1871–8.

[376] Yu R, Guan W, Zhou XD. Probing Temperature Inside Planar SOFC Short Stack, Modules, and Stack Series. *JOM* 2017;**69**(2):247–53.

[377] van Herle J, Larrain D, Autissier N, Wuillemin Z, Molinelli M, Favrat D. Modeling and experimental validation of solid oxide fuel cell materials and stacks. *J Eur Ceram Soc* 2005;**25**(12):2627–32.

[378] Kulikovsky A, Kucernak A, Kornyshev A. Feeding PEM fuel cells. *Electrochimica Acta* 2005;**50**(6):1323–33.

[379] Hassan SM, Hasnain SA. Measuring Porosity of Anodes in Solid Oxide Fuel Cell (SOFC) through Water Archimedeans Porosimetry. *J Pow Energy Eng* 2015;**3**(06):46.

[380] Boigues-Muñoz C, Pumiglia D, McPhail SJ, Santori G, Montinaro D, Comodi G, et al. More accurate macro-models of solid oxide fuel cells through electrochemical and microstructural parameter estimation–Part II: Parameter estimation. *J Pow Sour* 2015;**286**:321–9.

[381] Orazem ME, Tribollet B. *Electrochemical impedance spectroscopy*. 2nd edn. John Wiley & Sons; 2017.

[382] Endler-Schuck C, Leonide A, Weber A, Uhlenbruck S, Tietz F, Ivers-Tiff,e E. Performance analysis of mixed ionic-electronic conducting cathodes in anode supported cells. *J Pow Sour* 2011;**196**(17):7257–62.

[383] Kornely M, Neumann A, Menzler N, Leonide A, Weber A, Ivers-Tiffée E. Degradation of anode supported cell (ASC) performance by Cr-poisoning. *J Pow Sour* 2011;**196**:7203–8.

[384] Kornely M, Menzler NH, Weber A, Ivers-Tiffée E. Degradation of a High Performance SOFC Cathode by Cr-Poisoning at OCV-Conditions. *Fuel Cells* 2013;**00**:1–5.

[385] Kromp A, Dierickx S, Leonide A, Weber A, Ivers-Tiff,e E. Electrochemical Analysis of Sulfur-Poisoning in Anode Supported SOFCs Fuelled with a Model Reformate. *J Electrochem Soc* 2012;**159**(5):B597–601.

[386] Weber A, Dierickx S, Kromp A, Ivers-Tiffée E. Sulfur Poisoning of Anode-Supported SOFCs under Reformate Operation. *Fuel Cells* 2013;**13**:487–93.

[387] Ploner A, Hagen A, Hauch A. Study of Operating Parameters for Accelerated Anode Degradation in SOFCs. *Fuel Cells* 2017;**17**(4):498–507.

[388] Hjalmarsson P, Sun X, Liu YL, Chen M. Influence of the oxygen electrode and inter-diffusion barrier on the degradation of solid oxide electrolysis cells. *J Pow Sour* 2013;**223**(0):349–57.

[389] Jensen SH, Hauch A, Hendriksen PV, Mogensen M, Bonanos N, Jacobsen T. A method to separate process contributions in impedance spectra by variation of test conditions. *J Electrochem Soc* 2007;**154**(12):B1325–B1B30.

[390] Tsai CH, Hwang CS, Chang CL, Yang SF, Cheng SW, Shie ZYC, et al. Performance and long term durability of metal-supported solid oxide fuel cells. *J Ceram Soc Jpn* 2015;**123**(1436):205–12.

[391] Nielsen J, Mogensen M. SOFC LSM: YSZ cathode degradation induced by moisture: An impedance spectroscopy study. *Solid State Ionics* 2011;**189**(1):74–81.

[392] Jalilvand G, Faghihi-Sani M-A. Fe doped Ni–Co spinel protective coating on ferritic stainless steel for SOFC interconnect application. *Int J Hydro Energy* 2013;**38**(27):12007–14.

[393] Yang S, Chen T, Wang Y, Peng Z, Wang WG. Electrochemical analysis of an anode-supported SOFC. *Int J Electrochem Sci* 2013;**8**(2):2330–44.

[394] Faes A, Hessler-Wyser A, Presvytes D, Vayenas C. Nickel–zirconia anode degradation and triple phase boundary quantification from microstructural analysis. *Fuel Cells* 2009;**9**(6):841–51.

[395] Nelson GJ, Grew KN, Izzo JR, Lombardo JJ, Harris WM, Faes A, et al. Three-dimensional microstructural changes in the Ni–YSZ solid oxide fuel cell anode during operation. *Acta Materialia* 2012;**60**(8):3491–500.

[396] Haering C, Roosen A, Schichl H. Degradation of the electrical conductivity in stabilised zirconia systems Part I: yttria-stabilised zirconia. *Solid State Ionics* 2005;**176**(3-4):253–9.

[397] Haering C, Roosen A, Schichl H, Schnoller M. Degradation of the electrical conductivity in stabilised zirconia system Part II: Scandia-stabilised zirconia. *Solid State Ionics* 2005;**176**(3-4):261–8.

[398] Butz B, Kruse P, Stormer H, Gerthsen D, Muller A, Weber A, et al. Correlation between microstructure and degradation in conductivity for cubic Y2O3-doped ZrO2. *Solid State Ionics* 2006;**177**(37-38):3275–84.

[399] Keane M, Mahapatra MK, Verma A, Singh P. LSM-YSZ interactions and anode delamination in solid oxide electrolysis cells. *Int J Hydro Energy* 2012;**37**(22):16776–85.

[400] Wu QH, Liu ML, Jaegermann W. X-ray photoelectron spectroscopy of La0.5Sr0.5MnO3. *Mater Lett* 2005;**59**(16):1980–3.

[401] Jiang SP, Wang W. Sintering and grain growth of (La,Sr)MnO3 electrodes of solid oxide fuel cells under polarization. *Solid State Ionics* 2005;**176**(13-14):1185–91.

[402] Shah M, Voorhees PW, Barnett SA. Time-dependent performance changes in LSCF-infiltrated SOFC cathodes: The role of nano-particle coarsening. *Solid State Ionics* 2011;**187**(1):64–7.

[403] Jiang SP, Zhang JP, Apateanu L, Foger K. Deposition of chromium species at Sr-doped LaMnO3 electrodes in solid oxide fuel cells I. Mechanism and kinetics. *J Electrochem Soc* 2000;**147**(11):4013–22.

[404] Position paper on solid oxide cells: International energy agency advanced fuel cell technology collaboration programme; 2019 [Available from: https://www.ieafuelcell.com/index.php?id=5#c280.

[405] The european green deal Brussels2019 [Available from: https://eur-lex.europa.eu/resource.html?uri=cellar:b828d165-1c22-11ea-8c1f-01aa75ed71a1.0002.02/DOC_1&format=PDF.

[406] Whiston MM, Azevedo IM, Litster S, Samaras C, Whitefoot KS, Whitacre JF. Meeting US Solid Oxide Fuel Cell Targets. *Joule* 2019;**3**(9):2060–5.

Steven Beale is a senior scientist and group leader at the Forschungszentrum Jülich. Formerly a principal research officer at the National Research Council of Canada, he has 35 years of experience in computational fluid dynamics and numerical heat and mass transfer, and 22 years in building fuel cell models. Dr. Beale is operating agent for the International Energy Agency technology collaboration programme on advanced fuel cells, modelling of fuel cells systems annex. He holds engineering degrees from McGill and the University of California at Berkeley, and a PhD from Imperial College, London. Dr. Beale is an Adjunct Professor at Queen's University in Canada, and a Fellow of the ASME (USA) and the IMechE (UK).

Martin Andersson is an Associate Professor at the department of Energy Sciences, where his main research is on modelling of fuel cells at various length scales. Andersson has a M. Sc. in Environmental Engineering from Lund University (2007) and a PhD in Heat Transfer from Lund University (2011). Martin was granted a Marie Curie Fellowship in 2015, which enabled him to work as a Guest Professor at the research centre Jülich in Germany between 2015 and 2019. Martin has served as Adjunct Professor at University of Electronic Science and Engineering of China (UESTC) in Chengdu, China since 2017. Martin is also the founder and director of the Lund University master's programme in Sustainable Energy Engineering.

Carlos Boigues-Muñoz is a programme manager in Enel X. He was formerly Research & Innovation Engineer at the Italian National Agency for New Technologies, Energy and Sustainable Economic Development (ENEA) Rome, As such, he was involved in the development of advanced diagnosis and prognosis techniques based on electrochemical impedance spectroscopy measurements for monitoring online the state-of-health of fuel cells and electrolyser systems. In addition to coaching and mentoring of team members. A former Visiting Scientist at VTT Technical Research Centre of Finland, he holds a Ph.D. in Energy Engineering from the Università Politecnica delle Marche, Ancona, a Masters degree from Universidad Politecnica de Valencia and Master thesis from the Technical University of Denmark, Copenhagen.

Henrik L. Frandsen is a Senior Researcher and the high temperature electrolysis technology track leader at the Department of Energy Conversion and Storage at the Technical University of Denmark. He is leading national and European projects on the solid oxide cell technologies, facilitating a close collaboration between industry and academia. His research on modelling covers multiphysics and multiscale simulation of solid oxide cells and stacks, with a special focus on their mechanical behavior. He holds Ph.D. and MSc degrees in Civil Engineering from Aalborg University, Denmark. Henrik L. Frandsen has currently co-authored 61 papers in international peer reviewed journals, 29 proceeding papers, as well as 3 patents, primarily on the solid oxide cell technologies.

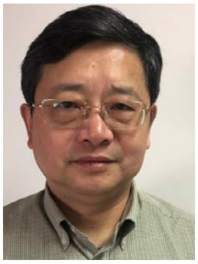

Zijing Lin is Professor of Physics in the Department of Physics at the University of Science and Technology of China in Hefei. He holds a B.Sc. in physics from Hangzhou University, and Ph.D., from the University of Science and Technology of China. He was a visiting researcher, at the Technical University of Clausthal, and Visiting Scientist, the Forschungszentrum Jülich, University of New Brunswick, and Pacific Northwest National Laboratory.

Stephen J. McPhail is co-author of more than 75 papers on fuel cells and hydrogen development, and heads the laboratory for electrochemical characterisation of high-temperature cells and stacks in ENEA, the Italian Agency for energy, new technologies and sustainable economic development. He works on the alignment of experimental and numerical investigation as convenor of working Group 13 of the International Electrotechnical Committee Technical Committee 105, on fuel cell technologies, and as a participant in many international initiatives on harmonisation of fuel cell operation and testing procedures for the generation of quality data. He is Coordinator of the joint programme on fuel cells and hydrogen in the European Energy Research Alliance and Executive Committee member for Italy of the International Energy Agency Technology Collaboration Programme on Advanced Fuel Cells.

Meng Ni is a Professor in the Department of Building and Real Estate at the Hong Kong Polytechnic University. He holds a PhD in Mechanical Engineering from the University of Hong Kong. He was a visiting researcher at the Forschungszentrum Jülich in 2017. He has 14 years research experience in modelling of solid oxide fuel cells/electrolysers; numerical heat/mass transfer; transport phenomena in porous media; in addition to experience in turbine blade cooling design. He has published over 150 papers in journals. He is an associate editor for Sustainable Energy Technologies and Assessments and a former associate editor for Science Bulletin. He is an active reviewer for over 60 academic journals.

Bengt Sundén is Professor Emeritus and Senior Professor in Heat Transfer at Lund University in Sweden. He was previously governmental Professor of Heat Transfer, and Head of the Department of Energy Sciences at Lund University. He graduated with an M.Sc. in Mechanical Engineering at Chalmers University of Technology, Göteborg, Sweden in 1973 and presented his PhD-thesis in thermodynamics and fluid mechanics in 1979, also at Chalmers University. He has published widely on energy, heat transfer, heat exchangers, fuel cells, nanofluids and nanostructured heat transfer surfaces.

André Weber is a senior researcher at the Institute for Applied Materials – Electrochemical Technologies (IAM-ET) at Karlsruhe Institute of Technology (KIT), where he heads both the fuel cell and battery research groups. In addition, he has been scientific manager of the Fuel Cell Test Laboratory, a joint laboratory of KIT and the European Institute for Energy Research, designated for testing fuel cell systems, since 2002. After studying electrical engineering at RWTH Aachen University, he obtained a PhD at Universität Karlsruhe (now KIT). He was strongly involved in the establishment of the SOFC group at IAM-ET, he has collaborated with many groups in numerous national, European and international research projects. His research is related to the electrical testing and modelling of fuel cells and batteries, with emphasis on detailed characterization by means of electrochemical impedance spectroscopy. André Weber has authored or co-authored several book chapters, 80 conference proceedings and more than 100 peer-reviewed journal papers on scientific topics related to fuel cells and batteries.

Adam Z. Weber is Staff Scientist/Engineer at Lawrence Berkeley National Laboratory and current Group Leader of the Energy Conversion Group within the Energy Technologies Area. He is also the Fuel Cell Lab Program Manager and Deputy Director of Fuel Cell Performance and Durability and HydroGen Advanced Water Splitting Materials Consortia. He has published over 120 peer-reviewed articles and 11 book chapters on fuel cells, electrolysers, and related electrochemical phenomena and components, and has given over 150 research talks including various invited and keynote ones. He has worked in fuel cells for over 15 years and leads a research group with a focus on mathematical modelling of the underlying physical phenomena and advanced diagnostics and characterisation of fuel-cell components.